2-1-2011

Band Structure Calculations of Strained Semiconductors Using Empirical Pseudopotential Theory

Jiseok Kim
University of Massachusetts - Amherst

BAND STRUCTURE CALCULATIONS OF STRAINED SEMICONDUCTORS USING EMPIRICAL PSEUDOPOTENTIAL THEORY

A Dissertation Presented

by

JISEOK KIM

Submitted to the Graduate School of the
University of Massachusetts Amherst in partial fulfillment
of the requirements for the degree of

DOCTOR OF PHILOSOPHY

February 2011

Electrical and Computer Engineering

BAND STRUCTURE CALCULATIONS OF STRAINED SEMICONDUCTORS USING EMPIRICAL PSEUDOPOTENTIAL THEORY

A Dissertation Presented

by

JISEOK KIM

Approved as to style and content by:

Massimo V. Fischetti, Chair

Eric Polizzi, Member

Neal Anderson, Member

Dimitrios Maroudas, Member

C. V. Hollot, Department Chair
Electrical and Computer Engineering

To my family.

ACKNOWLEDGMENTS

"If I have seen a little further it is by standing on the shoulders of giants."

Sir Isaac Newton

First of all, I would like to express my heartfelt gratitude to my doctoral advisor Professor Massimo V. Fischetti for his meticulous and constant guidance and support throughout this work. As a renowned physicist in the field of solid state device physics he always has been a role model in my life and taught me how to enjoy learning and doing research. I have been amazingly fortunate to work with him and I hope that one day I would become as good an advisor to my students as he has been to me.

I would like to thank my dissertation committee members, Prof. Eric Polizzi, Prof. Neal Anderson and Prof. Dimitrios Maroudas for their sincere interest and constructive criticism, suggestion and advice for this work.

I also thank Dr. Siddarth A. Krishana, Dr. Michael P. Chudzik for giving me an opportunity to work at IBM as an intern and for the chance to experimentally work on state-of-the-art high-k MOSFET devices.

I would like to thank to Dr. Seonghoon Jin at Synopsys, a talented former post-doc in our group, for his support throughout the initial work on the pseudopotential calculation.

I wish to express my sincere gratitude to my friends, Terrance, Dusung, Jinwook, Banyoon and Changhyun for their friendship with consistent encouragement and love.

Finally, and most importantly, I wish to thank my wife Hokyeong and my son Doyoon for their endless patience, support and love during all these years. Also, I would like to express my sincere gratitude to my parents, parents in law, sisters and

sisters and brothers in law. Without their love and support, this dissertation would not have been possible.

ABSTRACT

BAND STRUCTURE CALCULATIONS OF STRAINED SEMICONDUCTORS USING EMPIRICAL PSEUDOPOTENTIAL THEORY

FEBRUARY 2011

JISEOK KIM

B.S., KYUNGHEE UNIVERSITY SEOUL

M.S., BALL STATE UNIVERSITY MUNCIE

Ph.D., UNIVERSITY OF MASSACHUSETTS AMHERST

Directed by: Professor Massimo V. Fischetti

Electronic band structure of various crystal orientations of relaxed and strained bulk, 1D and 2D confined semiconductors are investigated using nonlocal empirical pseudopotential method with spin-orbit interaction. For the bulk semiconductors, local and nonlocal pseudopotential parameters are obtained by fitting transport-relevant quantities, such as band gap, effective masses and deformation potentials, to available experimental data. A cubic-spline interpolation is used to extend local form factors to arbitrary q and the resulting transferable local pseudopotential $V(q)$ with correct work function is used to investigate the 1D and 2D confined systems with supercell method. Quantum confinement, uniaxial and biaxial strain and crystal orientation effects of the band structure are investigated. Regarding the transport relavant quantities, we have found that the largest ballistic electron conductance oc-

curs for compressively-strained large-diameter [001] wires while the smallest transport electron effective mass is found for larger-diameter [110] wires under tensile stress.

TABLE OF CONTENTS

LIST OF TABLES

Table **Page**

LIST OF FIGURES

Figure **Page**

CHAPTER 1

INTRODUCTION

Study of electronic transport in the wide range of alternative structures and materials currently investigated to scale transistors to the 10 nanometer length [16] requires accurate knowledge of transport parameters (such as effective masses, band-gaps, deformation potentials, etc.) which are not always readily available experimentally. First-principle band-structure calculations, while absolutely necessary to determine the atomic structure of alternative channels or device-structures, are still moderately affected by the band-gap problem which requires numerically expensive GW or generalized gradient approximation (GGA) corrections. On the other hand, after suitable calibration, empirical pseudopotentials can provide the much needed information with much lower computational effort. An early example of the use of empirical psudopotential method (EPM) in our context is given by the study of the significant enhancement of electron mobility observed in strained Si n-type MOSFETs [93, 74] and of the hole mobility observed in strained Ge channels [49]. The underlying physical mechanisms responsible for these observations have been investigated employing various theoretical models [82, 30, 80, 28, 81], including empirical pseudopotentials, leading to the conclusions that the mobility enhancement is due to a lower conductivity mass [30, 81], to the suppression of intervalley phonon scattering due to the strain-induced band splitting [81], and to reduced interface-roughness scattering [28].

For bulk semiconductors we intend to extend these studies to more general strain conditions and also to III-V compound semiconductors by extracting deformation potentials associated with phonon scattering, energy shifts at symmetry points, band-

gap bowing parameters in alloys and effective masses at conduction and valence band minima and maxima, respectively, from the full band structure calculated for strained semiconductors. Indeed, so far most of the band structure calculations for strained materials have been limited to certain semiconductors or certain crystal orientations resulting in still missing informations such as effective masses as a function of strain, conduction band deformation potentials in some III-V channel-materials. In so doing, we intend to provide comprehensive information for material parameters for Si, Ge, and III-Vs as a function of strain along all three major crystal orientations (001), (110) and (111).

The nonlocal EPM with spin-orbit interaction has been one of the most popular method to calculate the full band structure for device simulation since its first application to fcc semiconductors by Chelikowsky and Cohen [18, 17]. Since then, the EPM has been successfully adopted by several groups [31, 30, 50, 43, 12, 36, 54, 73, 100, 59] to calculate the electronic band structure of relaxed or strained group-IV and III-V bulk semiconductors where one needs a continuous form of full Fourier transform of local pseudopotential $V(q)$ by interpolating among form factors. Also, the concept of a supercell has allowed us to account for surface and interface geometries using EPM. The supercell was constructed to contain a slab or wire type of structures of atoms with a vacuum region so that infinitely repeated supercell would resemble a system with an infinite number of slabs or wires separated by vacuum [21]. However, fitting of the local psedudopotential $V(q)$ for bulk semiconductors is insufficient for confined structures since long wavelength (small q) components of $V(q)$ relavant to the workfunction cannot be explicitly determined [59] from the electronic properties of bulk semiconductors. Thus it is obvious to calibrate correctly the workfunctions and band-alignment for the confined structures and theses properties can be fitted by calibrating $V(q = 0)$ [59, 10].

In this dissertation, we discuss the EPM applied to relaxed and strained, and bulk, 1D and 2D confined semiconductors, emphasizing the local form-factors interpolation with correct workfunction. Our results include comprehensive informations regarding the electronic structures of theses semiconductors such as band structure, effective masses, deformation potentials, band gap and effective mass bowing parameters, density of states and ballistic conductances. This dissertation is organized as follows : In Chap. 2 and 3 we review the elasticity theory and empirical pseudopotential theory, respectively, in detail. In Chap. 4 we present calculated band structure results and bench mark to numerous experimental data for relaxed and strained bulk Si, Ge, III-Vs and their alloys. In Chap. 5 we discuss the transferability of the local pseudopotential $V(q)$ when we extend the EPM to nanometer-scale systems using supercell method. In Chap. 6 we discuss the band alignment problem between the Si and Ge and present band structure results for 1D confined systems, Si thin- and $Si/Si_{1-x}Ge_x/Si$ hetero-layers. In Chap. 7 we present band structure results for relaxed and uniaxially strained Si NWs and the transport relavant quantities such as ballistic conductance and effective masses are also evaluated. Then some conclusions is followed in Chap. 8.

CHAPTER 2

ELASTICITY THEORY

2.1 Review

We review the elasticity theory in detail to show how to derive the strain tensor e and the deformation tensor ϵ which is necessary to deal with a crystal structure with strain. The strain tensor e_{ij} and stress tensor σ_{ij} are related by the compliances tensor S_{ijkl} and the stiffness tensor C_{ijkl}.

$$\begin{aligned} e_{ij} &= S_{ijkl}\sigma_{kl} \\ \sigma_{ij} &= C_{ijkl}e_{kl} \end{aligned} \tag{2.1}$$

Both S_{ijkl} and C_{ijkl} are fourth rank tensor which has total 81 components. By symmetry of the crystal structure in which assume that there is no net torque when we apply the stress, the number of independent constants of S_{ijkl} and C_{ijkl} are reduced to 36 from 81. And also, the symmetry of S_{ijkl} and C_{ijkl} in the first two and the last two suffixes makes it possible to use the matrix notation. Both stress components and strain components are written with a single suffix running from 1 to 6. [64]

$$\boldsymbol{\sigma} = \begin{bmatrix} \sigma_{11} & \sigma_{12} & \sigma_{31} \\ \sigma_{12} & \sigma_{22} & \sigma_{23} \\ \sigma_{31} & \sigma_{23} & \sigma_{33} \end{bmatrix} = \begin{bmatrix} \sigma_1 & \sigma_6 & \sigma_5 \\ \sigma_6 & \sigma_2 & \sigma_4 \\ \sigma_5 & \sigma_4 & \sigma_3 \end{bmatrix} \tag{2.2}$$

and

$$\mathbf{e} = \begin{bmatrix} e_{11} & e_{12} & e_{31} \\ e_{12} & e_{22} & e_{23} \\ e_{31} & e_{23} & e_{33} \end{bmatrix} = \begin{bmatrix} e_1 & \frac{1}{2}e_6 & \frac{1}{2}e_5 \\ \frac{1}{2}e_6 & e_2 & \frac{1}{2}e_4 \\ \frac{1}{2}e_5 & \frac{1}{2}e_4 & e_3 \end{bmatrix} \tag{2.3}$$

In the S_{ijkl} and the C_{ijkl}, the first two suffices are abbreviated into a single one running from 1 to 6, the last two are abbreviated in the same way.

tensor notation	11	22	33	23,32	31,13	12,21
matrix notation	1	2	3	4	5	6

At the same time, factors of 2 and 4 are introduced as follows;

$S_{ijkl} = S_{mn}$ when m and n are 1, 2 or 3

$2S_{ijkl} = S_{mn}$ when either m or n are 4, 5 or 6

$4S_{ijkl} = S_{mn}$ when both m and n are 4, 5 or 6

Now consider Eq. 2.1 written out for e_{11} and e_{23}. For example,

$$\begin{aligned} e_{11} &= S_{1111}\sigma_{11} + S_{1112}\sigma_{12} + S_{1113}\sigma_{13} \\ &+ S_{1121}\sigma_{21} + S_{1122}\sigma_{22} + S_{1123}\sigma_{23} \\ &+ S_{1131}\sigma_{31} + S_{1132}\sigma_{32} + S_{1133}\sigma_{33} \end{aligned} \tag{2.4}$$

then the Eq. 2.4 in the matrix notation combined with Eq. 2.3 becomes,

$$\begin{aligned} e_1 &= S_{11}\sigma_1 + \frac{1}{2}S_{16}\sigma_6 + \frac{1}{2}S_{15}\sigma_5 \\ &+ \frac{1}{2}S_{16}\sigma_6 + S_{12}\sigma_2 + \frac{1}{2}S_{14}\sigma_4 \\ &+ \frac{1}{2}S_{15}\sigma_5 + \frac{1}{2}S_{14}\sigma_4 + S_{13}\sigma_3 \\ &= S_{11}\sigma_1 + S_{12}\sigma_2 + S_{13}\sigma_3 + S_{14}\sigma_4 + S_{15}\sigma_5 + S_{16}\sigma_6 \end{aligned} \tag{2.5}$$

and also in the matrix notation

$$\begin{aligned} e_{23} &= S_{2311}\sigma_{11} + S_{2312}\sigma_{12} + S_{2313}\sigma_{13} \\ &+ S_{2321}\sigma_{21} + S_{2322}\sigma_{22} + S_{2323}\sigma_{23} \\ &+ S_{2331}\sigma_{31} + S_{2332}\sigma_{32} + S_{2333}\sigma_{33} \end{aligned} \tag{2.6}$$

then Eq. 2.6 combined with Eq. 2.3 becomes,

$$\begin{aligned} \frac{1}{2}e_4 &= \frac{1}{2}S_{41}\sigma_1 + \frac{1}{4}S_{46}\sigma_6 + \frac{1}{4}S_{45}\sigma_5 \\ &+ \frac{1}{4}S_{46}\sigma_6 + \frac{1}{2}S_{42}\sigma_2 + \frac{1}{4}S_{44}\sigma_4 \\ &+ \frac{1}{4}S_{45}\sigma_5 + \frac{1}{4}S_{44}\sigma_4 + \frac{1}{2}S_{43}\sigma_3 \\ &= \frac{1}{2}\left\{S_{41}\sigma_1 + S_{42}\sigma_2 + S_{43}\sigma_3 + S_{44}\sigma_4 + S_{45}\sigma_5 + S_{46}\sigma_6\right\} \end{aligned} \tag{2.7}$$

Therefore, in general, Eq. 2.1 takes simple form of

$$e_i = S_{ij}\sigma_j \quad (i,j = 1,2,..,6) \tag{2.8}$$

The reason for introducing the 2's and 4's into the definitions of S_{ij} is to avoid the appearance of 2's and 4's in Eq. 2.8 and to make it possible to write this equation in a compact form. For the C_{ijkl}, no factors of 2 or 4 are necessary. If we simply write

$$C_{ijkl} = C_{mn} \quad (i,j,k,l = 1,2,3; m,n = 1,2,..,6) \tag{2.9}$$

then it may be shown by writing out some typical members that Eq. 2.1 take the simple form

$$\sigma_i = C_{ij}e_j \quad (i,j = 1,2,..,6) \tag{2.10}$$

Now, the matrix form of S_{ij} and C_{ij} becomes,

$$S_{ij} = \begin{bmatrix} S_{11} & S_{12} & S_{13} & S_{14} & S_{15} & S_{16} \\ S_{21} & S_{22} & S_{23} & S_{24} & S_{25} & S_{26} \\ S_{31} & S_{32} & S_{33} & S_{34} & S_{35} & S_{36} \\ S_{41} & S_{42} & S_{43} & S_{44} & S_{45} & S_{46} \\ S_{51} & S_{52} & S_{53} & S_{54} & S_{55} & S_{56} \\ S_{61} & S_{62} & S_{63} & S_{64} & S_{65} & S_{66} \end{bmatrix} \tag{2.11}$$

and

$$C_{ij} = \begin{bmatrix} C_{11} & C_{12} & C_{13} & C_{14} & C_{15} & C_{16} \\ C_{21} & C_{22} & C_{23} & C_{24} & C_{25} & C_{26} \\ C_{31} & C_{32} & C_{33} & C_{34} & C_{35} & C_{36} \\ C_{41} & C_{42} & C_{43} & C_{44} & C_{45} & C_{46} \\ C_{51} & C_{52} & C_{53} & C_{54} & C_{55} & C_{56} \\ C_{61} & C_{62} & C_{63} & C_{64} & C_{65} & C_{66} \end{bmatrix} \tag{2.12}$$

For cubic crystals, the number of independent stiffness and compliance constants can be reduced further by the possession of symmetry elements [46]. By considering minimum symmetry requirement for a cubic crystal structure, the compliance and stiffness matrix in Eq. 2.11 and 2.12, respectively, can be simply expressed by [98]

$$S = \begin{bmatrix} S_{11} & S_{12} & S_{12} & 0 & 0 & 0 \\ S_{12} & S_{11} & S_{12} & 0 & 0 & 0 \\ S_{12} & S_{12} & S_{11} & 0 & 0 & 0 \\ 0 & 0 & 0 & S_{44} & 0 & 0 \\ 0 & 0 & 0 & 0 & S_{44} & 0 \\ 0 & 0 & 0 & 0 & 0 & S_{44} \end{bmatrix} \tag{2.13}$$

and

$$C = \begin{bmatrix} C_{11} & C_{12} & C_{12} & 0 & 0 & 0 \\ C_{12} & C_{11} & C_{12} & 0 & 0 & 0 \\ C_{12} & C_{12} & C_{11} & 0 & 0 & 0 \\ 0 & 0 & 0 & C_{44} & 0 & 0 \\ 0 & 0 & 0 & 0 & C_{44} & 0 \\ 0 & 0 & 0 & 0 & 0 & C_{44} \end{bmatrix} \tag{2.14}$$

where the stiffness and compliance constants for the cubic crystals are related by

$$\begin{aligned} C_{11} - C_{12} &= \frac{1}{S_{11} - S_{12}} \\ C_{11} + 2C_{12} &= \frac{1}{S_{11} + 2S_{12}} \\ C_{44} &= \frac{1}{S_{44}} \end{aligned} \tag{2.15}$$

and

$$\begin{aligned} S_{11} &= \frac{C_{11} + C_{12}}{(C_{11} + 2C_{12})(C_{11} - C_{12})} \\ S_{12} &= \frac{-C_{12}}{(C_{11} + 2C_{12})(C_{11} - C_{12})} \\ S_{44} &= \frac{1}{C_{44}} \end{aligned} \tag{2.16}$$

Thus, Eq. 2.8 can be expressed in a matrix equation as,

$$\begin{bmatrix} e_1 \\ e_2 \\ e_3 \\ e_4 \\ e_5 \\ e_6 \end{bmatrix} = \begin{bmatrix} S_{11} & S_{12} & S_{12} & 0 & 0 & 0 \\ S_{12} & S_{11} & S_{12} & 0 & 0 & 0 \\ S_{12} & S_{12} & S_{11} & 0 & 0 & 0 \\ 0 & 0 & 0 & S_{44} & 0 & 0 \\ 0 & 0 & 0 & 0 & S_{44} & 0 \\ 0 & 0 & 0 & 0 & 0 & S_{44} \end{bmatrix} \begin{bmatrix} \sigma_1 \\ \sigma_2 \\ \sigma_3 \\ \sigma_4 \\ \sigma_5 \\ \sigma_6 \end{bmatrix} \tag{2.17}$$

which is equivalent to,

$$\begin{bmatrix} e_{11} \\ e_{22} \\ e_{33} \\ 2e_{23} \\ 2e_{31} \\ 2e_{12} \end{bmatrix} = \begin{bmatrix} S_{11} & S_{12} & S_{12} & 0 & 0 & 0 \\ S_{12} & S_{11} & S_{12} & 0 & 0 & 0 \\ S_{12} & S_{12} & S_{11} & 0 & 0 & 0 \\ 0 & 0 & 0 & S_{44} & 0 & 0 \\ 0 & 0 & 0 & 0 & S_{44} & 0 \\ 0 & 0 & 0 & 0 & 0 & S_{44} \end{bmatrix} \begin{bmatrix} \sigma_{11} \\ \sigma_{22} \\ \sigma_{33} \\ \sigma_{23} \\ \sigma_{31} \\ \sigma_{12} \end{bmatrix} \tag{2.18}$$

In a familiar coordinate axis representation, Eq. 2.18 can be expressed as,

$$\begin{bmatrix} e_{xx} \\ e_{yy} \\ e_{zz} \\ e_{yz} \\ e_{zx} \\ e_{xy} \end{bmatrix} = \begin{bmatrix} S_{11} & S_{12} & S_{12} & 0 & 0 & 0 \\ S_{12} & S_{11} & S_{12} & 0 & 0 & 0 \\ S_{12} & S_{12} & S_{11} & 0 & 0 & 0 \\ 0 & 0 & 0 & \frac{S_{44}}{2} & 0 & 0 \\ 0 & 0 & 0 & 0 & \frac{S_{44}}{2} & 0 \\ 0 & 0 & 0 & 0 & 0 & \frac{S_{44}}{2} \end{bmatrix} \begin{bmatrix} \sigma_{xx} \\ \sigma_{yy} \\ \sigma_{zz} \\ \sigma_{yz} \\ \sigma_{zx} \\ \sigma_{xy} \end{bmatrix} \tag{2.19}$$

where the first subscript of σ indicates the direction of the force and the second subscript indicates the normal to the plane to which the force is applied. For example, σ_{xx} represents the force toward x direction on the plane noraml to the x axis and σ_{yz} represents the force toward y direction on the plane normal to the z axis as shown in Fig. 2.1. Using Eq. 2.19, we can express the constant D, so called 'Poisson's ratio', as a function of the elastic constants C_{11}, C_{12} and C_{44} for both biaxial and uniaxial strain on different crystal orientations, (001), (110) and (111). The D is defined by the ratio of $\epsilon_{\perp}$ and $\epsilon_{\parallel}$ which are the strain components perpendicular and parallel to the interface, respectively [85].

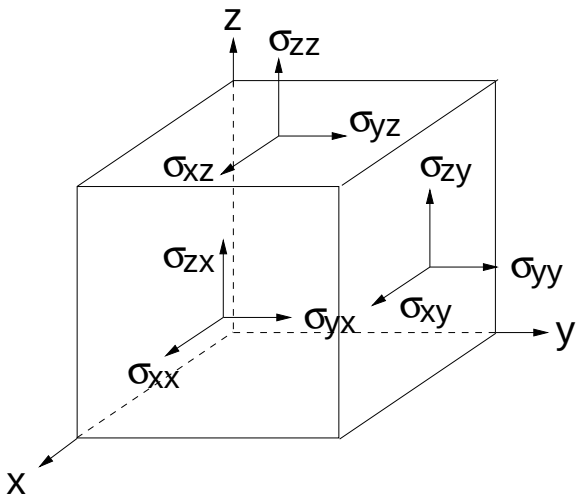

Figure 2.1. Stress tensor notation in cartesian coordinate system.

$$\epsilon_{\perp} = -D\epsilon_{\parallel}$$
$$D = -\frac{\epsilon_{\perp}}{\epsilon_{\parallel}} \tag{2.20}$$

where the $\epsilon_{\perp}$ and $\epsilon_{\parallel}$ are defined as,

$$\epsilon_{\perp} = \vec{v}_{\perp}^{T} \cdot \bar{e} \cdot \vec{v}_{\perp}$$
$$\epsilon_{\parallel} = \vec{v}_{\parallel}^{T} \cdot \bar{e} \cdot \vec{v}_{\parallel} \tag{2.21}$$

where the $\vec{v}_{\perp}$ and $\vec{v}_{\parallel}$ are vectors perpendicular and parallel to the given crystal interface, respectively. Using the above relations, we can express the $e_{\perp}$ and $e_{\parallel}$ in terms of the strain components i.e. e_{xx}, e_{yy} and so on, for various crystal orientations.

2.2 Strain tensor

As we mentioned in the previous section, $e_{\perp}$ and $e_{\parallel}$ can be expressed as a function of strain tensor components for different crystal orientations. In this section, we show how the $e_{\perp}$ and $e_{\parallel}$ can be derived for (001), (110) and (111) interfaces.

2.2.1 (001) Interface

On the (001) crystal interface, the vector parallel to the interface, $\vec{v}_{\parallel}$, can be either $[010]^T$ or $[100]^T$ and the vector perpendicular to the interface, $\vec{v}_{\perp}$, is $[001]^T$. Using Eq. 2.3 and 2.21, we can easily show,

$$\begin{aligned}
\epsilon_{\perp} &= \vec{v}_{\perp}^{T} \cdot \bar{e} \cdot \vec{v}_{\perp} = \begin{bmatrix} 0 & 0 & 1 \end{bmatrix} \begin{bmatrix} e_{xx} & e_{xy} & e_{zx} \\ e_{xy} & e_{yy} & e_{yz} \\ e_{zx} & e_{yz} & e_{zz} \end{bmatrix} \begin{bmatrix} 0 \\ 0 \\ 1 \end{bmatrix} = e_{zz} \\
\epsilon_{\parallel,(1)} &= \vec{v}_{\parallel,(1)}^{T} \cdot \bar{e} \cdot \vec{v}_{\parallel,(1)} = \begin{bmatrix} 0 & 1 & 0 \end{bmatrix} \begin{bmatrix} e_{xx} & e_{xy} & e_{zx} \\ e_{xy} & e_{yy} & e_{yz} \\ e_{zx} & e_{yz} & e_{zz} \end{bmatrix} \begin{bmatrix} 0 \\ 1 \\ 0 \end{bmatrix} = e_{yy} \\
\epsilon_{\parallel,(2)} &= \vec{v}_{\parallel,(2)}^{T} \cdot \bar{e} \cdot \vec{v}_{\parallel,(2)} = \begin{bmatrix} 1 & 0 & 0 \end{bmatrix} \begin{bmatrix} e_{xx} & e_{xy} & e_{zx} \\ e_{xy} & e_{yy} & e_{yz} \\ e_{zx} & e_{yz} & e_{zz} \end{bmatrix} \begin{bmatrix} 1 \\ 0 \\ 0 \end{bmatrix} = e_{xx}
\end{aligned} \tag{2.22}$$

Also, if we assume that the strain applied to the (001) interface is biaxial and uniform, then

$$\epsilon_{\parallel,(1)} = \epsilon_{\parallel,(2)}$$

and thus, the $e_{\perp}$ and $e_{\parallel}$ becomes,

$$\begin{aligned}
\epsilon_{\perp} &= e_{zz} \\
\epsilon_{\parallel} &= e_{xx} = e_{yy}
\end{aligned} \tag{2.23}$$

2.2.2 (110) Interface

In the case of (110) interface, the $\vec{v}_{\perp}$ and $\vec{v}_{\parallel}$ are,

$$\vec{v}_{\perp} = \begin{bmatrix} \frac{1}{\sqrt{2}} & \frac{1}{\sqrt{2}} & 0 \end{bmatrix}^T$$
$$\vec{v}_{\parallel,(1)} = \begin{bmatrix} \frac{1}{\sqrt{2}} & \frac{-1}{\sqrt{2}} & 0 \end{bmatrix}^T$$
$$\vec{v}_{\parallel,(2)} = \begin{bmatrix} 0 & 0 & 1 \end{bmatrix}^T \tag{2.24}$$

Using Eq. 2.3 and 2.21,

$$\epsilon_{\perp} = \vec{v}_{\perp}^T \cdot \bar{e} \cdot \vec{v}_{\perp} = \begin{bmatrix} \frac{1}{\sqrt{2}} & \frac{1}{\sqrt{2}} & 0 \end{bmatrix} \begin{bmatrix} e_{xx} & e_{xy} & e_{zx} \\ e_{xy} & e_{yy} & e_{yz} \\ e_{zx} & e_{yz} & e_{zz} \end{bmatrix} \begin{bmatrix} \frac{1}{\sqrt{2}} \\ \frac{1}{\sqrt{2}} \\ 0 \end{bmatrix} = \frac{1}{2}\left(e_{xx} + 2e_{xy} + e_{yy}\right)$$
$$\epsilon_{\parallel,(1)} = \vec{v}_{\parallel,(1)}^T \cdot \bar{e} \cdot \vec{v}_{\parallel,(1)} = \begin{bmatrix} \frac{1}{\sqrt{2}} & \frac{-1}{\sqrt{2}} & 0 \end{bmatrix} \begin{bmatrix} e_{xx} & e_{xy} & e_{zx} \\ e_{xy} & e_{yy} & e_{yz} \\ e_{zx} & e_{yz} & e_{zz} \end{bmatrix} \begin{bmatrix} \frac{1}{\sqrt{2}} \\ \frac{-1}{\sqrt{2}} \\ 0 \end{bmatrix} = \frac{1}{2}\left(e_{xx} - 2e_{xy} + e_{yy}\right)$$
$$\epsilon_{\parallel,(2)} = \vec{v}_{\parallel,(2)}^T \cdot \bar{e} \cdot \vec{v}_{\parallel,(2)} = \begin{bmatrix} 0 & 0 & 1 \end{bmatrix} \begin{bmatrix} e_{xx} & e_{xy} & e_{zx} \\ e_{xy} & e_{yy} & e_{yz} \\ e_{zx} & e_{yz} & e_{zz} \end{bmatrix} \begin{bmatrix} 0 \\ 0 \\ 1 \end{bmatrix} = e_{zz} \tag{2.25}$$

The uniform biaxial strain implies that $e_{xx} = e_{yy}$. Therefore,

$$\epsilon_{\perp} = \frac{1}{2}\left(e_{xx} + 2e_{xy} + e_{yy}\right) = e_{xx} + e_{xy}$$
$$\epsilon_{\parallel,(1)} = \frac{1}{2}\left(e_{xx} - 2e_{xy} + e_{yy}\right) = e_{xx} - e_{xy}$$
$$\epsilon_{\parallel,(2)} = e_{zz} \tag{2.26}$$

By the uniform biaxial strain condition on the plane, $\epsilon_{\parallel,(1)} = \epsilon_{\parallel,(2)}$, following relation

$$e_{xx} - e_{xy} = e_{zz} \tag{2.27}$$

should be satisfied. Therefore, the $\epsilon_{\parallel}$ and $\epsilon_{\perp}$ in terms of strain tensor components becomes,

$$\begin{aligned}\epsilon_{\perp} &= e_{xx} + e_{xy} \\ \epsilon_{\parallel} &= e_{xx} - e_{xy} = e_{zz}\end{aligned} \tag{2.28}$$

which in turn,

$$\begin{aligned}e_{xx} &= \frac{1}{2}\left(\epsilon_{\perp} + \epsilon_{\parallel}\right) \\ e_{yy} &= \frac{1}{2}\left(\epsilon_{\perp} + \epsilon_{\parallel}\right) \\ e_{xy} &= \frac{1}{2}\left(\epsilon_{\perp} - \epsilon_{\parallel}\right) \\ e_{zz} &= \epsilon_{\parallel}\end{aligned} \tag{2.29}$$

2.2.3 (111) Interface

In the case of (111) interface, the $\vec{v}_{\perp}$ and $\vec{v}_{\parallel}$ are,

$$\begin{aligned}\vec{v}_{\perp} &= \begin{bmatrix}\frac{1}{\sqrt{3}} & \frac{1}{\sqrt{3}} & \frac{1}{\sqrt{3}}\end{bmatrix}^T \\ \vec{v}_{\parallel,(1)} &= \begin{bmatrix}\frac{1}{\sqrt{2}} & \frac{-1}{\sqrt{2}} & 0\end{bmatrix}^T \\ \vec{v}_{\parallel,(2)} &= \begin{bmatrix}\frac{1}{\sqrt{6}} & \frac{1}{\sqrt{6}} & \frac{-2}{\sqrt{6}}\end{bmatrix}^T\end{aligned} \tag{2.30}$$

Using Eq. 2.3 and 2.21,

$$\begin{aligned}\epsilon_{\perp} &= \vec{v}_{\perp}^{T} \cdot \bar{e} \cdot \vec{v}_{\perp} = \frac{1}{3}\left[e_{xx} + e_{yy} + e_{zz} + 2\left(e_{xy} + e_{zx} + e_{yz}\right)\right] \\ \epsilon_{\parallel,(1)} &= \vec{v}_{\parallel,(1)}^{T} \cdot \bar{e} \cdot \vec{v}_{\parallel,(1)} = \frac{1}{2}\left(e_{xx} + e_{yy} - 2e_{xy}\right) \\ \epsilon_{\parallel,(2)} &= \vec{v}_{\parallel,(2)}^{T} \cdot \bar{e} \cdot \vec{v}_{\parallel,(2)} = \frac{1}{6}\left(e_{xx} + 2e_{xy} + e_{yy} - 4e_{yz} - 4e_{zx} + 4e_{zz}\right)\end{aligned} \tag{2.31}$$

The uniform biaxial strain implies that

$$\begin{aligned} e_{xx} &= e_{yy} = e_{zz} \\ e_{xy} &= e_{zx} = e_{yz} \end{aligned} \tag{2.32}$$

resulting in rather simple expressions of Eq. 2.31,

$$\begin{aligned} \epsilon_{\perp} &= e_{xx} + 2e_{xy} \\ \epsilon_{\parallel,(1)} &= \epsilon_{\parallel,(2)} = e_{xx} - e_{xy} \end{aligned} \tag{2.33}$$

and also,

$$\begin{aligned} e_{xx} = e_{yy} = e_{zz} &= \frac{1}{3}\left(\epsilon_{\perp} + 2\epsilon_{\parallel}\right) \\ e_{xy} = e_{zx} = e_{yz} &= \frac{1}{3}\left(\epsilon_{\perp} - \epsilon_{\parallel}\right) \end{aligned} \tag{2.34}$$

2.3 Poisson's Ratio

As we mentioned, the 'Poisson's ratio' D is a quantity that is defined by the ratio of $\epsilon_{\perp}$ and $\epsilon_{\parallel}$ which depend on the crystal orientation and types of strain. In this section, we show a detail derivation of the D in the case of biaxial and uniaxial along different crystal orientaions.

2.3.1 Biaxial Strain

2.3.1.1 (001) Biaxial Strain

We assume that the magnitude of the biaxial stress is not uniform which is more general on the (001) interface and define the magnitude of the force per unit area in σ_{xx} direction is σ_1 and in σ_{yy} direction is σ_2 as shown in Fig. 2.2.

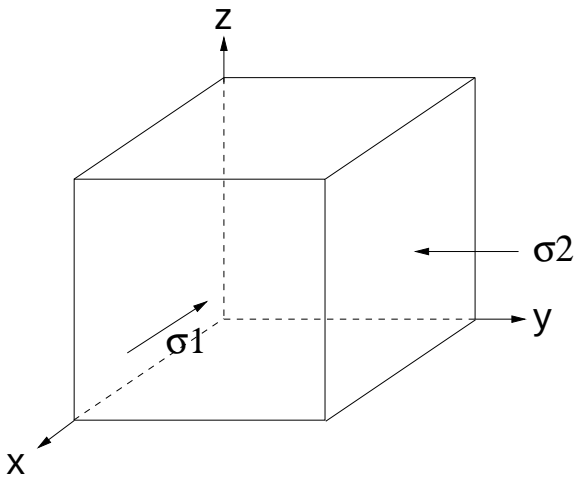

Figure 2.2. Non-uniform (001) biaxial stress where the magnitude of stress tensor components σ_{xx} and σ_{yy} are denoted as σ_1 and σ_1, respectively.

From Eq. 2.19, the strain tensor under (001) non-uniform biaxial stress can be expressed as,

$$\begin{bmatrix} e_{xx} \\ e_{yy} \\ e_{zz} \\ e_{yz} \\ e_{zx} \\ e_{xy} \end{bmatrix} = \begin{bmatrix} S_{11} & S_{12} & S_{12} & 0 & 0 & 0 \\ S_{12} & S_{11} & S_{12} & 0 & 0 & 0 \\ S_{12} & S_{12} & S_{11} & 0 & 0 & 0 \\ 0 & 0 & 0 & \frac{S_{44}}{2} & 0 & 0 \\ 0 & 0 & 0 & 0 & \frac{S_{44}}{2} & 0 \\ 0 & 0 & 0 & 0 & 0 & \frac{S_{44}}{2} \end{bmatrix} \begin{bmatrix} \sigma_1 \\ \sigma_2 \\ 0 \\ 0 \\ 0 \\ 0 \end{bmatrix} \tag{2.35}$$

then, we can show

$$\begin{aligned} e_{xx} &= S_{11}\sigma_1 + S_{12}\sigma_2 \\ e_{yy} &= S_{12}\sigma_1 + S_{11}\sigma_2 \\ e_{zz} &= S_{12}\sigma_1 + S_{12}\sigma_2 \end{aligned} \tag{2.36}$$

If we assume that the biaxial stress is uniform, eg. $\sigma_1 = \sigma_2$, then Eq. 2.36 becomes,

$$
\begin{aligned}
e_{xx} &= (S_{11} + S_{12})\,\sigma_1 \\
e_{yy} &= (S_{12} + S_{11})\,\sigma_1 \\
e_{zz} &= 2S_{12}\sigma_1
\end{aligned} \tag{2.37}
$$

Thus, we can show that the $\epsilon_\perp$ and $\epsilon_\parallel$ in terms of σ_1 using Eq. 2.23,

$$
\begin{aligned}
\epsilon_\perp &= e_{zz} = 2\sigma_1 \\
\epsilon_\parallel &= e_{xx} = e_{yy} = (S_{12} + S_{11})\,\sigma_1
\end{aligned} \tag{2.38}
$$

and the 'Poisson's ratio' D_{001} for uniform biaxial strain becomes,

$$
\begin{aligned}
D_{001}^{bi} &= -\frac{\epsilon_\perp}{\epsilon_\parallel} = -\frac{2S_{12}\sigma_1}{(S_{11} + S_{12})\,\sigma_1} \\
&= -\frac{2S_{12}}{S_{11} + S_{12}} = -\frac{-2C_{12}}{C_{11} + C_{12} - C_{12}} \\
&= \frac{2C_{12}}{C_{11}}
\end{aligned} \tag{2.39}
$$

The strain tensor in terms of the $\epsilon_\perp$ and $\epsilon_\parallel$ can be written,

$$
\mathbf{e} = \begin{bmatrix} e_{xx} & e_{xy} & e_{zx} \\ e_{xy} & e_{yy} & e_{yz} \\ e_{zx} & e_{yz} & e_{zz} \end{bmatrix} = \begin{bmatrix} \epsilon_\parallel & 0 & 0 \\ 0 & \epsilon_\parallel & 0 \\ 0 & 0 & \epsilon_\perp \end{bmatrix} \tag{2.40}
$$

2.3.1.2 (110) Biaxial Strain

For (110) biaxial strain, biaxial stress applied to the (110) interface is not as easy as the (001) biaxial stress to decompose into stress components which requires us to use the property of cubic crystal. For cubic crystal structure, the crystal structure is invariant under rotational transformation with respect to the original coordinate system. Thus we can transform the original coordinate system $[xyz]^T$ to the coordinate $[x'y'z']^T$ as shown in Fig. 2.3 by use of the rotational transformation matrix Q,

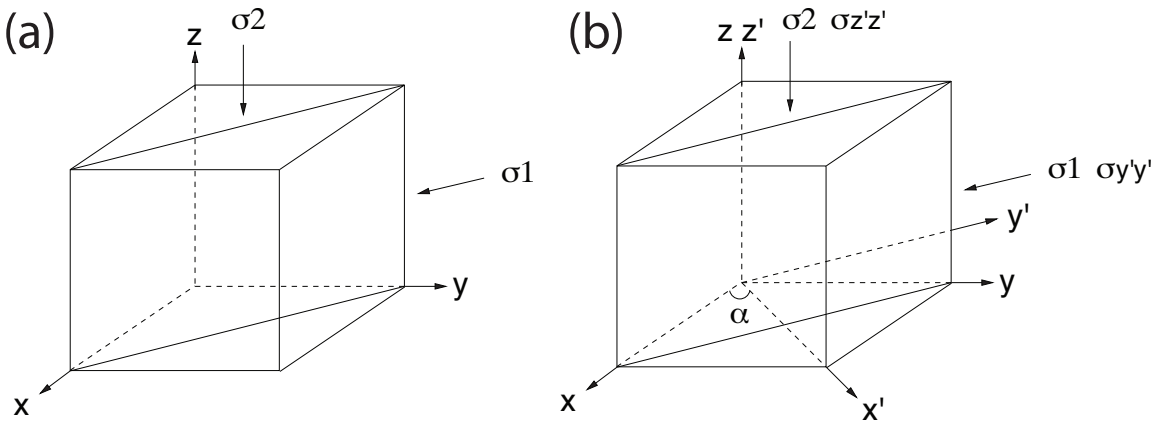

Figure 2.3. (a) Non-uniform (110) biaxial stress where the magnitude of stress tensor components σ_{xy} and σ_{zz} are denoted as σ_1 and σ_1, respectively. (b) Rotational transformation of coordinate system of (110) biaxial stress.

where the Q has a property that $Q^{-1} = Q^T$. The rotational transformation matrix Q about the z-axis by an angle α is given by,

$$Q = \begin{bmatrix} \cos\alpha & \sin\alpha & 0 \\ -\sin\alpha & \cos\alpha & 0 \\ 0 & 0 & 1 \end{bmatrix} \tag{2.41}$$

and

$$\sigma' = Q\sigma Q^{-1} \tag{2.42}$$

where the σ' and σ are the stress tensor in the rotated coordinate system and the original system, respectively and the σ' in terms of σ_1 and σ_2 can be written,

$$\sigma' = \begin{bmatrix} \sigma_{x'x'} & \sigma_{x'y'} & \sigma_{z'x'} \\ \sigma_{x'y'} & \sigma_{y'y'} & \sigma_{y'z'} \\ \sigma_{z'x'} & \sigma_{y'z'} & \sigma_{z'z'} \end{bmatrix} = \begin{bmatrix} 0 & 0 & 0 \\ 0 & \sigma_1 & 0 \\ 0 & 0 & \sigma_2 \end{bmatrix} \tag{2.43}$$

Thus, the stress tensor σ in the original coordinate system becomes,

$$
\begin{aligned}
\sigma &= Q^{-1}\sigma' Q \\
&= \begin{bmatrix} \frac{1}{\sqrt{2}} & \frac{-1}{\sqrt{2}} & 0 \\ \frac{1}{\sqrt{2}} & \frac{1}{\sqrt{2}} & 0 \\ 0 & 0 & 1 \end{bmatrix} \begin{bmatrix} 0 & 0 & 0 \\ 0 & \sigma_1 & 0 \\ 0 & 0 & \sigma_2 \end{bmatrix} \begin{bmatrix} \frac{1}{\sqrt{2}} & \frac{1}{\sqrt{2}} & 0 \\ \frac{-1}{\sqrt{2}} & \frac{1}{\sqrt{2}} & 0 \\ 0 & 0 & 1 \end{bmatrix} \\
&= \begin{bmatrix} \frac{\sigma_1}{2} & -\frac{\sigma_1}{2} & 0 \\ -\frac{\sigma_1}{2} & \frac{\sigma_1}{2} & 0 \\ 0 & 0 & \sigma_2 \end{bmatrix}
\end{aligned} \tag{2.44}
$$

Using Eq. 2.19, the strain tensor under (110) non-uniform biaxial stress can be expressed as,

$$
\begin{bmatrix} e_{xx} \\ e_{yy} \\ e_{zz} \\ e_{yz} \\ e_{zx} \\ e_{xy} \end{bmatrix} = \begin{bmatrix} S_{11} & S_{12} & S_{12} & 0 & 0 & 0 \\ S_{12} & S_{11} & S_{12} & 0 & 0 & 0 \\ S_{12} & S_{12} & S_{11} & 0 & 0 & 0 \\ 0 & 0 & 0 & \frac{S_{44}}{2} & 0 & 0 \\ 0 & 0 & 0 & 0 & \frac{S_{44}}{2} & 0 \\ 0 & 0 & 0 & 0 & 0 & \frac{S_{44}}{2} \end{bmatrix} \begin{bmatrix} \frac{\sigma_1}{2} \\ \frac{\sigma_1}{2} \\ \sigma_2 \\ 0 \\ 0 \\ -\frac{\sigma_1}{2} \end{bmatrix} = \begin{bmatrix} \frac{S_{11}}{2}\sigma_1 + \frac{S_{12}}{2}\sigma_1 + S_{12}\sigma_2 \\ \frac{S_{11}}{2}\sigma_1 + \frac{S_{12}}{2}\sigma_1 + S_{12}\sigma_2 \\ S_{12}\sigma_1 + S_{11}\sigma_2 \\ 0 \\ 0 \\ -\frac{S_{44}\sigma_1}{4} \end{bmatrix} \tag{2.45}
$$

From the uniform biaxial strain condition Eq. 2.28,

$$
\frac{S_{11}}{2}\sigma_1 + \frac{S_{12}}{2}\sigma_1 + S_{12}\sigma_2 + \frac{S_{44}}{4}\sigma_1 = S_{12}\sigma_1 + S_{11}\sigma_2 \tag{2.46}
$$

then we can determine the relation between σ_1 and σ_2.

$$
\sigma_2 = \frac{2S_{11} - 2S_{12} + S_{44}}{4\left(S_{11} - S_{12}\right)}\sigma_1 \tag{2.47}
$$

By substituting Eq. 2.47 into he right hand side of Eq. 2.45 we can show,

$$
\begin{aligned}
e_{xx} &= \sigma_1 \left\{ \frac{S_{11}}{2} + \frac{S_{12}}{2} + \frac{S_{12}\left(2S_{11} - 2S_{12} + S_{44}\right)}{4\left(S_{11} - S_{12}\right)} \right\} \\
e_{yy} &= \sigma_1 \left\{ \frac{S_{11}}{2} + \frac{S_{12}}{2} + \frac{S_{12}\left(2S_{11} - 2S_{12} + S_{44}\right)}{4\left(S_{11} - S_{12}\right)} \right\} \\
e_{zz} &= \sigma_1 \left\{ S_{12} + \frac{S_{11}\left(2S_{11} - 2S_{12} + S_{44}\right)}{4\left(S_{11} - S_{12}\right)} \right\} \\
e_{yz} &= 0 \\
e_{zx} &= 0 \\
e_{xy} &= -\frac{S_{44}}{4}\sigma_1
\end{aligned}
\tag{2.48}
$$

Thus, we can show that the $\epsilon_\perp$ and $\epsilon_\parallel$ in terms of σ_1 using Eq. 2.28,

$$
\begin{aligned}
\epsilon_\perp &= e_{xx} + e_{xy} = \frac{\left\{2S_{11}^2 + S_{11}\left(2S_{12} - S_{44}\right) + 2S_{12}\left(S_{44} - 2S_{12}\right)\right\}}{4\left(S_{11} - S_{12}\right)}\sigma_1 \\
\epsilon_\parallel &= e_{xx} - e_{xy} = e_{zz} = \left\{ S_{12} + \frac{S_{11}\left(2S_{11} - 2S_{12} + S_{44}\right)}{4\left(S_{11} - S_{12}\right)} \right\} \sigma_1
\end{aligned}
\tag{2.49}
$$

and the D_{110} for uniform biaxial strain of the (110) interface becomes,

$$
\begin{aligned}
D_{110}^{bi} &= -\frac{\epsilon_\perp}{\epsilon_\parallel} \\
&= -\frac{2S_{11}^2 + 2S_{11}S_{12} - 4S_{12}^2 - S_{11}S_{44} + 2S_{12}S_{44}}{2S_{11}^2 + 2S_{11}S_{12} - 4S_{12}^2 + S_{11}S_{44}} \\
&= \frac{C_{11} + 3C_{12} - 2C_{44}}{C_{11} + C_{12} + 2C_{44}}
\end{aligned}
\tag{2.50}
$$

The strain tensor in terms of the $\epsilon_\perp$ and $\epsilon_\parallel$ can be written,

$$
\mathbf{e} = \begin{bmatrix} e_{xx} & e_{xy} & e_{zx} \\ e_{xy} & e_{yy} & e_{yz} \\ e_{zx} & e_{yz} & e_{zz} \end{bmatrix} = \begin{bmatrix} \frac{1}{2}\left(\epsilon_\perp + \epsilon_\parallel\right) & \frac{1}{2}\left(\epsilon_\perp - \epsilon_\parallel\right) & 0 \\ \frac{1}{2}\left(\epsilon_\perp - \epsilon_\parallel\right) & \frac{1}{2}\left(\epsilon_\perp + \epsilon_\parallel\right) & 0 \\ 0 & 0 & \epsilon_\parallel \end{bmatrix}
\tag{2.51}
$$

2.3.1.3 (111) Biaxial Strain

For (111) biaxial strain, we can still use the rotational invariant property of the cubic crystal. However, in this case, we should take the rotational transformation

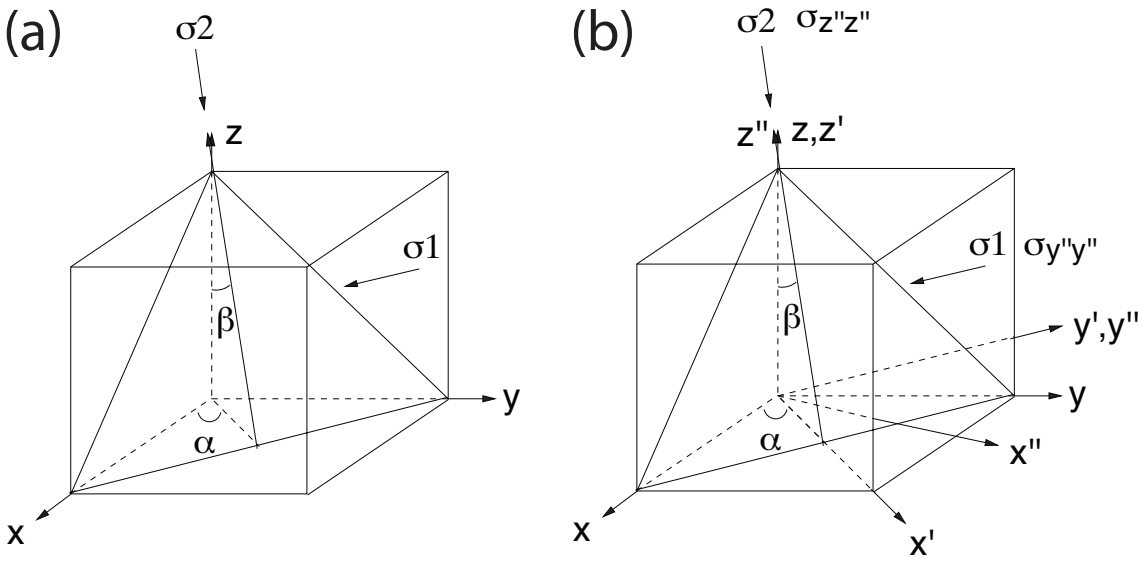

Figure 2.4. (a) Non-uniform (111) biaxial stress where the magnitude of stress are denoted as σ_1 and σ_1, respectively. (b) Rotational transformation of coordinate system of (111) biaxial stress. First rotation takes place with an angle α about z-axis and then rotated about y'-axis with an angle β, where $\cos\alpha = \frac{1}{\sqrt{2}}$, $\sin\alpha = \frac{1}{\sqrt{2}}$, $\cos\beta = \sqrt{\frac{2}{3}}$ and $\sin\beta = \sqrt{\frac{1}{3}}$.

twice about the z-axis of the original coordinate system and y'-axis in Fig. 2.3 of the first rotated coordinated system. We begin to define the rotational transformation matrix Q_1 and Q_2 for the first and second rotation, respectively, as follows,

$$Q_1 = \begin{bmatrix} \cos\alpha & \sin\alpha & 0 \\ -\sin\alpha & \cos\alpha & 0 \\ 0 & 0 & 1 \end{bmatrix} = \begin{bmatrix} \frac{1}{\sqrt{2}} & \frac{1}{\sqrt{2}} & 0 \\ -\frac{1}{\sqrt{2}} & \frac{1}{\sqrt{2}} & 0 \\ 0 & 0 & 1 \end{bmatrix} \tag{2.52}$$

and

$$Q_2 = \begin{bmatrix} \cos\beta & 0 & \sin\beta \\ 0 & 1 & 0 \\ -\sin\beta & 0 & \cos\beta \end{bmatrix} = \begin{bmatrix} \sqrt{\frac{2}{3}} & 0 & \sqrt{\frac{1}{3}} \\ 0 & 1 & 0 \\ -\sqrt{\frac{1}{3}} & 0 & \sqrt{\frac{2}{3}} \end{bmatrix} \tag{2.53}$$

Then, the stress tensor for the first rotated and second rotated coordinate system can be written as,

$$\sigma' = Q_1 \sigma Q_1^{-1}$$
$$\sigma'' = Q_2 \sigma' Q_2^{-1} \tag{2.54}$$

where σ' and σ'' are the stress tensor for first and second rotated coordinate system, respectively. Using the relation Eq. 2.54, the stress tensor in the original system for (111) biaxial stress is,

$$\sigma = Q_1^{-1} Q_2^{-1} \sigma'' Q_2 Q_1 \tag{2.55}$$

where,

$$\sigma'' = \begin{bmatrix} 0 & 0 & 0 \\ 0 & \sigma_1 & 0 \\ 0 & 0 & \sigma_2 \end{bmatrix} \tag{2.56}$$

Therefore,

$$\sigma = Q_1^{-1} Q_2^{-1} \begin{bmatrix} 0 & 0 & 0 \\ 0 & \sigma_1 & 0 \\ 0 & 0 & \sigma_2 \end{bmatrix} Q_2 Q_1 = \begin{bmatrix} \frac{\sigma_1}{2} + \frac{\sigma_2}{6} & -\frac{\sigma_1}{2} + \frac{\sigma_2}{6} & -\frac{\sigma_2}{3} \\ -\frac{\sigma_1}{2} + \frac{\sigma_2}{6} & \frac{\sigma_1}{2} + \frac{\sigma_2}{6} & -\frac{\sigma_2}{3} \\ -\frac{\sigma_2}{3} & -\frac{\sigma_2}{3} & \frac{2\sigma_2}{3} \end{bmatrix} \tag{2.57}$$

Now, the strain tensor under (111) non-uniform biaxial stress using Eq. 2.19 becomes,

$$\begin{bmatrix} e_{xx} \\ e_{yy} \\ e_{zz} \\ e_{yz} \\ e_{zx} \\ e_{xy} \end{bmatrix} = \begin{bmatrix} S_{11}(\frac{\sigma_1}{2} + \frac{\sigma_2}{6}) + S_{12}(\frac{\sigma_1}{2} + \frac{\sigma_2}{6}) + \frac{2S_{12}}{3}\sigma_2 \\ S_{11}(\frac{\sigma_1}{2} + \frac{\sigma_2}{6}) + S_{12}(\frac{\sigma_1}{2} + \frac{\sigma_2}{6}) + \frac{2S_{12}}{3}\sigma_2 \\ 2S_{12}(\frac{\sigma_1}{2} + \frac{\sigma_2}{6}) + \frac{2S_{11}}{3}\sigma_2 \\ -\frac{S_{44}}{6}\sigma_2 \\ -\frac{S_{44}}{6}\sigma_2 \\ \frac{1}{2}S_{44}(\frac{\sigma_2}{6} - \frac{\sigma_1}{2}) \end{bmatrix} \tag{2.58}$$

If we assume the biaxial strain is uniform, we can determine the relation between σ_1 and σ_2 using the uniform biaxial strain condition Eq. 2.32,

$$\sigma_2 = \sigma_1 \tag{2.59}$$

By substituting Eq. 2.59 into he right hand side of Eq. 2.58 we can show,

$$\begin{aligned} e_{xx} &= (\frac{2}{3}S_{11} + \frac{4}{3}S_{12})\sigma_1 = e_{yy} = e_{zz} \\ e_{xy} &= -\frac{S_{44}}{6}\sigma_1 = e_{yz} = e_{zx} \end{aligned} \tag{2.60}$$

Thus, we can show that the $\epsilon_\perp$ and $\epsilon_\parallel$ in terms of σ_1 using Eq. 2.33,

$$\begin{aligned} \epsilon_\perp &= e_{xx} + 2e_{xy} = (\frac{2}{3}S_{11} + \frac{4}{3}S_{12} - \frac{S_{44}}{3})\sigma_1 \\ \epsilon_{\parallel,(1)} &= e_{xx} - e_{xy} = (\frac{2}{3}S_{11} + \frac{4}{3}S_{12} + \frac{S_{44}}{6})\sigma_1 \end{aligned} \tag{2.61}$$

and the D_{111} for uniform biaxial strain of the (111) interface becomes,

$$\begin{aligned} D_{111}^{bi} = -\frac{\epsilon_\perp}{\epsilon_\parallel} &= -\frac{\frac{2}{3}S_{11} + \frac{4}{3}S_{12} - \frac{S_{44}}{3}}{\frac{2}{3}S_{11} + \frac{4}{3}S_{12} + \frac{S_{44}}{6}} \\ &= \frac{2(C_{11} + 2C_{12} - 2C_{44})}{C_{11} + 2C_{12} + 4C_{44}} \end{aligned} \tag{2.62}$$

The strain tensor for (111) biaxial strain in terms of the $\epsilon_\perp$ and $\epsilon_\parallel$ can be written,

$$\mathbf{e} = \begin{bmatrix} e_{xx} & e_{xy} & e_{zx} \\ e_{xy} & e_{yy} & e_{yz} \\ e_{zx} & e_{yz} & e_{zz} \end{bmatrix} = \begin{bmatrix} \frac{1}{3}\left(\epsilon_\perp + 2\epsilon_\parallel\right) & \frac{1}{3}\left(\epsilon_\perp - \epsilon_\parallel\right) & \frac{1}{3}\left(\epsilon_\perp - \epsilon_\parallel\right) \\ \frac{1}{3}\left(\epsilon_\perp - \epsilon_\parallel\right) & \frac{1}{3}\left(\epsilon_\perp + 2\epsilon_\parallel\right) & \frac{1}{3}\left(\epsilon_\perp - \epsilon_\parallel\right) \\ \frac{1}{3}\left(\epsilon_\perp - \epsilon_\parallel\right) & \frac{1}{3}\left(\epsilon_\perp - \epsilon_\parallel\right) & \frac{1}{3}\left(\epsilon_\perp + 2\epsilon_\parallel\right) \end{bmatrix} \tag{2.63}$$

2.3.2 Uniaxial Strain

Qualitatively, the uniaxial strain or stress is equivalent to biaxial strain or stress resulting in the same expression for the strain tensor in terms of $e_\parallel$ and $e_\perp$. However, the quantitative difference between uniaxial and biaxial strain stems from the 'Poisson's ratio' D. Derivation of the D for uniaxial strain is very similar to the case of biaxial strain except the stress tensor in which one has only one stress tensor component.

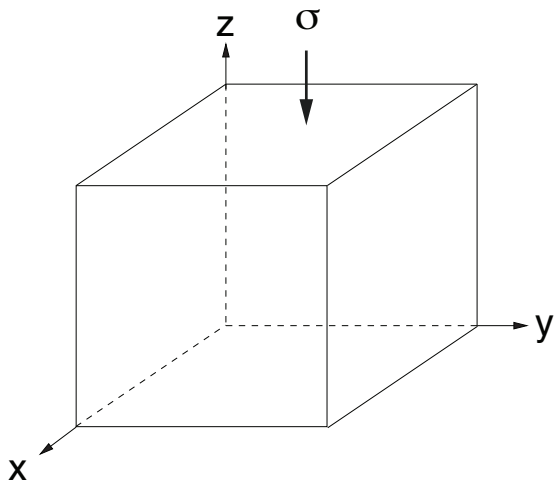

Figure 2.5. [001] uniaxial stress where the magnitude of stress tensor components σ_{zz} are denoted as σ.

2.3.2.1 [001] Uniaxial Strain

Assume that we have uniaxial stress along [001] direction which is equivalent to z-direction in Fig. 2.5, then the Eq. 2.19 can be written,

$$\begin{bmatrix} e_{xx} \\ e_{yy} \\ e_{zz} \\ e_{yz} \\ e_{zx} \\ e_{xy} \end{bmatrix} = \begin{bmatrix} S_{11} & S_{12} & S_{12} & 0 & 0 & 0 \\ S_{12} & S_{11} & S_{12} & 0 & 0 & 0 \\ S_{12} & S_{12} & S_{11} & 0 & 0 & 0 \\ 0 & 0 & 0 & \frac{S_{44}}{2} & 0 & 0 \\ 0 & 0 & 0 & 0 & \frac{S_{44}}{2} & 0 \\ 0 & 0 & 0 & 0 & 0 & \frac{S_{44}}{2} \end{bmatrix} \begin{bmatrix} 0 \\ 0 \\ \sigma \\ 0 \\ 0 \\ 0 \end{bmatrix} \tag{2.64}$$

and

$$e_{xx} = S_{12}\sigma, \qquad e_{yy} = S_{12}\sigma, \qquad e_{zz} = S_{11}\sigma \tag{2.65}$$

The $e_{\parallel}$ and $e_{\perp}$ to the (001) plane using Eq. 2.23 and Eq. 2.65 can be written,

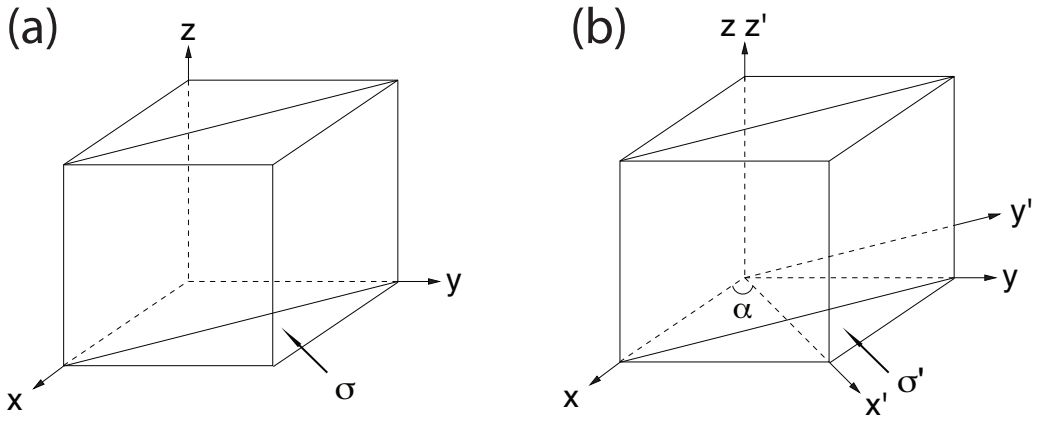

Figure 2.6. (a) [110] uniaxial stress where the magnitude of stress tensor components σ_{xy} are denoted as σ. (b) Rotational transformation of coordinate system of [110] uniaxial stress where the $\sigma_{x'x'} = \sigma'$.

$$\begin{aligned} \epsilon_{\perp} &= e_{zz} = S_{11}\sigma \\ \epsilon_{\parallel} &= e_{xx} = e_{yy} = S_{12}\sigma \end{aligned} \tag{2.66}$$

and the D_{001} for uniaxial strain would be,

$$D_{001}^{uni} = -\frac{\epsilon_{\perp}}{\epsilon_{\parallel}} = -\frac{S_{11}\sigma}{S_{12}\sigma} = \frac{C_{11}+C_{12}}{C_{12}} \tag{2.67}$$

2.3.2.2 [110] Uniaxial Strain

We take the same rotational transformation as shown in Sec. 2.3.1.2. Then the stress tensor σ' in the rotated coordinate system in Fig. 2.6 can be written as,

$$\sigma' = \begin{bmatrix} \sigma_{x'x'} & \sigma_{x'y'} & \sigma_{z'x'} \\ \sigma_{x'y'} & \sigma_{y'y'} & \sigma_{y'z'} \\ \sigma_{z'x'} & \sigma_{y'z'} & \sigma_{z'z'} \end{bmatrix} = \begin{bmatrix} \sigma & 0 & 0 \\ 0 & 0 & 0 \\ 0 & 0 & 0 \end{bmatrix} \tag{2.68}$$

and the stress tensor in the original coordinate system becomes,

$$\begin{aligned}\sigma &= Q^{-1}\sigma' Q \\ &= \begin{bmatrix} \frac{1}{\sqrt{2}} & \frac{-1}{\sqrt{2}} & 0 \\ \frac{1}{\sqrt{2}} & \frac{1}{\sqrt{2}} & 0 \\ 0 & 0 & 1 \end{bmatrix} \begin{bmatrix} \sigma & 0 & 0 \\ 0 & 0 & 0 \\ 0 & 0 & 0 \end{bmatrix} \begin{bmatrix} \frac{1}{\sqrt{2}} & \frac{1}{\sqrt{2}} & 0 \\ \frac{-1}{\sqrt{2}} & \frac{1}{\sqrt{2}} & 0 \\ 0 & 0 & 1 \end{bmatrix} = \begin{bmatrix} \frac{\sigma}{2} & \frac{\sigma}{2} & 0 \\ \frac{\sigma}{2} & \frac{\sigma}{2} & 0 \\ 0 & 0 & 0 \end{bmatrix}\end{aligned} \tag{2.69}$$

Using Eq. 2.19, the strain tensor under [110] uniaxial stress can be expressed as,

$$\begin{bmatrix} e_{xx} \\ e_{yy} \\ e_{zz} \\ e_{yz} \\ e_{zx} \\ e_{xy} \end{bmatrix} = \begin{bmatrix} S_{11} & S_{12} & S_{12} & 0 & 0 & 0 \\ S_{12} & S_{11} & S_{12} & 0 & 0 & 0 \\ S_{12} & S_{12} & S_{11} & 0 & 0 & 0 \\ 0 & 0 & 0 & \frac{S_{44}}{2} & 0 & 0 \\ 0 & 0 & 0 & 0 & \frac{S_{44}}{2} & 0 \\ 0 & 0 & 0 & 0 & 0 & \frac{S_{44}}{2} \end{bmatrix} \begin{bmatrix} \frac{\sigma}{2} \\ \frac{\sigma}{2} \\ 0 \\ 0 \\ 0 \\ \frac{\sigma}{2} \end{bmatrix} = \begin{bmatrix} \frac{S_{11}}{2}\sigma + \frac{S_{12}}{2}\sigma \\ \frac{S_{11}}{2}\sigma + \frac{S_{12}}{2}\sigma \\ S_{12}\sigma \\ 0 \\ 0 \\ \frac{S_{44}}{4}\sigma \end{bmatrix} \tag{2.70}$$

and

$$e_{xx} = e_{yy} = \frac{\sigma}{2}(S_{11} + S_{12}), \qquad e_{zz} = S_{12}\sigma, \qquad e_{xy} = \frac{S_{44}}{4}\sigma \tag{2.71}$$

The $e_{\parallel}$ and $e_{\perp}$ to the (110) plane using Eq. 2.49 and Eq. 2.71 can be written,

$$\begin{aligned}\epsilon_{\perp} &= e_{xx} + e_{xy} = \frac{\sigma}{4}(2S_{11} + 2S_{12} + S_{44}) \\ \epsilon_{\parallel} &= e_{xx} - e_{xy} = e_{zz} = S_{12}\sigma\end{aligned} \tag{2.72}$$

Therefore, the D_{110} for uniaxial strain becomes,

$$\begin{aligned}D_{110}^{uni} = -\frac{\epsilon_{\perp}}{\epsilon_{\parallel}} &= -\frac{2S_{11} + 2S_{12} + S_{44}}{4S_{12}} \\ &= \frac{2C_{11}C_{44} + (C_{11} + 2C_{12})(C_{11} - C_{12})}{4C_{12}C_{44}}\end{aligned} \tag{2.73}$$

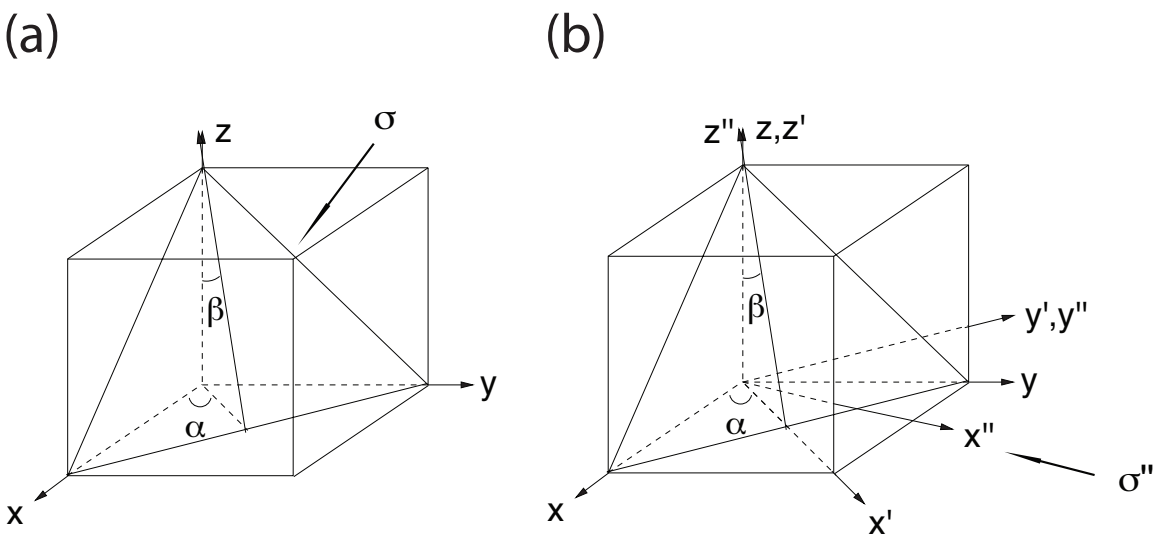

Figure 2.7. (a) [111] uniaxial stress where the magnitude of the stress is denoted as σ. (b) Rotational transformation of coordinate system of [111] uniaxial stress where the $\sigma_{x''x''} = \sigma''$. The rotation angles α and β are the same as in Fig. 2.4.

2.3.2.3 [111] Uniaxial Strain

We take the same rotational transformations as shown in Sec. 2.3.1.3 where the angles α and β are also same as in Fig. 2.4. Then the stress tensor σ'' in the doubly rotated coordinate system in Fig. 2.7 can be written as,

$$\sigma'' = \begin{bmatrix} \sigma_{x'x'} & \sigma_{x'y'} & \sigma_{z'x'} \\ \sigma_{x'y'} & \sigma_{y'y'} & \sigma_{y'z'} \\ \sigma_{z'x'} & \sigma_{y'z'} & \sigma_{z'z'} \end{bmatrix} = \begin{bmatrix} \sigma & 0 & 0 \\ 0 & 0 & 0 \\ 0 & 0 & 0 \end{bmatrix} \tag{2.74}$$

and the stress tensor σ in the original coordinate system becomes,

$$\sigma = Q_1^{-1} Q_2^{-1} \begin{bmatrix} \sigma & 0 & 0 \\ 0 & 0 & 0 \\ 0 & 0 & 0 \end{bmatrix} Q_2 Q_1 \tag{2.75}$$

where,

$$Q_1 = \begin{bmatrix} \frac{1}{\sqrt{2}} & \frac{1}{\sqrt{2}} & 0 \\ -\frac{1}{\sqrt{2}} & \frac{1}{\sqrt{2}} & 0 \\ 0 & 0 & 1 \end{bmatrix}, \qquad Q_2 = \begin{bmatrix} \sqrt{\frac{2}{3}} & \sqrt{\frac{1}{3}} & 0 \\ 0 & 1 & 0 \\ -\sqrt{\frac{1}{3}} & 0 & \sqrt{\frac{2}{3}} \end{bmatrix} \tag{2.76}$$

and we can simplify the σ as,

$$\sigma = \frac{\sigma}{3} \begin{bmatrix} 1 & 1 & 1 \\ 1 & 1 & 1 \\ 1 & 1 & 1 \end{bmatrix} \tag{2.77}$$

By substituting Eq. 2.77 into Eq. 2.19, we can show as follows,

$$\begin{aligned} e_{xx} = e_{yy} = e_{zz} &= \frac{\sigma}{3}(S_{11} + 2S_{12}) \\ e_{xy} = e_{yz} = e_{zx} &= \frac{\sigma}{6} S_{44} \end{aligned} \tag{2.78}$$

Therefore, the $e_{\parallel}$ and $e_{\perp}$ to the (111) plane from Eq. 2.33 and Eq. 2.78 can be written,

$$\begin{aligned} e_{\perp} &= e_{xx} + 2e_{xy} = \frac{\sigma}{6}(2S_{11} + 4S_{12} + S_{44}) \\ e_{\parallel} &= e_{xx} - e_{xy} = \frac{\sigma}{6}(2S_{11} + 4S_{12} - S_{44}) \end{aligned} \tag{2.79}$$

Thus, the D_{111} for uniaxial strain becomes,

$$\begin{aligned} D_{111}^{uni} = -\frac{\epsilon_{\perp}}{\epsilon_{\parallel}} &= -\frac{2S_{11} + 4S_{12} + S_{44}}{2S_{11} + 4S_{12} - S_{44}} \\ &= \frac{C_{11} + 2C_{12} + 2C_{44}}{C_{11} + 2C_{12} - 2C_{44}} \end{aligned} \tag{2.80}$$

CHAPTER 3

NONLOCAL EMPIRICAL PSEUDOPOTENTIAL THEORY

3.1 Theoretical Backgrounds and Concepts

Interacting atoms model which is one of the popular model of solids describe a collection of individual atoms to a model of a solid composed of cores containing periodically arranged nuclei with their core electrons and a sea of valence electrons interacting with the positive cores and each other [21, 22]. As a foundation to the pseudopotential theory, the frozen-core approximation assumes that the cores are taken to be unperturbed with respect to the formation of the solid. Thus, the cores in solids are treated as the same as the cores in isolated atoms and only the valence electrons readjust as the solid is formed.

Ideally, the total Hamiltonian for a crystal consists of kinetic energies of the electron and cores; the electron-electron, core-core, and electron-core Coulomb interactions; and relativistic effects. However, practically it is impossible to consider all the interactions in a given crystal so we need several simplifications and approximations to solve the problem. The adiabatic approximation (or Born-Oppenheimer approximation) which assumes that the electrons follows the core motion 'adiabatically', allows us to decouple the core and electron parts of the total Hamiltonian. Since our interest is limited to the electronic band structure $E(\vec{k})$ calculation, we can further simplify the problem by ignoring the core vibration and assuming fixed cores. Then the resulting Hamiltonian can be written as;

$$H = \sum_i \frac{\hat{p}_i^2}{2m} + \frac{1}{2}\sum_{i \neq j} \frac{e^2}{4\pi\epsilon_0 |\vec{r}_i - \vec{r}_j|} + \sum_{i,\alpha} V_\alpha(\vec{r}_i - \vec{R}_\alpha) \tag{3.1}$$

where the indices i and j refer to electrons while α refers to cores and $\vec{r}_i$ and $\vec{R}_\alpha$ represent the coordinates of electrons and cores, respectively. We have kinetic energy of the electrons, electron-electron Coulomb interactions, and the electron-core Coulomb interaction V_α. However, this many-body problem is still unsolvable so we need further simplification of the problem. The Hartree (mean field) approximations considers only one electron at the time and assumes that each electron moves in the average field created by all the other electrons. The total Hamiltonian then can be written as the sum of one-electron Hamiltonians:

$$H = \sum_i H_i \tag{3.2}$$

where the one-electron Hamiltonian is

$$H_i = \frac{\hat{p}_i^2}{2m} + \sum_j \frac{e^2}{4\pi\epsilon_0} \int \frac{\psi_j^*(\vec{r}_j)\psi_j(\vec{r}_j)}{|\vec{r}_i - \vec{r}_j|} d\vec{r}_j + \sum_\alpha V_\alpha(\vec{r}_i - \vec{R}_\alpha) \tag{3.3}$$

where integral term represents the electrostatic potential due to the charge density of the j-th electrons so that the sum constitutes the 'mean field' due to all other electrons. Then the electronic wavefunctions are product of one-electron wavefunctions and the Pauli principle should be obeyed. The Hartree approximation have significantly simplified the problem and we can rewrite the Eq.3.3 as,

$$H_i = \frac{\hat{p}_i^2}{2m} + V_{lat}(\vec{r}) \tag{3.4}$$

where the $V_{lat}(\vec{r})$ possesses the lattice symmetry and includes both the electron-electron and electron-core Coulomb interactions which are averaged and the each

electron moves in this average potential. Then we need to determine the $V_{lat}(\vec{r})$ and solve the Schrödinger's equation for $E_n(\vec{k})$ and $\psi_n(\vec{r})$ which can be greatly simplified by taking advantage of the translational symmetry of the crystal. Thus one can employ the Bloch's theorem, so expanding the general solution over products of Bloch functions and plan-waves, and arrive at a matrix form of the Hamiltonian.

In pseudopotential theory, the core electrons are assumed to be frozen in an atomic configuration while only the valence electrons which are responsible to the atomic bonding need to be considered and they move in a net, weak single-electron potential. Theoretical background of the pseudopotential theory can be started from the orthogonalized plane-wave (OPW) method in which the unknown single electron wavefunctions expanded over the subset of plane-waves are orthogonal to the core states known from atomic structure calculation. Then the mathematical formulation by Phillips-Kleinman cancellation theorem [67] can give a formal justification of the pseudopotential theory as following. We begin by assuming that we know the exact crystal wavefunction ψ as a sum of a smooth wavefunction ϕ and a sum over occupied core states ξ_t for an individual ion,

$$\psi = \phi + \sum_t c_t \xi_t \tag{3.5}$$

If we assume that the ψ is orthogonal to the core states as in the OPW scheme, that is $\langle \xi_t | \psi \rangle = 0$, then the plane-wave expansion coefficients c_t is,

$$c_t = -\langle \xi_t | \phi \rangle \tag{3.6}$$

and we obtain

$$\psi = \phi - \sum_t \langle \xi_t | \phi \rangle \xi_t \tag{3.7}$$

Now our aim is to look for a wave equation satisfied by ϕ, the 'smooth' part of the ψ. The Schrödinger's equation with Hamiltonian, $H = \hat{p}^2/2m + V_c$ operating on ψ

which gives the correct eigen-energy E. Then we substitute Eq. 3.7 into $H\psi = E\psi$ and we can obtain,

$$H\psi = H\phi - \sum_t E_t|\xi_t\rangle\langle\xi_t|\phi\rangle = E\psi \tag{3.8}$$

and then,

$$H\phi + \sum_t (E - E_t)\xi_t\langle\xi_t|\phi\rangle = E\phi \tag{3.9}$$

We can rewrite the Eq. 3.9 as,

$$(H + V_{nl})\phi = E\phi \tag{3.10}$$

where the nonlocal pseudopotential V_{nl} is,

$$V_{nl}\phi = \sum_t (E - E_t)\xi_t\langle\xi_t|\phi\rangle \tag{3.11}$$

which acts like a short-ranged non-Hermitian negative repulsive potential. If we rewrite the H of Eq. 3.10 with a kinetic and potential energy part, then we obtain,

$$\left[-\frac{\hbar^2}{2m}\nabla^2 + V_c + V_{nl}\right]\phi = \left[-\frac{\hbar^2}{2m}\nabla^2 + V_{pseudo}\right]\phi = E\phi \tag{3.12}$$

where the V_{pseudo} is the pseudopotential which is the sum of attractive long-ranged core potential and repulsive short-ranged nonlocal potential which effect almost compensated by the attractive core potential near the core leading to the net, weak effective potential acting on the valence electrons [10]. The Eq. 3.12 is called 'pseudopotential' equation and we can obtain the correct 'pseudo-wavefunction' ϕ outside cores. Also, we should note the the energy E is identical to the eigenvalue corresponding the the exact wavefunction ψ and the resulting 'pseudo-wavefunction' ϕ are smoothly varying in the core region in contrast to the exact wavefunction ψ because of the cancellations of the real potential in the core region by Eq. 3.11.

Now our task is to find the 'pseudopotential' (or 'model potential') $V_{pseudo}(\vec{r})$ which yield correct wavefunctions outside cores and its Fourier transform $V(\vec{G})$ in reciprocal space, hence $V(q)$ is the relevant potential, is required for band structure calculation. Empirical pseudopotential method (EPM) involves direct fit of $V(\vec{G})$'s to the experimental band structure which will be described in detail in the following sections.

3.2 Local Pseudopotential

In this section, we review the nonlocal empirical pseudopotential method to calculate the electronic band structure which have been widely used since it was introduced by Chelikowsky and Cohen [18, 17]. The total hamiltonian of the crystal can be written as a sum of local, nonlocal and spin-orbit hamiltonians.

$$H^{tot}_{\vec{G},\vec{G}'} = H^{L}_{\vec{G},\vec{G}'} + H^{NL}_{\vec{G},\vec{G}'} + H^{SP}_{\vec{G},\vec{G}'} \tag{3.13}$$

where the local hamiltonian $H^{L}_{\vec{G},\vec{G}'}$ to solve the single electron Schrödinger equation in crystal without external potential can be written as,

$$H^{L}_{\vec{G},\vec{G}'}\psi(\vec{r}) = -\frac{\hbar^2}{2m}\nabla^2\psi(\vec{r}) + V_{lat}(\vec{r})\psi(\vec{r}) = E_{\vec{k}}\psi(\vec{r}) \tag{3.14}$$

where the $V_{lat}(\vec{r})$ is the periodic lattice potential ignoring nonlocal effects and satisfies $V_{lat}(\vec{r}) = V_{lat}(\vec{r} + \vec{r'})$. Since $V_{lat}(\vec{r})$ is periodic, the wave function can be expressed with Bloch theorem,

$$\begin{aligned} \psi_{\vec{k}}(\vec{r}) \quad &= e^{i\vec{k}\cdot\vec{r}}\sum_{\vec{G}} u_{\vec{k},\vec{G}} e^{i\vec{G}\cdot\vec{r}} \\ &= \sum_{\vec{G}} u_{\vec{k},\vec{G}} e^{i(\vec{k}+\vec{G})\cdot\vec{r}} = \sum_{\vec{G}} u_{\vec{k}+\vec{G}} e^{i(\vec{k}+\vec{G})\cdot\vec{r}} \end{aligned} \tag{3.15}$$

where the $\vec{G}$ are the reciprocal lattice vectors. Substitute Eq. 3.15 into Eq. 3.14,

$$\begin{aligned} -\frac{\hbar^2}{2m}\nabla^2\psi_{\vec{k}}(\vec{r}) &= -\frac{\hbar^2}{2m}\nabla^2\left[\sum_{\vec{G}} u_{\vec{k}+\vec{G}} e^{i(\vec{k}+\vec{G})\cdot\vec{r}}\right] = -\frac{\hbar^2}{2m}\sum_{\vec{G}} u_{\vec{k}+\vec{G}}\left[\nabla^2 e^{i(\vec{k}+\vec{G})\cdot\vec{r}}\right] \\ &= \frac{\hbar^2}{2m}\sum_{\vec{G}} u_{\vec{k}+\vec{G}}\left[|\vec{k}+\vec{G}|^2 e^{i(\vec{k}+\vec{G})\cdot\vec{r}}\right] \end{aligned} \tag{3.16}$$

thus, the fourier transform of the local hamiltonian is,

$$\frac{\hbar^2}{2m}\sum_{\vec{G}} |\vec{k}+\vec{G}|^2 u_{\vec{k}+\vec{G}} e^{i(\vec{k}+\vec{G})\cdot\vec{r}} + V_{lat}(\vec{r})\sum_{\vec{G}} u_{\vec{k}+\vec{G}} e^{i(\vec{k}+\vec{G})\cdot\vec{r}} = E(\vec{k})\sum_{\vec{G}} u_{\vec{k}+\vec{G}} e^{i(\vec{k}+\vec{G})\cdot\vec{r}} \tag{3.17}$$

By multiplying $e^{-i(\vec{k}+\vec{G'})\cdot\vec{r}}$ on both side, then we have,

$$\frac{\hbar^2}{2m}\sum_{\vec{G}} |\vec{k}+\vec{G}|^2 u_{\vec{k}+\vec{G}} e^{i(\vec{G}-\vec{G'})\cdot\vec{r}} + V_{lat}(\vec{r})\sum_{\vec{G}} u_{\vec{k}+\vec{G}} e^{i(\vec{G}-\vec{G'})\cdot\vec{r}} = E(\vec{k})\sum_{\vec{G}} u_{\vec{k}+\vec{G}} e^{i(\vec{G}-\vec{G'})\cdot\vec{r}} \tag{3.18}$$

Taking the integration over the whole volume of the crystal, the first term of the left side of Eq. 3.18 becomes,

$$\begin{aligned} \frac{\hbar^2}{2m}\int_{-\infty}^{\infty} d^3\vec{r}\sum_{\vec{G}} |\vec{k}+\vec{G}|^2 u_{\vec{k}+\vec{G}} e^{i(\vec{G}-\vec{G'})\cdot\vec{r}} &= \frac{\hbar^2}{2m}\sum_{\vec{G}} |\vec{k}+\vec{G}|^2 u_{\vec{k}+\vec{G}}\int_{-\infty}^{\infty} d^3\vec{r} e^{i(\vec{G}-\vec{G'})\cdot\vec{r}} \\ &= (2\pi)^3\frac{\hbar^2}{2m}\sum_{\vec{G}} |\vec{k}+\vec{G}|^2 u_{\vec{k}+\vec{G}}\delta(\vec{G}-\vec{G'}) \\ &= (2\pi)^3\frac{\hbar^2}{2m}|\vec{k}+\vec{G'}|^2 u_{\vec{k}+\vec{G'}} \end{aligned} \tag{3.19}$$

the second term would be,

$$\begin{aligned} \int_{-\infty}^{\infty} d^3\vec{r} V_{lat}(\vec{r})\sum_{\vec{G}} u_{\vec{k}+\vec{G}} e^{i(\vec{G}-\vec{G'})\cdot\vec{r}} &= \sum_{\vec{G}} u_{\vec{k}+\vec{G}}\int_{-\infty}^{\infty} d^3\vec{r} V_{lat}(\vec{r}) e^{i(\vec{G}-\vec{G'})\cdot\vec{r}} \\ &= \sum_{\vec{G}} u_{\vec{k}+\vec{G}} V(\vec{G}-\vec{G'})(2\pi)^3 \end{aligned} \tag{3.20}$$

and the right side of Eq. 3.18 would be,

$$E(\vec{k})\sum_{\vec{G}} u_{\vec{k}+\vec{G}} \int_{-\infty}^{\infty} d^3\vec{r} e^{i(\vec{G}-\vec{G'})\cdot\vec{r}} \quad = E(\vec{k})\sum_{\vec{G}} u_{\vec{k}+\vec{G}}\delta(\vec{G}-\vec{G'})(2\pi)^3$$
$$= (2\pi)^3 E(\vec{k}) u_{\vec{k}+\vec{G'}} \tag{3.21}$$

Thus, we can simplify the Eq. 3.18 as,

$$\frac{\hbar^2}{2m}|\vec{k}+\vec{G'}|^2 u_{\vec{k}+\vec{G'}} + \sum_{\vec{G}} u_{\vec{k}+\vec{G}} V(\vec{G}-\vec{G'}) = E(\vec{k}) u_{\vec{k}+\vec{G'}} \tag{3.22}$$

then we multiply $\sum_{\vec{G}} \delta(\vec{G}-\vec{G'})$ to the first term of left and right side of Eq. 3.22,

$$\sum_{\vec{G}} \delta(\vec{G}-\vec{G'})\frac{\hbar^2}{2m}|\vec{k}+\vec{G'}|^2 u_{\vec{k}+\vec{G'}} + \sum_{\vec{G}} u_{\vec{k}+\vec{G}} V(\vec{G}-\vec{G'}) = \sum_{\vec{G}} \delta(\vec{G}-\vec{G'}) E(\vec{k}) u_{\vec{k}+\vec{G'}} \tag{3.23}$$

where $\sum_{\vec{G}} \delta(\vec{G}-\vec{G'}) = N$ and $\delta(\vec{G}-\vec{G'}) = 1$ if $\vec{G} = \vec{G'}$. This is the linear homogeneous equation and can be re-written as,

$$\sum_{\vec{G}} \left[\{ \frac{\hbar^2}{2m}|\vec{k}+\vec{G'}|^2 - E(\vec{k}) \} \delta(\vec{G}-\vec{G'}) + V(\vec{G}-\vec{G'}) \right] u_{\vec{k}+\vec{G}} = 0 \tag{3.24}$$

This linear homogeneous equation has nontrivial solutions only if the determinant of the equation is zero called secular equation.

$$Det| \{ \frac{\hbar^2}{2m}|\vec{k}+\vec{G'}|^2 - E(\vec{k}) \} \delta(\vec{G}-\vec{G'}) + V(\vec{G}-\vec{G'})| = 0 \tag{3.25}$$

The term $V(\vec{G}-\vec{G'})$ can be simplified using its periodicity,

$$V(\vec{G}-\vec{G'}) = \frac{1}{V}\int_V V_{lat}(\vec{r}) e^{-i(\vec{G}-\vec{G'})\cdot\vec{r}} d^3\vec{r} \tag{3.26}$$

assuming the wavefunctions are nomarlized to the volume V of the crystal. Now, $V_{lat}(\vec{r})$ is the sum of the ionic potentials in the wigner-seitz (WS) cell. Since we must

deal with indices for both cells and ions in each cell, we use the indices $l, m, ...$ for the cells and the indices $\alpha, \beta...$ for the N_{ions} in the cell. Then the lattice potential $V_{lat}(\vec{r})$ at position $\vec{r}$ is assumed to be self-consistent and to be represented as a linear superposition of ionic potential,

$$V_{lat}(\vec{r}) = \sum_{l,\alpha} V_{ion}(\vec{r} - \vec{R}_l - \vec{\tau}_\alpha) \tag{3.27}$$

where the V_{ion} is the ionic potential for the ion at $\vec{\tau}_\alpha$ in the cell at $\vec{R}_l$. Then Eq. 3.26 becomes,

$$V(\vec{G} - \vec{G'}) = \frac{1}{V} \int_V \sum_{l,\alpha} V_{ion}(\vec{r} - \vec{R}_l - \vec{\tau}_\alpha) e^{-i(\vec{G}-\vec{G'})\cdot\vec{r}} d^3\vec{r} \tag{3.28}$$

Let $\vec{r'} = \vec{r} - \vec{R}_l - \vec{\tau}_\alpha$ as dummy integration variable, then

$$\begin{aligned} V(\vec{G} - \vec{G'}) &= \frac{1}{V} \sum_{l,\alpha} \int_V V_{ion}(\vec{r'}) e^{-i(\vec{G}-\vec{G'})\cdot(\vec{r'}+\vec{R}_l+\vec{\tau}_\alpha)} d^3\vec{r'} \\ &= \frac{1}{V} \sum_{l,\alpha} e^{-i(\vec{G}-\vec{G'})\cdot\vec{R}_l} e^{-i(\vec{G}-\vec{G'})\cdot\vec{\tau}_\alpha} \int_V V_{ion}(\vec{r'}) e^{-i(\vec{G}-\vec{G'})\cdot\vec{r'}} d^3\vec{r'} \\ &= \frac{1}{V} \sum_{l} e^{-i(\vec{G}-\vec{G'})\cdot\vec{R}_l} \sum_{\alpha} e^{-i(\vec{G}-\vec{G'})\cdot\vec{\tau}_\alpha} \int_V V_{ion}(\vec{r'}) e^{-i(\vec{G}-\vec{G'})\cdot\vec{r'}} d^3\vec{r'} \end{aligned} \tag{3.29}$$

Since the ionic potential $V_{ion}(\vec{r'})$ is short-range which decays vert quickly at large distance and we can neglect the contribution to the integral coming from point at $\vec{r'}$ outside the WS cell.

$$\int_V V_{ion}(\vec{r'}) e^{-i(\vec{G}-\vec{G'})\cdot\vec{r'}} d^3\vec{r'} \simeq \int_\Omega V_{ion}(\vec{r'}) e^{-i(\vec{G}-\vec{G'})\cdot\vec{r'}} d^3\vec{r'} \tag{3.30}$$

where Ω is the volume of the WS cell. Since

$$\sum_l e^{-i(\vec{G}-\vec{G'})\cdot\vec{R}_l} = \sum_l 1 = N_{cell} \tag{3.31}$$

where N_{cell} is the number of cells in volume V and $e^{-i(\vec{G}-\vec{G'})\cdot\vec{R}_l} = e^{-i2n\pi} = 1$, we can show,

$$\begin{aligned} V(\vec{G}-\vec{G'}) &= \frac{N_{cell}}{V}\sum_{\alpha} e^{-i(\vec{G}-\vec{G'})\cdot\vec{\tau}_\alpha}\int_{\Omega} V_{ion}(\vec{r'})e^{-i(\vec{G}-\vec{G'})\cdot\vec{r'}}d^3\vec{r'} \\ &= \frac{N_{cell}}{V}\sum_{\alpha} e^{-i(\vec{G}-\vec{G'})\cdot\vec{\tau}_\alpha}\frac{\Omega}{\Omega}\int_{\Omega} V_{ion}(\vec{r'})e^{-i(\vec{G}-\vec{G'})\cdot\vec{r'}}d^3\vec{r'} \\ &= \frac{N_{cell}\Omega}{V}\sum_{\alpha} e^{-i(\vec{G}-\vec{G'})\cdot\vec{\tau}_\alpha}\frac{1}{\Omega}\int_{\Omega} V_{ion}(\vec{r'})e^{-i(\vec{G}-\vec{G'})\cdot\vec{r'}}d^3\vec{r'} \\ &\simeq S(\vec{G}-\vec{G'})V_{ion}(\vec{G}-\vec{G'}) \end{aligned} \tag{3.32}$$

where $V_{ion}(\vec{G}-\vec{G'})$ is called atomic form factor which is the Fourier transform of the atomic potential within the WS cell and $S(\vec{G}-\vec{G'})$ is called the structure factor which depends only on the location of the ions within the WS cell.

$$\begin{aligned} V_{ion}(\vec{G}-\vec{G'}) &= \frac{1}{\Omega}\int_{\Omega} V_{ion}(\vec{r'})e^{-i(\vec{G}-\vec{G'})\cdot\vec{r'}}d^3\vec{r'} \\ S(\vec{G}-\vec{G'}) &= \frac{1}{N}\sum_{\alpha} e^{-i(\vec{G}-\vec{G'})\cdot\vec{\tau}_\alpha} \end{aligned} \tag{3.33}$$

These equations can be specialized for the diamond or zinc-blende compounds which have two ions in the unit cell at $\vec{\tau}_1 = (0,0,0)$ and $\vec{\tau}_2 = a_0(1,1,1)/4$ where a_0 is the unstrained lattice constant in cartesian coordinate. With the two ions model, the atomic form factor can be simplified as,

$$V(\vec{G}-\vec{G'}) = V_{\vec{G}\vec{G'},1}e^{-i(\vec{G}-\vec{G'})\cdot\vec{\tau}_1} + V_{\vec{G}\vec{G'},2}e^{-i(\vec{G}-\vec{G'})\cdot\vec{\tau}_2} \tag{3.34}$$

For convenience, we shift the origin of the coordinate to the mid-point between the ions, so that $\vec{\tau}_1 = \vec{\tau} = a_0(1,1,1)/8$ and $\vec{\tau}_2 = -\vec{\tau} = -a_0(1,1,1)/8$. Then Eq. 3.34 becomes,

$$
\begin{aligned}
V(\vec{G}-\vec{G}') &= V_{\vec{G}\vec{G}',1}e^{-i(\vec{G}-\vec{G}')\cdot\vec{\tau}} + V_{\vec{G}\vec{G}',2}e^{i(\vec{G}-\vec{G}')\cdot\vec{\tau}} \\
&= V^s(\vec{G}-\vec{G}')cos\{(\vec{G}-\vec{G}')\cdot\vec{\tau}\} + iV^a(\vec{G}-\vec{G}')sin\{(\vec{G}-\vec{G}')\cdot\vec{\tau}\} \\
&= V^s(\vec{G}-\vec{G}')S^s(\vec{G}-\vec{G}') + iV^a(\vec{G}-\vec{G}')S^a(\vec{G}-\vec{G}') \qquad (3.35)
\end{aligned}
$$

where the structure factors are,

$$
\begin{aligned}
S^s(\vec{G}-\vec{G}') &= \cos\{(\vec{G}-\vec{G}')\cdot\vec{\tau}\} \\
S^a(\vec{G}-\vec{G}') &= \sin\{(\vec{G}-\vec{G}')\cdot\vec{\tau}\} \qquad (3.36)
\end{aligned}
$$

and the symmetric and asymmetric form factor $V^s_{|\vec{G}-\vec{G}'|}$ and $V^a_{|\vec{G}-\vec{G}'|}$, respectively, are,

$$
\begin{aligned}
V^s_{|\vec{G}-\vec{G}'|} &= \frac{1}{2}(V_{\vec{G}\vec{G}',1} + V_{\vec{G}\vec{G}',2}) \\
V^a_{|\vec{G}-\vec{G}'|} &= \frac{1}{2}(V_{\vec{G}\vec{G}',1} - V_{\vec{G}\vec{G}',2}) \qquad (3.37)
\end{aligned}
$$

with the atomic pseudopotential of two ions in the cell,

$$
V_{\vec{G}\vec{G}',i} = \frac{2}{\Omega}\int_{\Omega} V_i(\vec{r})e^{-i(\vec{G}-\vec{G}')\cdot\vec{r}}d\vec{r} \qquad (3.38)
$$

where i=1 and 2 which would be the anion and cation for zinc-blende crystals and identical for the diamond crystals such as Si and Ge resulting in the zero asymmetric form factor. In this local pseudopotential approximation without knowing the information in the core states, we can empirically fit both symmetric and asymmetric form factor to the experimental data in order to obtain correct band structure of valence electrons which plays a major role to the chemical or physical properties of the crystal. Typically, the ionic potential is assumed to be spherically symmetric so that the form factors depend upon the magnitude of $\vec{G}$ [17]. Then we only need three form factors at $|\vec{G}-\vec{G}'| = \sqrt{3}$, $\sqrt{8}$ and $\sqrt{11}\times(2\pi/a_0)$ as empirical parameters for bulk relaxed

cubic crystals such as Si and Ge since the full Fourier transform $V(|q| = |\vec{G} - \vec{G'}|)$ becomes very weak for q's larger than $\sqrt{11} \times (2\pi/a_0)$ due to the cancellation of the strong core potential.

Finally, the linear homogeneous equation Eq. 3.24 can be written in terms of the form and structure factor,

$$\sum_{\vec{G}} \left[\{ \frac{\hbar^2}{2m} |\vec{k} + \vec{G'}|^2 - E(\vec{k}) \} \delta_{\vec{G},\vec{G'}} + V^s_{\vec{G},\vec{G'}} S^s_{\vec{G},\vec{G'}} + iV^a_{\vec{G},\vec{G'}} S^a_{\vec{G},\vec{G'}} \right] u_{\vec{k}+\vec{G}} = 0 \qquad (3.39)$$

and thus the secular equation of Eq. 3.25 which is the eigenvalue problem would be,

$$Det \left| \{ \frac{\hbar^2}{2m} |\vec{k} + \vec{G'}|^2 - E(\vec{k}) \} \delta_{\vec{G},\vec{G'}} + V^s_{\vec{G},\vec{G'}} S^s_{\vec{G},\vec{G'}} + iV^a_{\vec{G},\vec{G'}} S^a_{\vec{G},\vec{G'}} \right| = 0 \qquad (3.40)$$

Numerically, we construct a two dimensional complex matrix with the reciprocal lattice vector $\vec{G}$ and $\vec{G'}$ which has a diagonal elements $\hbar^2|\vec{k} + \vec{G'}|^2/2m$ and we solve for the eigenvalues $E(\vec{K})$ which is the electron's energy band in k-space.

3.3 Nonlocal Pseudopotential

It had been impressive success that the local-only EPM was able to accurately reproduce the major optical gaps and cyclotron masses of semiconductors. However, deviation from the experimental results became significant in photoemission and X-ray charge-density results so that it was required to employ an energy-dependent nonlocal pseudopotential [17]. In general, the pseudopotential is spatially nonlocal and depends on $\vec{r}$ and $\vec{r'}$ and explicitly Eq. 3.11 can be written,

$$V_{nl}(\vec{r}, \vec{r'}) = \sum_t (E - E_t) |\xi_t(\vec{r})\rangle \langle \xi_t(\vec{r'})| \rangle \qquad (3.41)$$

where the empty 'ket' will contain a function of $\vec{r}$ [22]. The term 'nonlocal' usually means the angular momentum or l dependence of the pseudopotential. Since the V_{nl}

involves a sum over the t occupied core states, it can be linearly decomposed into angular momentum components by summing over various core states corresponding to their angular momentum symmetry [22]. Therefore, sums over $l = 0, 1, 2$ results in $s-$, $p-$ and $d-$components for the V_{nl} and we rewrite the V_{pseudo},

$$V_{pseudo} = V_s + V_p + V_d + .. \tag{3.42}$$

and if the core does not contain electrons of a certain angular momentum involved in the sum, there is no repulsive potential for that component [22]. In order to better understand the possible failing of the local-only EPM, Chelikowsky *et al.* [17, 18] employed an angular momentum and energy dependent nonlocal pseudopotential of the form,

$$V_{nl}(\vec{r}, E) = \sum_{l=0}^{\infty} A_l(E) f_l(r) P_l, \tag{3.43}$$

where $A_l(E)$ is an energy dependent well depth as an adjustable prameter, $f_l(r)$ is a function simulating the effect of core states with l symmetry, and P_l is a projection operator for the lth angular momentum component. Most commonly, square well or Gaussian model potential for $fl(r)$ are chosen and Chelikowsky *et al.* [18] employed the square well which has the advantage of simplicity and wide applicability as the form,

$$f_l(r) = \begin{cases} 1, & r < R_l \\ 0, & r \geqslant R_l \end{cases} \tag{3.44}$$

where the R_l is the model radius as a parameter.

Thus the required matrix elements of the nonlocal correction with a plane-wave basis are of the form

$$H^{NL}_{\vec{G},\vec{G'}} = V^{NL}_{\vec{K},\vec{K'}} = \frac{4\pi}{\Omega} \sum_{l,\alpha} A^{\alpha}_l (2l+1) P_l(cos\theta_{K,K'}) F^{\alpha}_l(K, K') S^{\alpha}(\vec{K} - \vec{K'}) \tag{3.45}$$

where $\vec{K} = \vec{k} + \vec{G}$, $\vec{K'} = \vec{k} + \vec{G'}$, and

$$F_l(\vec{K}, \vec{K'}) = \begin{cases} \frac{R^3}{2}\{[j_l(KR)]^2 - j_{l-1}(KR)j_{l+1}(KR)\} & K = K' \\ \frac{R^2}{(K^2-K'^2)}\left[Kj_{i+1}(KR)j_i(K'R) - K'j_{i+1}(K'R)j_i(KR)\right] & K \neq K' \end{cases} \tag{3.46}$$

The j_i are spherical Bessel functions,

$$\begin{aligned} j_{-1}(x) &= \frac{\cos x}{x} \\ j_0(x) &= \frac{\sin x}{x} \\ j_1(x) &= \frac{\sin x}{x^2} - \frac{\cos x}{x} \\ j_2(x) &= (\frac{3}{x^2} - 1)\frac{\sin x}{x} - \frac{3\cos x}{x^2} \\ j_3(x) &= (\frac{5}{x^2} - 2)\frac{3\sin x}{x^2} - (\frac{15}{x^2} - 1)\frac{\cos x}{x} \end{aligned} \tag{3.47}$$

$P_l(x)$ in Eq. 3.45 are the Legendre polynomials where the $\cos\theta_{K,K'} = (\vec{K} \cdot \vec{K'})/|KK'|$,

$$\begin{aligned} P_0(x) &= 1 \\ P_1(x) &= x \\ P_2(x) &= \frac{3}{2}x^2 - \frac{1}{2} \\ P_3(x) &= \frac{5}{2}x^3 - \frac{3}{2}x \end{aligned} \tag{3.48}$$

For diamond or zinc-blende semiconductors where we have two ions in the unit cell as we assumed in the previous section, we can expand the Eq. 3.45 as,

$$\begin{aligned} H^{NL}_{\vec{G},\vec{G'}} &= \frac{4\pi}{\Omega}\sum_{l=0,2,\alpha=1,2} A^\alpha_l(2l+1)P_l(cos\theta_{K,K'})F^\alpha_l(K,K')S^\alpha(\vec{K}-\vec{K'}) \\ &= \frac{4\pi}{\Omega}\sum_{l=0,2}\{A^1_l(2l+1)P_l(cos\theta_{K,K'})F^1_l(K,K')S^1(\vec{K}-\vec{K'}) \\ &+ A^2_l(2l+1)P_l(cos\theta_{K,K'})F^2_l(K,K')S^2(\vec{K}-\vec{K'})\} \end{aligned} \tag{3.49}$$

where the α is the sum over all the atoms in the unit cell and the l is the angular momentum index in which we consider s and d orbitals corresponding to $l = 0$ and $l = 2$, respectively. For s orbital ($l = 0$), the energy dependent well depth $A_0(E)$ is approximated,

$$A_0(E) = \alpha_0 + \beta_0\{\left[E^0(K)E^0(K')\right]^{\frac{1}{2}} - E^0(K_F)\} \tag{3.50}$$

where $E^0(K) = \hbar^2K^2/2m$ and K_F is the Fermi momentum as follows. The valence electron number density for group-IV diamond structure which has 4 valence electrons per atom and two atoms in an unit cell is,

$$n_v = \frac{N}{\Omega} = \frac{\text{number of total electrons in a cell}}{\text{atomic volume}} = 8 \times \frac{4}{a_0}$$

and the number of states per unit volume is

$$n_v = \frac{2}{(2\pi)^3}\int_{\text{Fermi Space}} d\vec{k} = \frac{2}{8\pi^3} \times \frac{4}{3}\pi K_F^3 = \frac{K_F^3}{3\pi^2}$$

thus,

$$K_F = (3\pi^2 n_v)^{\frac{1}{3}} = (3\pi^2 \times \frac{32}{a_0^3})^{\frac{1}{3}} = \frac{(96\pi^2)^{\frac{1}{3}}}{a_0}$$

Now, let's define,

$$\begin{aligned} V_{nl,1}(K,K') &= A_l^1(2l+1)P_l(cos\theta_{K,K'})F_l^1(K,K') \\ V_{nl,2}(K,K') &= A_l^2(2l+1)P_l(cos\theta_{K,K'})F_l^2(K,K') \end{aligned} \tag{3.51}$$

then Eq. 3.49 using Eq. 3.33 would be,

$$
\begin{aligned}
H^{NL}_{\vec{G},\vec{G}'} &= \frac{4\pi}{\Omega}\sum_{l=0,2}\{V_{nl,1}(K,K')\frac{1}{2}e^{-i(\vec{K}-\vec{K}')\cdot\vec{\tau}} + V_{nl,2}(K,K')\frac{1}{2}e^{i(\vec{K}-\vec{K}')\cdot\vec{\tau}}\} \\
&= \frac{4\pi}{\Omega}\sum_{l=0,2}\{\frac{1}{2}V_{nl,1}(K,K')\left[\cos(\vec{K}-\vec{K}')\cdot\vec{\tau} - i\sin(\vec{K}-\vec{K}')\cdot\vec{\tau}\right] \\
&+\frac{1}{2}V_{nl,2}(K,K')\left[\cos(\vec{K}-\vec{K}')\cdot\vec{\tau} + i\sin(\vec{K}-\vec{K}')\cdot\vec{\tau}\right]\} \\
&= \frac{4\pi}{\Omega}\sum_{l=0,2}\{V^s_{nl}(K,K')\cos(\vec{K}-\vec{K}')\cdot\vec{\tau} + iV^a_{nl}(K,K')\sin(\vec{K}-\vec{K}')\cdot\vec{\tau}\}
\end{aligned}
\tag{3.52}
$$

where,

$$
\begin{aligned}
V^s_{nl}(K,K') &= \frac{1}{2}\left[V_{nl,1}(K,K') + V_{nl,2}(K,K')\right] \\
V^a_{nl}(K,K') &= \frac{1}{2}\left[V_{nl,1}(K,K') - V_{nl,2}(K,K')\right]
\end{aligned}
$$

3.4 Spin-orbit Interaction

It has been well know that spin-orbit interactions can have significant importance on the electronic band structure of semiconductors, especially on the valence band structure near the valence band maximum. When an observer moves with velocity $\vec{v}$ across the lines of electrostatic field $\vec{e}$ generated by the charge of nucleus with core states, special relativity reveals that in the frame of the observer, a magnetic field

$$
\vec{B} = -\gamma\vec{\beta}\times\vec{\varepsilon} \tag{3.53}
$$

where, $\vec{\beta} = \vec{v}/c$ and $\gamma^2 = 1-\beta^2$. Thus, the magnetic field can expressed in another way,

$$
\vec{B} = -\frac{\vec{v}}{c}\times\vec{\varepsilon} = -\frac{\vec{P}}{mc}\times\vec{\varepsilon} \tag{3.54}
$$

This is the nature of the magnetic field with which the magnetic moment of the orbiting valence electron interacts [53]. In other words, the spin-orbit interaction is

the interaction between the spin-induced magnetic moment and the magnetic field seen by the electron. Analytically, the spin-orbit Hamiltonian is given as [76, 92],

$$H^{SP} = \frac{\hbar}{4mc^2}(\nabla V \times \hat{p} \cdot \hat{\sigma}) \tag{3.55}$$

where V is the lattice potential, $\hat{p}$ is the momentum operator, and $\hat{\sigma}$ is the Pauli spin operator. Chelikowsky *et al.* [18] have included spin-orbit interactions by extension of a method first presented by Saravia and Brust [76] for Ge and have followed the work of Weisz [92], as modified by Bloom and Bergstresser [11].

In this study, we have followed the approach by Chelikowsky *et al.* shown in Ref. [18] where they included the spin-orbit matrix element contribution which has a form of 2×2 matrix to the pseudopotential Hamiltonian as

$$H^{SP}_{\vec{G},\vec{G}'}(\vec{k}) = (\vec{K} \times \vec{K}') \cdot \vec{\sigma}_{s,s'} \left[-i\lambda^s \cos\{(\vec{G} - \vec{G}') \cdot \vec{\tau}\} + \lambda^a \sin\{(\vec{G} - \vec{G}') \cdot \vec{\tau}\} \right] \tag{3.56}$$

where

$$\begin{aligned} \lambda^s &= \frac{1}{2}(\lambda_A + \lambda_B) \\ \lambda^a &= \frac{1}{2}(\lambda_A - \lambda_B) \\ \lambda_A &= \mu B^A_{nl}(K) B^A_{nl}(K') \\ \lambda_B &= \alpha\mu B^B_{nl}(K) B^B_{nl}(K') \end{aligned} \tag{3.57}$$

and the σ are the Pauli spin states,

$$\vec{\sigma} = \begin{pmatrix} 0 & 1 \\ 1 & 0 \end{pmatrix} \hat{\sigma}_x + \begin{pmatrix} 0 & -i \\ i & 0 \end{pmatrix} \hat{\sigma}_y + \begin{pmatrix} 1 & 0 \\ 0 & -1 \end{pmatrix} \hat{\sigma}_z$$

The vector product $(\vec{K} \times \vec{K'}) \cdot \vec{\sigma}_{s,s'}$ can be simplified as,

$$(\vec{K} \times \vec{K'}) \cdot \vec{\sigma}_{s,s'} = \begin{pmatrix} K_1K_2' - K_2K_1' & (K_2K_3' - K_3K_2') + i(K_1K_3' - K_3K_1') \\ (K_2K_3' - K_3K_2') + i(K_3K_1' - K_1K_3') & K_2K_1' - K_1K_2' \end{pmatrix} \tag{3.58}$$

The λ^s and λ^a are the symmetric and antisymmetric contributions to the spin-orbit hamiltonian, μ is an empirical parameter and α is the ratio of the nonmetallic contribution to the metallic contribution for $\vec{G} = \vec{G'} = 0$ [88]. The B_{nl} are defined by

$$B_{nl}(K) = C \int_0^\infty j_l(Kr) R_{nl}(r) r^2 dr \tag{3.59}$$

where C is the nomalization constat determined by the condition

$$\sum_{K \to 0} K^{-1} B_{nl}(K) = 1 \tag{3.60}$$

thus, the constant C becomes

$$C = \frac{3}{\int_0^\infty r R_{nl}(r) r^2 dr} \tag{3.61}$$

The R_{nl} is the radial part of core wave function which are tabulated Hartree-Fock-Slater orbitals [40]. Here we only include contributions from the outermost p-core states corresponding to $l = 1$.

CHAPTER 4

BAND STRUCTURES FOR BULK SEMICONDUCTORS

4.1 Crystal Structure With Biaxial Strain

We use the diamond structure which can be expressed in terms of a set of primitive translation vectors $\vec{a}_1$, $\vec{a}_2$ and $\vec{a}_3$ and in general the choice of these primitive vectors is not unique [46, 98]. We take the primitive vectors for the bulk material without strain as,

$$\vec{a}_1 = \frac{1}{2}a_0(\hat{y}+\hat{z}), \qquad \vec{a}_2 = \frac{1}{2}a_0(\hat{x}+\hat{z}), \qquad \vec{a}_3 = \frac{1}{2}a_0(\hat{x}+\hat{y}) \tag{4.1}$$

where a_0 is a lattice constant of the unstrained material. The volume of the primitive cell becomes

$$\Omega = |\vec{a}_1 \cdot \vec{a}_2 \times \vec{a}_3| = \frac{1}{4}a_0^3 \tag{4.2}$$

and primitive translation vectors of the lattice reciprocal to the bulk fcc can be expressed as,

$$\vec{b}_1 = \frac{2\pi}{a_0}(-\hat{x}+\hat{y}+\hat{z}), \qquad \vec{b}_2 = \frac{2\pi}{a_0}(\hat{x}-\hat{y}+\hat{z}), \qquad \vec{b}_3 = \frac{2\pi}{a_0}(\hat{x}+\hat{y}-\hat{z}) \tag{4.3}$$

Thus, the reciprocal lattice vector would be a set of,

$$\vec{G} = l_1\vec{b}_1 + l_3\vec{b}_3 + l_3\vec{b}_3 \quad (l_1, l_2, l_3 = 0, 1, 2...) \tag{4.4}$$

Let's consider the fcc structure is biaxially strained on (001) interface, for example. Then we can take the primitive lattice vectors as,

$$\vec{a}_1 = a_0(1+\epsilon_\parallel)\hat{x}, \qquad \vec{a}_2 = a_0(1+\epsilon_\parallel)\hat{y}, \qquad \vec{a}_3 = a_0(1+\epsilon_\perp)\hat{z} \tag{4.5}$$

where $\epsilon_\parallel$ and $\epsilon_\perp$ are the strain components parallel and perpendicular to the interface, respectively, as discussed in the previous chapter, and the linear relation between $\epsilon_\parallel$ and $\epsilon_\perp$ using Eq. 2.20 and Eq. 2.39 is,

$$\epsilon_\perp = -D_{001}^{bi}\epsilon_\parallel, \qquad D_{001}^{bi} = 2C_{12}/C_{11} \tag{4.6}$$

The volume of the strained primitive cell would be,

$$\Omega = |\vec{a}_1 \cdot \vec{a}_2 \times \vec{a}_3| = \frac{a_0^3}{4}(1+\epsilon_\parallel)^2(1+\epsilon_\perp) \tag{4.7}$$

and thus the primitive translation vectors of the reciprocal lattice can be written,

$$\begin{aligned}
\vec{b}_1 &= \frac{2\pi}{\Omega}(\vec{a}_2 \times \vec{a}_3) = \frac{2\pi}{a_0}\left[-\frac{1}{1+\epsilon_\parallel}\hat{x} + \frac{1}{1+\epsilon_\parallel}\hat{y} + \frac{1}{1+\epsilon_\perp}\hat{z}\right] \\
\vec{b}_2 &= \frac{2\pi}{\Omega}(\vec{a}_3 \times \vec{a}_1) = \frac{2\pi}{a_0}\left[\frac{1}{1+\epsilon_\parallel}\hat{x} - \frac{1}{1+\epsilon_\parallel}\hat{y} + \frac{1}{1+\epsilon_\perp}\hat{z}\right] \\
\vec{b}_3 &= \frac{2\pi}{\Omega}(\vec{a}_1 \times \vec{a}_2) = \frac{2\pi}{a_0}\left[\frac{1}{1+\epsilon_\parallel}\hat{x} + \frac{1}{1+\epsilon_\parallel}\hat{y} - \frac{1}{1+\epsilon_\perp}\hat{z}\right]
\end{aligned} \tag{4.8}$$

In the case of [001] uniaxial strain, we can take the same primitive lattice vectors as Eq. 4.5 leading to the same reciprocal lattice vectors as Eq. 4.8. However, we should take the D_{001}^{uni} in Eq. 4.6 from Eq. 2.67 instead of using D_{001}^{bi} since there is quantitative

difference between uniaxial and biaxial strain as we mentioned previously. Similarly, we can take the primitive vectors for the strain of (110) interface as,

$$\begin{aligned}
\vec{a}_1 &= \frac{a_0}{2}\left[-\left(\frac{\epsilon_\parallel - \epsilon_\perp}{2}\right)\hat{x} + \left(1 + \frac{\epsilon_\parallel + \epsilon_\perp}{2}\right)\hat{y} + \left(1+\epsilon_\parallel\right)\hat{z}\right] \\
\vec{a}_2 &= \frac{a_0}{2}\left[\left(1 + \frac{\epsilon_\parallel + \epsilon_\perp}{2}\right)\hat{x} - \left(\frac{\epsilon_\parallel - \epsilon_\perp}{2}\right)\hat{y} + \left(1+\epsilon_\parallel\right)\hat{z}\right] \\
\vec{a}_3 &= \frac{a_0}{2}\left(1+\epsilon_\perp\right)\left(\hat{x}+\hat{y}\right)
\end{aligned} \tag{4.9}$$

and for the strain of (111) interface,

$$\begin{aligned}
\vec{a}_1 &= \frac{a_0}{2}\left[\frac{2}{3}\left(\epsilon_\perp - \epsilon_\parallel\right)\hat{x} + \left\{1 + \frac{1}{3}\left(2\epsilon_\perp + \epsilon_\parallel\right)\right\}\hat{y} + \left\{1 + \frac{1}{3}\left(2\epsilon_\perp + \epsilon_\parallel\right)\right\}\hat{z}\right] \\
\vec{a}_2 &= \frac{a_0}{2}\left[\left\{1 + \frac{1}{3}\left(2\epsilon_\perp + \epsilon_\parallel\right)\right\}\hat{x} + \frac{2}{3}\left(\epsilon_\perp - \epsilon_\parallel\right)\hat{y} + \left\{1 + \frac{1}{3}\left(2\epsilon_\perp + \epsilon_\parallel\right)\right\}\hat{z}\right] \\
\vec{a}_3 &= \frac{a_0}{2}\left[\left\{1 + \frac{1}{3}\left(2\epsilon_\perp + \epsilon_\parallel\right)\right\}\hat{x} + \left\{1 + \frac{1}{3}\left(2\epsilon_\perp + \epsilon_\parallel\right)\right\}\hat{y} + \frac{2}{3}\left(\epsilon_\perp - \epsilon_\parallel\right)\hat{z}\right]
\end{aligned} \tag{4.10}$$

Thus, the reciprocal lattice vectors for the strain of (110) and (111) plane becomes,

$$\begin{aligned}
\vec{b}_1 &= \frac{2\pi}{a_0}\frac{1}{1+\epsilon_\parallel}\left(-\hat{x}+\hat{y}+\hat{z}\right) \\
\vec{b}_2 &= \frac{2\pi}{a_0}\frac{1}{1+\epsilon_\parallel}\left(\hat{x}-\hat{y}+\hat{z}\right) \\
\vec{b}_3 &= \frac{2\pi}{a_0}\left(\frac{1}{1+\epsilon_\perp}\hat{x} + \frac{1}{1+\epsilon_\perp}\hat{y} - \frac{1}{1+\epsilon_\parallel}\hat{z}\right)
\end{aligned} \tag{4.11}$$

and

$$\begin{aligned}
\vec{b}_1 &= \frac{2\pi}{a_0}\frac{1}{3}\left[-\left(\frac{4}{1+\epsilon_\parallel} - \frac{1}{1+\epsilon_\perp}\right)\hat{x} + \left(\frac{1}{1+\epsilon_\perp} + \frac{2}{1+\epsilon_\parallel}\right)\hat{y} + \left(\frac{1}{1+\epsilon_\perp} + \frac{2}{1+\epsilon_\parallel}\right)\hat{z}\right] \\
\vec{b}_2 &= \frac{2\pi}{a_0}\frac{1}{3}\left[\left(\frac{1}{1+\epsilon_\perp} + \frac{2}{1+\epsilon_\parallel}\right)\hat{x} - \left(\frac{4}{1+\epsilon_\parallel} - \frac{1}{1+\epsilon_\perp}\right)\hat{y} + \left(\frac{1}{1+\epsilon_\perp} + \frac{2}{1+\epsilon_\parallel}\right)\hat{z}\right] \\
\vec{b}_3 &= \frac{2\pi}{a_0}\frac{1}{3}\left[\left(\frac{1}{1+\epsilon_\perp} + \frac{2}{1+\epsilon_\parallel}\right)\hat{x} + \left(\frac{1}{1+\epsilon_\perp} + \frac{2}{1+\epsilon_\parallel}\right)\hat{y} - \left(\frac{4}{1+\epsilon_\parallel} - \frac{1}{1+\epsilon_\perp}\right)\hat{z}\right]
\end{aligned} \tag{4.12}$$

, respectively.

In addition to the distortion of the crystal structure due to the strain, we should consider an additional displacement of the each atom in the unit cell. The new positions of the atom in the unit cell are given by following [56],

$$\begin{aligned}
\vec{\tau}_{(001)} &= \left[\mathbf{1} + \mathbf{e}_{(001)}\right] \vec{\tau} \\
\vec{\tau}_{(110)} &= \left[\mathbf{1} + \mathbf{e}_{(110)}\right] \vec{\tau} - \frac{a_0}{2} e_{xy,(110)} \zeta \begin{bmatrix} 1 \\ 1 \\ 0 \end{bmatrix} \\
\vec{\tau}_{(111)} &= \left[\mathbf{1} + \mathbf{e}_{(111)}\right] \vec{\tau} - \frac{a_0}{2} e_{xy,(111)} \zeta \begin{bmatrix} 0 \\ 0 \\ 1 \end{bmatrix}
\end{aligned} \tag{4.13}$$

where $\mathbf{1}$ is the unit tensor, ζ is the internal displacement parameter obtained by theoretical calculation [61].

4.2 Local Pseudopotential Interpolation

As we discussed in Chap. 3, we just need few local form factors to obtain comparable data to experiment for bulk semiconductors. All the necessary parameters including local form factors for nonlocal EPM calculation with spin-orbit interaction are shown in Tables 4.1, 4.2 and 4.3. However, the local form factors only at discrete values for the magnitude of the unstrained reciprocal lattice vector, $q = |\vec{G} - \vec{G}'| = \sqrt{3}$, $\sqrt{4}$, $\sqrt{8}$, and $\sqrt{11}$ (in units of $2\pi/a_0$) is insufficient when the strain is applied. Therefore we must employ an interpolation to obtain the value $V(q)$ of the form factor at arbitrary values of q. Several different interpolation schemes have been proposed in order to fit to the experimental data such as band structure, effective masses, and deformation potentials [94, 31, 73, 30, 59, 35, 4]. Rieger *et. al.* employed a cubic spline interpolation of the form factors, assuming also $V(q = 0) = -2E_F/3$ and

Table 4.1. Material parameters used in this work.

Quantity	Symbol	Unit	Si	Ge	GaAs	GaSb	InAs	InSb	InP
lattice constant[a]	a_0	Å	5.431	5.658	5.653	6.096	6.058	6.479	5.869
elastic constants[a]	C_{11}	10^{11} dyn cm^{-2}	16.577	12.853	11.26	8.834	8.329	6.918	10.11
	C_{12}	10^{11} dyn cm^{-2}	6.393	4.862	5.71	4.023	4.526	3.788	5.61
	C_{44}	10^{11} dyn cm^{-2}	7.962	6.680	6.00	4.322	3.959	3.132	4.56
cutoff energy	E_{cut}	Ry	10	10	10	10	10	10	10
internal displacement[b, c]	ζ	-	0.45	0.51	0.48	0.99	0.58	0.9	0.87

[a] From Ref. [58]
[b] From Ref. [13]
[c] From Ref. [61]

Table 4.2. EPM nonlocal and spin-orbit parameters. The superscrip *cat* and *ani* stand for cation and anion in III-V.

Quantity	Symbol	Unit	Si[a]	Ge[a]	GaAs [b]	GaSb[a]	InAs[a]	InSb[a]	InP[b]
s-well depth	α_0^{cat}	Ry	0.55	0.0	0.0	0.0	0.0	0.0	0.0
	α_0^{ani}				0.0	0.0	0.0	0.0	0.3
s-well energy dependence	β_0^{cat}	-	0.32	0.0	0.0	0.2	0.35	0.45	0.25
	β_0^{ani}				0.1	0.3	0.25	0.48	0.05
d-well depth	A_2^{cat}	Ry	0.0	0.295	0.25	0.2	0.5	0.55	0.55
	A_2^{ani}				0.65	0.6	1.0	0.7	0.35
s-well radius[b]	R_0^{cat}	Å	1.06	0.0	1.27	1.27	1.27	1.27	1.27
	R_0^{ani}				1.06	1.06	1.06	1.06	1.06
d-well radius[c]	R_2^{cat}	Å	0.0	1.22	1.33	1.4384	1.43	1.5289	1.38
	R_2^{ani}				1.11	1.2011	1.19	1.2767	1.15
spin-orbit	α	-	1.0	1.0	1.37978	2.2327	0.79204	1.278	0.1558
	μ	-	0.000214	0.002383	0.00127	0.003103	0.00261	0.0046	0.00241

[a] From Ref. [18]
[b] From Ref. [29]
[c] The d-well radius is fixed by 'touching spheres', as suggested in Ref.[68]

Table 4.3. Empirical local pseudopotential parameters. The form factors for Si, Ge and III-Vs are adjusted to fit experimental band gaps.

Quantity	Symbol	Unit	Compound						
			Si	Ge	GaAs	GaSb	InAs	InSb	InP
local form factor	$V^s_{\sqrt{3}}$	Ry	-0.263	-0.236	-0.235	-0.2043	-0.207	-0.199	-0.232
	$V^s_{\sqrt{8}}$	Ry	-0.040	0.019	0.015	0.0	0.0	-0.0115	0.0
	$V^s_{\sqrt{11}}$	Ry	0.033	0.056	0.0691(0.0538)	0.0497	0.0449	0.0432	0.0455
	$V^a_{\sqrt{3}}$	Ry	-	-	0.076	0.033	0.054	0.0416	0.078
	$V^a_{\sqrt{4}}$	Ry	-	-	0.057	0.028	0.0466	0.035	0.062
	$V^a_{\sqrt{11}}$	Ry	-	-	0.0061(0.0047)	0.0054	0.007	0.006	0.0116
cubic spline interpolation parameters	$S^s_{\sqrt{3}}$	-	0.4	0.4	0.45	0.74	0.55	0.68	0.765
	$S^s_{\sqrt{8}}$	-	0.1	0.09	0.125	0.14	0.125	0.09	0.09
	$S^s_{\sqrt{11}}$	-	0.1	0.09	0.025	0.01	0.025	0.01	0.025
	$S^a_{\sqrt{3}}$	-	-	-	0.025	-0.05	-0.035	-0.05	-0.05
	$S^a_{\sqrt{4}}$	-	-	-	-0.115	-0.04	-0.09	-0.04	-0.03
	$S^a_{\sqrt{11}}$	-	-	-	-0.01	-0.03	-0.022	-0.03	-0.06
	a_5	a.u.	5.0	4.5	4.05	4.0	4.5	3.9	4.2
	a_6	a.u.	0.3	0.3	0.39	0.3	0.41	0.3	0.3
	$V^s(0)$	Ry	-1.113	-1.100	-1.136	-1.080	-1.121	-1.077	-1.147
	$V^a(0)$	Ry	-	-	-0.104	-0.047	-0.088	-0.045	-0.114

$V(q = 3k_F) = 0$, where E_F and k_F are the free electrons Fermi energy and wave vector [73]. Fischetti *et. al.* [30] and Friedel *et. al.* [31] have used an expression of the form in which 'tanh'-term is introduced in order to cutoff the pseudopotential at short wave lengths ($q \to \infty$).

The long wave length behavior of the local pseudopotential $V(q = 0)$, which determines the acoustic deformation potentials and to the vacuum workfunction, has been discussed in several studies [30, 7, 4, 3, 35]. Allen *et. al.* extrapolated it to $V(q = 0) = -2E_F/3$, which is the values of the 'Heine-Abarenkov-Animalu model potential' at the Fermi surface [39] and mentioned that the choice for $V(q = 0)$ in not unique except in a nearly-free-electron metal [3, 4]. In contrast, Bednarek *et. al.* showed better agreement with experiment data regarding the Si absorption coefficient using $V(q = 0) = 0$, in sharp contrast with the suggestions of Refs. [35, 3]. In our context, even large, but still realistic, strain cannot probe the small-q behavior discussed above. Thus, our results are largely insensitive to this issue. Yet, in general empirical pseudopotentials may be used also in supercell calculations dealing, for example, with the band structure of thin homo- and hetero-layers, quantum wires, and quantum dots. In this case which one needs also the explicit form of $V(q)$ at small q and this value must yield the correct workfunction and band offset [59]. In previous studies [59, 97, 89, 99] of group IV and III-V semiconductors, Zunger's group has employed a single Gaussian or a linear combination of four Gaussians to express the $V(q)$ with parameters chosen so as to obtain the experimentally observed bulk band structure, effective masses, and workfunctions.

Therefore, in order to give our empirical pseudopotentials a more general range of applications, we have decided to treat the small-q behavior in order to obtain the correct workfunction and band alignment. The parameters $V(q = 0)$ we have employed are listed in Table 4.3 and have been obtained from Ref. [8] for GaAs and from fits to the known valence band offsets referenced to the GaAs [87, 83]. In

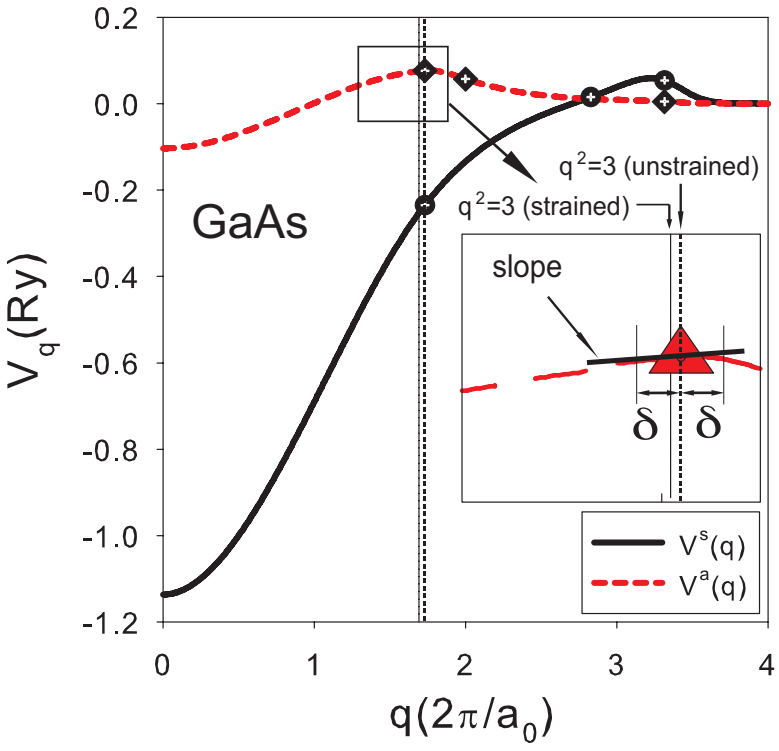

Figure 4.1. Symmetric (solid line) and antisymmetric (dashed line) local pseudopotential for GaAs obtained from a cubic spline interpolation with a fast cut-off at large q where symbols represent local form factors at $q = \sqrt{3}, \sqrt{8}(\sqrt{4})$ and $\sqrt{11}$ (in units of $2\pi/a_0$) shown in Table 4.3. The $V^{s,a}(q = 0)$ is referenced to Ref. [8] which are fitted to experimental workfunction.

addition, we employ a cubic spline interpolation which allows us to freely adjust slopes of the curve at a given q by using a q-dependent local pseudopotential exprssed as:

$$V(q) = V(q)_{cubic} \times \left[\frac{1}{2}\tanh\left\{\frac{a_5 - q^2}{a_6}\right\} + \frac{1}{2}\right], \tag{4.14}$$

where $V(q)_{cubic}$ is the cubic spline interpolation of the local form factors and the 'tanh' part is for fast cutoff at large $q(> 3k_F)$. For the cubic-spline interpolation $V(q)_{cubic}$, we use eleven inputs for symmetric and antisymmetric components, $V^s(q)_{cubic}$ and $V^a(q)_{cubic}$, respectively.

Three form factors must be adjusted at $q = \sqrt{3}$, $\sqrt{8}(\sqrt{4})$ and $\sqrt{11}$, one more for $V(q = 0)$ together with the constrain $V(3k_F) = 0$ for both $V^s(q)_{cubic}$ and $V^a(q)_{cubic}$.

In addition, the slope of the curve (an empirical parameter which determines, among other properties, the variation of the gap with strain) is introduced as shown in inset in Fig. 4.1 where two neighboring points at q are defined at $\pm\delta = 0.01$. Figure 4.1 shows our interpolation of symmetric ($V^s(q)$) and antisymmetric ($V^a(q)$) local pseudopotentials for GaAs using relations $V^s(q) = (V_{Ga}(q) + V_{As}(q))/2$ and $V^a(q) = (V_{Ga}(q) - V_{As}(q))/2$ where the ionic potentials for $V_{Ga}(q)$ and $V_{As}(q)$ at $q = 0$ is fitted to Ref. [8]. As stated above, the long-wavelength behavior (small q) of $V(q)$ is not important in our context, since the variation of q due to the strain at $q = \sqrt{3}$, for example, is very small even at the maximum amount of strain (5% tensile) we have considered here. In Table 4.3 we list the form factors fitted to experimental band gaps in relaxed materials and the slopes of the cubic spline interpolation of the local pseudopotentials fitted to the deformation potentials obtained from the calculation of the variation of the energy with strain. As we can see in Table 4.4, the values of the gap at various symmetry points in k-space show good agreement with the experimental data, thus giving us confidence on the form factors and interpolation scheme we have obtained.

The band gap modulation as a function of strain can be clearly observed in Fig. 4.2 in which we show the relative energy shifts at various symmetry points in k-space as a function of strain along (001), (110) and (111) interfaces where the in-plane biaxial strain $\epsilon_{\parallel}$ varies from 5% compressive to 5% tensile. We can see the three top of the valence bands (heavy, light and split-off hole) splitting in all strain direction. For the conduction bands, the Δ minimum splitting is observed in (100) and (110) but (111) strain. On the other hand, $L_{6,c}$ splitting can be seen in both (111) and (110) but (001) strain. These energy band splitting is caused by the broken symmetry of the 1st BZ due to the strain and can be quantified by deformation potentials which can be directly extracted from our band structure calculation.

Table 4.4. Band structure without strain for Si, Ge and III-Vs. E_{gap} is calculated from the bottom of the conduction to the top of the valence band. For Si and Ge, it is an indirect gap where the conduction band minima are located along Δ and at L, respectively. $E_g^{\Gamma_c-\Gamma_v}$, $E_g^{X_c-\Gamma_v}$ and $E_g^{L_c-\Gamma_v}$ are the gap between the first conduction band at Γ, X, and L, respectively, and the top of the valence band. For III-Vs, E_{gap} is equivalent to the $E_g^{\Gamma_c-\Gamma_v}$ showing that a direct gap. Δ_{so} is the spin-orbit splitting and all the units are eV.

Compound		E_{gap}	$E_g^{\Gamma_c-\Gamma_v}$	$E_g^{X_c-\Gamma_v}$	$E_g^{L_c-\Gamma_v}$	Δ_{so}
Si	This work	1.16	3.46	1.3	2.3	0.044
	Literature	1.14[b]; 1.17 [c]	3.5[a]; 3.43[c]	1.12[a]	2.29[a]; 2.33[c]	0.0441[a]; 0.044[b]
Ge	This work	0.794	0.923	0.178	-	0.289
	Literature	0.744[a]; 0.79[b]	0.928[b]; 0.9[c]	1.16[c]	-	0.296[b]; 0.29[c]
GaAs	This work	1.518	-	2.003	1.812	0.340
	Literature	1.52[d]; 1.519[e]	-	2.03[a]; 2.35[b]	1.82[a]; 1.815[e]	0.341[a]; 0.341[e]
GaSb	This work	0.812	-	1.152	0.912	0.765
	Literature	0.811[a]; 0.812[e]	-	1.72[a]; 1.141[e]	1.22[a]; 0.875[e]	0.76[a]; 0.76[e]
InAs	This work	0.416	-	1.477	1.14	0.392
	Literature	0.418[a]; 0.417[e]	-	1.433[e]; 1.37[f]	1.13[e]; 1.07[f]	0.39[e]; 0.4[f]
InSb	This work	0.234	-	1.632	0.97	0.81
	Literature	0.235[a]; 0.235[e]	-	1.63[e]; 1.63[f]	0.93[e]; 1.0[g]	0.81[e]; 0.81[f]
InP	This work	1.425	-	2.252	1.931	0.108
	Literature	1.42[d]; 1.4236[e]	-	2.38[e]; 2.21[f]	2.01[e]; 1.95[g]	0.108[a]; 0.108[e]

[a] From Ref. [58]
[b] From Ref. [29]
[c] From Ref. [18]
[d] From Ref. [84]
[e] From Ref. [87]
[f] From Ref. [1]
[g] From Ref. [83]

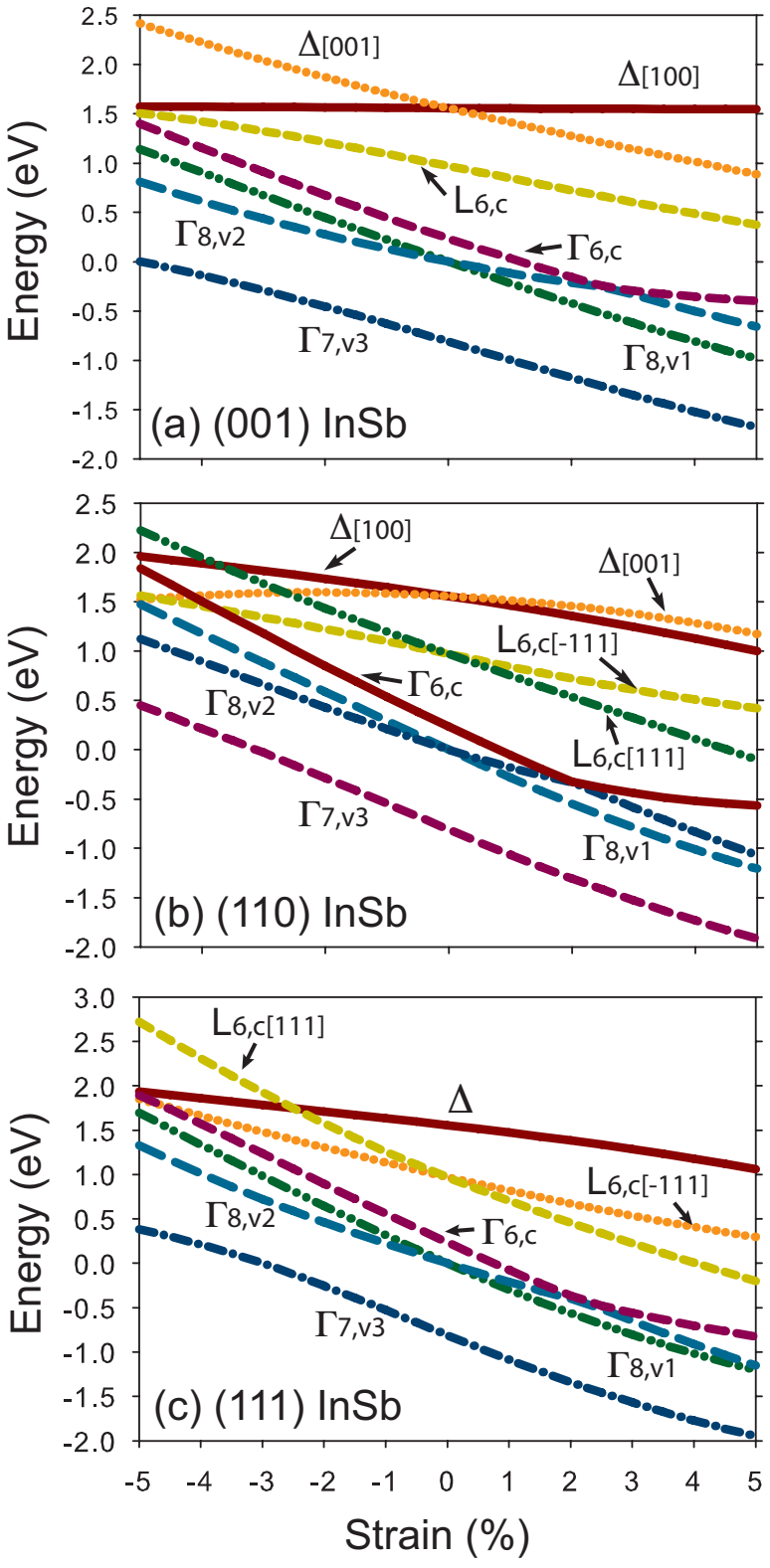

Figure 4.2. Calculated relative shifts of band extrema for InSb at various symmetry points caused by biaxial strain on the (001), (110) and (111) planes. The energy scale is fixed by setting arbitrarily top of the valence band to zero at zero strain.

4.3 Virtual Crystal Approximation

One of the simplest approach employed to calculate the electronic band structure of disordered semiconductor alloys within the EPM framework is the virtual crystal approximation (VCA) which has been widely used before [50, 36, 43, 6, 12]. In the VCA scheme, one can imagine the disordered alloy as approximated by an ordered crystal in which one ion is a 'virtual' ion resulting from the linear interpolation of the pseudopotentials and parameters of the two alloying ions. The disorder will eventually by accounted for as a perturbation affecting electronic transport via alloy scattering. However, it was known that the VCA gives a band gap bowing which was in disagreement with experimental observations [43, 12, 50]. Lee *et. al.* proposed a simple pseudopotential scheme which includes the compositional disorder effect by introducing an effective disorder potential with an adjustable parameter [50]. However, the effects due to the atomic volume Ω in Ref. [50] can be lumped into a single fitting parameter P^{loc} resulting in the following rather simple expression for the local pseudopotential:

$$\begin{aligned} V^{loc}(q) &= xV^{loc}_{AC}(q) + (1-x)V^{loc}_{BC}(q) \\ &- P^{loc}\left[x(1-x)\right]\left(V^{loc}_{AC} - V^{loc}_{BC}\right) . \end{aligned} \tag{4.15}$$

We employ the same approach for the λ^s and λ^a, the symmetric and antisymmetric contributions to the spin-orbit Hamiltonian in Ref. [18]. Thus we express them as:

$$\begin{aligned} \lambda^s &= x\lambda^s_{AC} + (1-x)\lambda^s_{BC} \\ &- P^{so}\left[x(1-x)\right]\left(\lambda^s_{AC} - \lambda^s_{BC}\right) , \end{aligned} \tag{4.16}$$

where P^{so} is an another empirical parameter.

On the contrary, we employ the VCA without introducing any empirical parameter P^{nloc} for the nonlocal potentials. Instead, we linearly interpolate the ionic parameters (including the elastic constants):

$$\alpha_{0,cat} = x\alpha_{0,A(AC)} + (1-x)\alpha_{0,B(BC)} \ , \tag{4.17}$$

where $\alpha_{0,cat}$ is the s-well depth for the 'virtual' cation. We prefer this strategy since the virtual atoms thus created inherit their atomic properties, such as the well radius, from both (AC) and (BC).

By taking this approach, we can have better flexibility in an empirical fashion for the ternary alloys to adjust band-structure results to the known experimental data. In Fig. 4.3 we show the shifts of the band extrema at various symmetry points in first BZ of relaxed $In_xGa_{1-x}As$ and $In_xGa_{1-x}Sb$ using $P^{loc} = -0.405$ and -0.6, and $P^{so} = 2.1$ and -1.5, respectively, as the In mole fraction x varies from 0 (GaAs and GaSb) to 1 (InAs and InSb). It is shown that the heavy ($\Gamma_{8,v1}$) and light ($\Gamma_{8,v2}$) hole bands are degenerated over the entire range of x. In addition, the band extrema vary nonlinearly causing band gap bowing effect. This is clearly shown in Fig. 4.4 for the direct band gap at Γ as a function of x for $In_xGa_{1-x}As$ and $In_xGa_{1-x}Sb$, where we compare our theoretical results to experimental data shown in Ref. [9] and references therein. In Fig. 4.4, the band gap bowing from 'EPM (0K)' obtained from our calculation shows good qualitative agreement with the experimental data. Also, the 'EPM (300K)' data generated from 'EPM (0K)' by using the temperature dependence of $E_g(T)$ from Ref. [58] shows an even better quantitative agreement. In Fig. 4.5 we show the various band gap bowing trends, such as $E_g(X)$, $E_g(L)$ and $E_g(sp)$ as well as $E_g(\Gamma)$ as a function of x.

In order to reproduce the correct band gap at an arbitrary x, we need to quantify the band gap bowing effects using the so-called bowing equation which is generally expressed as quadratic polynomial where a coefficient of the quadratic term called a

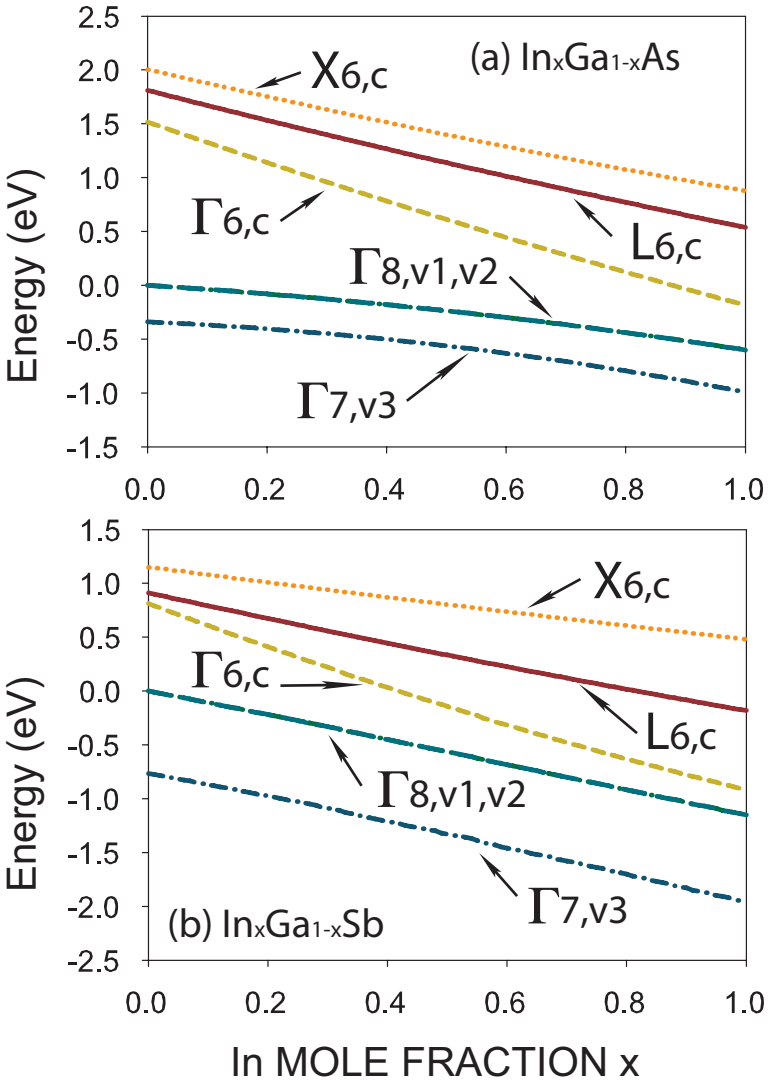

Figure 4.3. Relative band extrema energy shifts of relaxed (a) $In_xGa_{1-x}As$ and (b) $In_xGa_{1-x}Sb$ as a function of In mole fraction x where the top of the valence band is arbitrarily fixed to zero at $x = 0$. The heavy hole ($\Gamma_{8,v1}$) and light hole ($\Gamma_{8,v2}$) bands are degenerated.

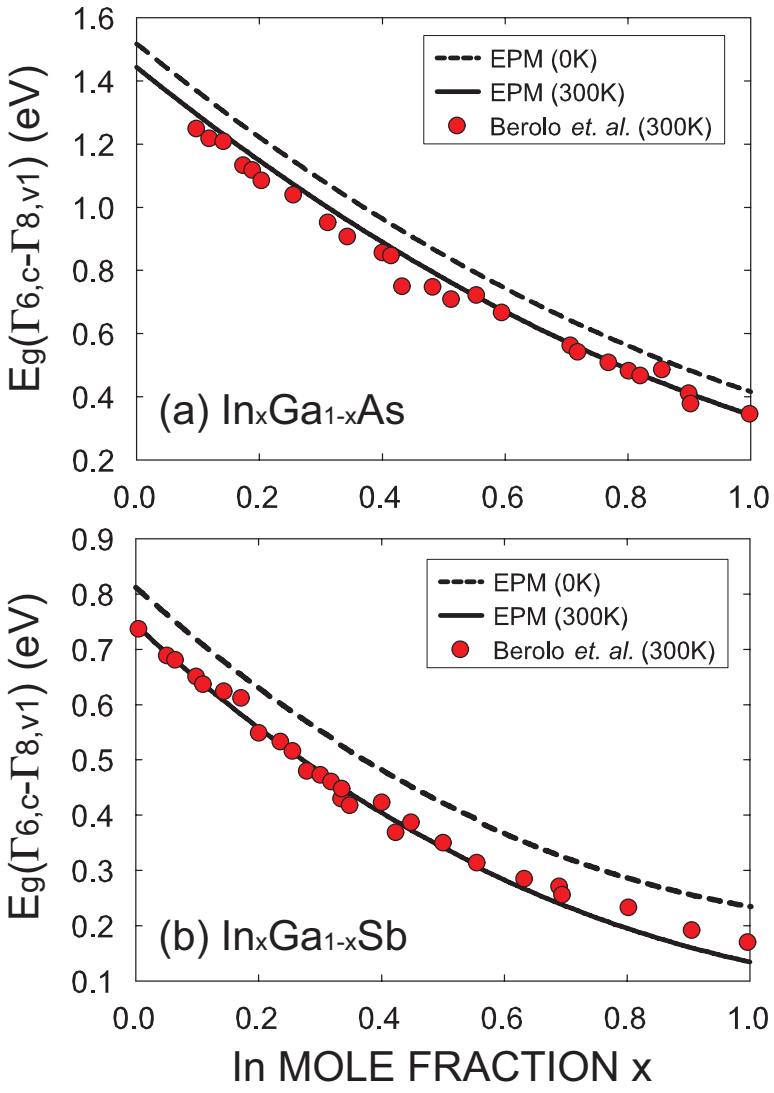

Figure 4.4. Direct band gap bowing at Γ in k-space of relaxed (a) $In_xGa_{1-x}As$ and (b) $In_xGa_{1-x}Sb$ as a function of In mole fraction x. The EPM (0K) (dashed line) is obtained from band structure calculation in this work, the EPM (300K) (solid line) for $In_xGa_{1-x}As$ and $In_xGa_{1-x}Sb$ are obtained using temperature dependence of band gap equations shown in Ref. [58] and references therein, and the Berolo *et.al.* (300K) (symbol) is taken from Ref. [9] and references therein.

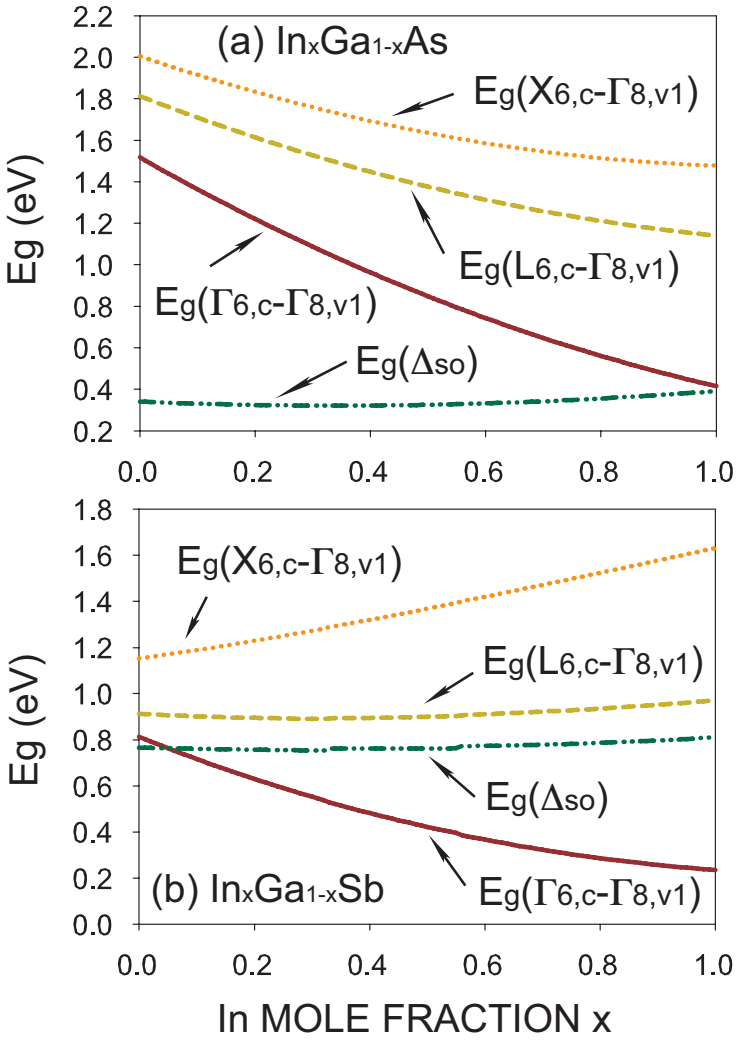

Figure 4.5. Band gap bowing of relaxed (a) $In_xGa_{1-x}As$ and (b) $In_xGa_{1-x}Sb$ as a function of In mole fraction x where the various band gaps at different symmetry points are calculated from the top of the valence band ($\Gamma_{8,v1}$).

bandgap bowing parameter (expressed in units of eV). The bandgap bowing parameters for various bandgaps can be extracted by using least square fitting. The bowing equations for relaxed $In_xGa_{1-x}As$ are:

$$\begin{aligned} E_g(\Delta_{so}) &= 0.340 - 0.111x + 0.163x^2 \\ E_g(\Gamma_{6,c} - \Gamma_{8,v1}) &= 1.517 - 1.573x + 0.473x^2 \\ E_g(L_{6,c} - \Gamma_{8,v1}) &= 1.813 - 1.072x + 0.399x^2 \\ E_g(X_{6,c} - \Gamma_{8,v1}) &= 2.005 - 0.950x + 0.421x^2 \end{aligned} \tag{4.18}$$

and for relaxed $In_xGa_{1-x}Sb$:

$$\begin{aligned} E_g(\Delta_{so}) &= 0.763 - 0.045x + 0.092x^2 \\ E_g(\Gamma_{6,c} - \Gamma_{8,v1}) &= 0.811 - 0.985x + 0.410x^2 \\ E_g(L_{6,c} - \Gamma_{8,v1}) &= 0.909 - 0.099x + 0.164x^2 \\ E_g(X_{6,c} - \Gamma_{8,v1}) &= 1.148 + 0.396x + 0.092x^2 \end{aligned} \tag{4.19}$$

where the direct band gap bowing parameters are $b_{gap} = 0.473$ eV and $b_{gap} = 0.410$ eV for $In_xGa_{1-x}As$ and $In_xGa_{1-x}Sb$, respectively. Our bandgap bowing parameters b_{gap} are in good agreement with the low-temperature theoretical and experimental data shown in Ref. [87] and references therein, and yield for the direct band gap E_g^{Γ} a value of 0.816 eV for the InP lattice-matched $In_{0.53}Ga_{0.47}As$. It is worth to note that the bowing parameters we have obtained are all positive (concave up) for the various band gaps in both relaxed $In_xGa_{1-x}As$ and $In_xGa_{1-x}Sb$.

$In_xGa_{1-x}As$ on InP is regarded as a very promising semiconductor for high-speed electronic devices and optoelectronics applications [26, 48, 33, 20]. In this material one can easily control the in-plane strain ratio by changing the In mole fraction thus affecting the band structure. There have been both theoretical and experimental

observations of the bandgap bowing as the In or Ga mole fraction varies from 0 to 1 in the $In_xGa_{1-x}As$ on (001) InP substrates [33, 48, 91, 34, 45]. However, experimental information for the bowing parameters of other gaps (namely, for the $E_g(X)$, $E_g(L)$ and $E_g(\Delta_{so})$ as a function of x for $In_xGa_{1-x}As$/(110) InP or (111) InP are still lacking. In this study, we provide theoretical predictions for the band structure and the values of the various bandgap bowing parameters in biaxially strained $In_xGa_{1-x}As$ on (001), (110) and (111) InP substrates as a function of the In mole fraction x. We begin by comparing in Fig. 4.6 the computed direct-bandgap ($E_g(\Gamma_{6,c} - \Gamma_{8,v1})$) bowing for strained $In_xGa_{1-x}As$/(001)-on-InP to experimental and theoretical observations from Ref. [34, 91, 48, 45]. Theoretical and experimental data agree quite well, especially for $0.4 < x < 0.6$. It should be noted that we have a discontinuity in derivative of the bandgap *vs.* mole fraction x at $x = 0.53$ due to crossing of the heavy hole ($\Gamma_{8,v1}$) and light hole ($\Gamma_{8,v2}$) bands.

Figure 4.7 shows a variation of the bandgap bowing parameters including direct band gap shown in Fig. 4.6 for InP lattice-matched $In_xGa_{1-x}As$ as a function of x for different interface orientations, (001), (110), and (111). As x moves away from the unstrained value of $x = 0.53$, the degeneracy of the bands at all symmetry points, X , L, and Γ, is lost and the bands begin to split as the biaxial strain is applied for both $x < 0.53$ (tensile strain) and $x > 0.53$ (compressive strain). In addition, the heavy- and light-hole bands cross at x=0.53, thus causing a discontinuity of the slope of the curve, fact already mentioned above and experimentally observed in Ref. [48, 34]. This results in different bandgap bowing parameters in $x < 0.53$ and $x > 0.53$ for all interface orientations. Note also the splitting of the X valleys for the (001) and (110) cases and the splitting of the L valleys for the (111) and (110) cases which is expected from the broken symmetry caused by the in-plane strain. Thus, we can expect that the band gap bowing parameters strongly depend on the

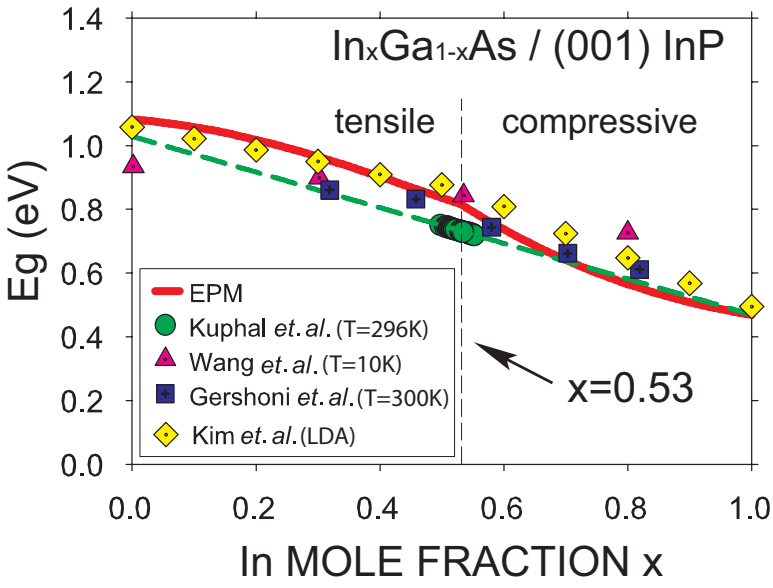

Figure 4.6. The EPM calculation (straight line) of direct band gap $E_g(\Gamma_{6,c}-\Gamma_{8,v1})$ of $In_xGa_{1-x}As$ on (001) InP substrate is compared to various experimental data [33, 91, 48] and theoretical calculation [45] (symbols). The horizontal dashed line is obtained by linearly extrapolating the result from Ref. [48]. Very good agreement is shown when the In mole fraction $0.4 < x < 0.6$.

interface orientation of the substrate. In Table 4.5 we show the various bandgap bowing equations for $In_xGa_{1-x}As$ on (001), (110), and (111) InP for the two cases $x > 0.53$ and $x < 0.53$. The bowing parameters for the direct gap $E_g(\Gamma_{6,c} - \Gamma_{8,v1})$ are positive (concave up) when the alloy is compressively strained ($x > 0.53$) for all interface orientations of InP we have considered. By contrast, the bowing parameters are negative (concave down) when the alloy is stretched ($x > 0.53$) on (001) and (110), but not for the (111) case. In addition, when the alloy is strained on (001) InP, the magnitude of the bowing parameter for the direct gap is the larger than the values obtained for the (110) and (111) cases.

4.4 Deformation Potential Theory

The distortion of the crystal structure due to strain changes the electronic energies at different symmetry points in the first Brillouin Zone (BZ). The parameters that

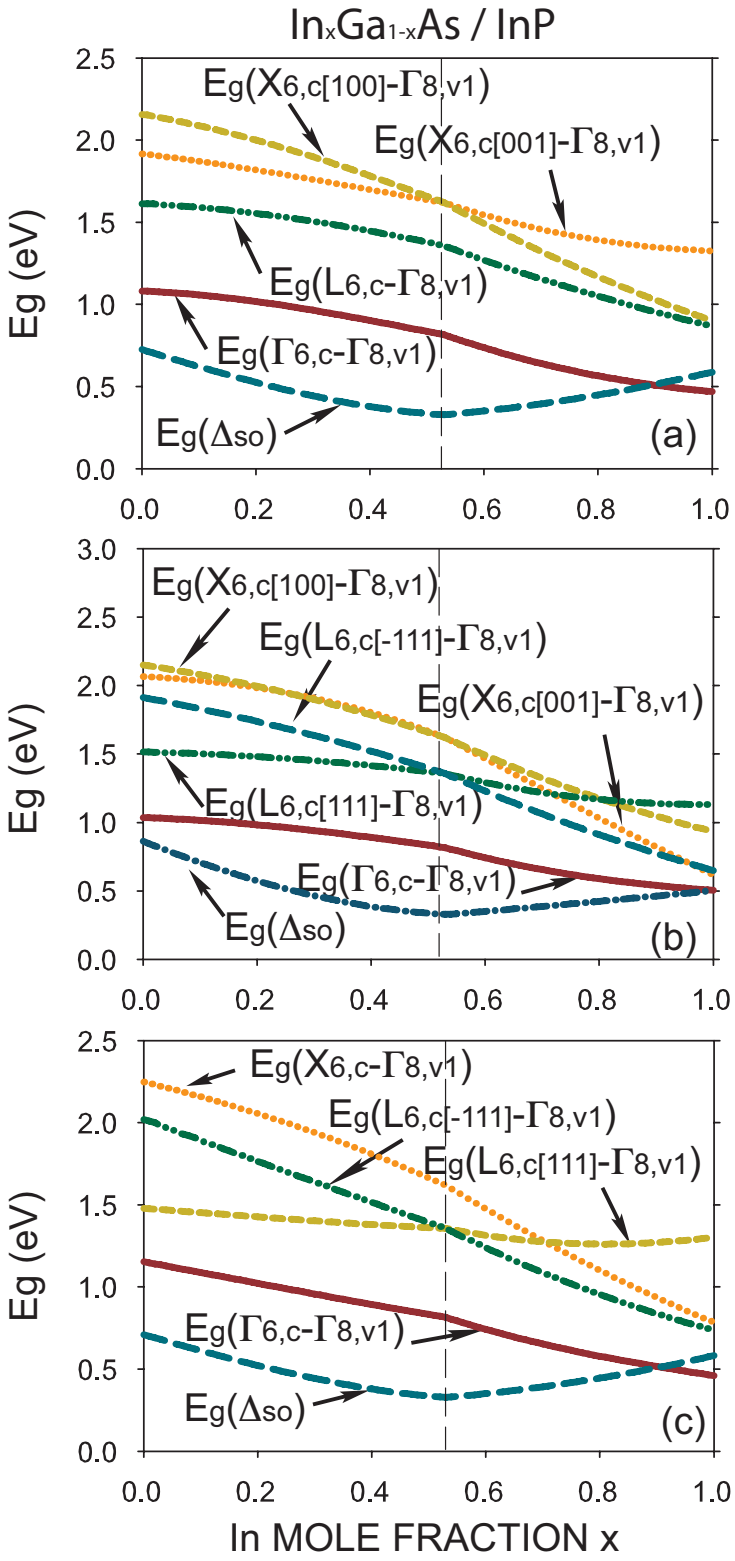

Figure 4.7. Various band gap changes from the top of the valence band ($\Gamma_{8,v1}$) of $In_xGa_{1-x}As$ on (a) (001), (b) (110) and (c) (111) InP. Different band gap bowings are observed between $x > 0.53$ (compressive) and $x < 0.53$ (tensile).

Table 4.5. Bandgap bowing equations and bowing parameters for $In_xGa_{1-x}As$ on InP with different interface orientations. The coefficient of the quadratic term is the bowing parameter and it is in units of eV.

In mole	Band gap	Interface orientation (001)	(110)	(111)
$x > 0.53$	$E_g(\Delta_{so})$	$0.314 - 0.255x + 0.529x^2$	$0.168 + 0.257x + 0.077x^2$	$0.312 - 0.267x + 0.529x^2$
	$E_g(\Gamma_{6,c} - \Gamma_{8,v1})$	$1.713 - 2.201x + 0.958x^2$	$1.638 - 2.032x + 0.901x^2$	$1.540 - 1.706x + 0.630x^2$
	$E_g(L_{6,c[111]} - \Gamma_{8,v1})$	$2.147 - 1.735x + 0.455x^2$	$2.192 - 2.162x + 1.101x^2$	$2.057 - 1.966x + 1.213x^2$
	$E_g(L_{6,c[-111]} - \Gamma_{8,v1})$	-	$2.540 - 2.627x + 0.737x^2$	$2.510 - 2.636x + 0.864x^2$
	$E_g(X_{6,c[001]} - \Gamma_{8,v1})$	$2.528 - 2.294x + 1.093x^2$	$2.875 - 2.487x + 0.228x^2$	$2.939 - 2.865x + 0.711x^2$
	$E_g(X_{6,c[100]} - \Gamma_{8,v1})$	$2.808 - 2.620x + 0.713x^2$	$2.887 - 2.887x + 0.934x^2$	-
$x < 0.53$	$E_g(\Delta_{so})$	$0.730 - 1.193x + 0.794x^2$	$0.866 - 1.738x + 1.350x^2$	$0.714 - 1.109x + 0.692x^2$
	$E_g(\Gamma_{6,c} - \Gamma_{8,v1})$	$1.086 - 0.245x - 0.521x^2$	$1.037 - 0.188x - 0.443x^2$	$1.155 - 0.679x + 0.068x^2$
	$E_g(L_{6,c[111]} - \Gamma_{8,v1})$	$1.615 - 0.195x - 0.560x^2$	$1.154 - 0.090x - 0.394x^2$	$1.480 - 0.286x + 0.094x^2$
	$E_g(L_{6,c[-111]} - \Gamma_{8,v1})$	-	$1.912 - 0.764x - 0.536x^2$	$2.022 - 1.300x + 0.084x^2$
	$E_g(X_{6,c[001]} - \Gamma_{8,v1})$	$1.919 - 0.465x - 0.201x^2$	$2.061 - 0.108x - 1.354x^2$	$2.246 - 0.809x - 0.709x^2$
	$E_g(X_{6,c[100]} - \Gamma_{8,v1})$	$2.160 - 0.669x - 0.678x^2$	$2.150 - 0.638x - 0.690x^2$	-

describes these changes are known as deformation potentials [98]. For instance, the strain along the [001] direction, perpendicular to the (001) plane, causes a splitting of the valence bands at Γ and between the 4-fold degenerate minima along the Δ lines towards the X symmetry points lying along the in-plane [100], [$\overline{1}$00], [010] and [0$\overline{1}$0] directions, and the remaining 2-fold minima lying on the symmetry lines Λ towards the Z points along the out-of-plane [001] and [00$\overline{1}$] directions, as can be seen in Fig. 4.2. The parameters related to the valence band splitting are the deformation potential b and d corresponding to the strain along [001] and [111], respectively.

When the strain is small, the electronic energy splittings of both valence and conduction bands can be assumed to be linearly proportional to strain. Considering first the valence bands labeled by their total angular momentum quantum numbers (J, J_z) [70, 15], $v_1(J=\frac{3}{2}, |\frac{3}{2}, \frac{1}{2}\rangle)$, $v_2(J=\frac{3}{2}, |\frac{3}{2}, \frac{3}{2}\rangle)$ and $v_3(J=\frac{1}{2}, |\frac{1}{2}, \frac{1}{2}\rangle)$, we can follow Van de Walle *et. al.* [85, 84] and refer to the average energy of these band at Γ as $E_{v,av}$ where shifts of the valence bands for the uniaxial strain along [001], which is *qualitatively* equivalent to the biaxial strain on (001), with respect to the weighted average $E_{v,av}$ as,

$$\begin{aligned}
\Delta E_{v2} &= \frac{1}{3}\Delta_{so} - \frac{1}{2}\delta E_{001} \\
\Delta E_{v1} &= -\frac{1}{6}\Delta_{so} + \frac{1}{4}\delta E_{001} + \frac{1}{2}\left[\Delta_{so}^2 + \Delta_{so}\delta E_{001} + \frac{9}{4}(\delta E_{001})^2\right]^{1/2} \\
\Delta E_{v3} &= -\frac{1}{6}\Delta_{so} + \frac{1}{4}\delta E_{001} - \frac{1}{2}\left[\Delta_{so}^2 + \Delta_{so}\delta E_{001} + \frac{9}{4}(\delta E_{001})^2\right]^{1/2}
\end{aligned} \tag{4.20}$$

where $\delta E_{001} = 2b(e_{zz} - e_{xx})$. The constant b is the deformation potential and the strain tensor components e_{xx} and e_{zz} are $\epsilon_{\parallel}$ and $\epsilon_{\perp}$, respectively. For the strain along [111] which is also equivalent to the biaxial strain on (111) in quality, the Eq. 4.20 is still valid with δE_{001} replaced by $\delta E_{111} = 2\sqrt{3}de_{xy}$ where $e_{xy} = (\epsilon_{\perp} - \epsilon_{\parallel})/3$. However, there is no analytical expression for the valence band splitting due to the strain along [110] direction in which the splitting is a mixture of the deformation potential b and

d. In this case, the valence band splitting can be calculated by solving the eigenvalues of the matrix [70],

$$\begin{bmatrix} \frac{\Delta_{so}}{3} - \frac{1}{8}(\delta E_{001} + 3\delta E_{111}) & -\frac{\sqrt{3}}{8}(\delta E_{001} - \delta E_{111}) & \frac{\sqrt{6}}{8}(\delta E_{001} - \delta E_{111}) \\ -\frac{\sqrt{3}}{8}(\delta E_{001} - \delta E_{111}) & \frac{\Delta_{so}}{3} + \frac{1}{8}(\delta E_{001} + 3\delta E_{111}) & \frac{\sqrt{2}}{8}(\delta E_{001} + 3\delta E_{111}) \\ \frac{\sqrt{6}}{8}(\delta E_{001} - \delta E_{111}) & \frac{\sqrt{2}}{8}(\delta E_{001} + 3\delta E_{111}) & -\frac{2}{3}\Delta_{so} \end{bmatrix} \tag{4.21}$$

where $\delta E_{001} = 4b(e_{xx} - e_{zz})$ and $\delta E_{111} = (4/\sqrt{3})de_{xy}$. The strain tensor components are $e_{xx} = (\epsilon_\perp + \epsilon_\parallel)/2$, $e_{zz} = \epsilon_\parallel$ and $e_{xy} = (\epsilon_\perp - \epsilon_\parallel)/2$.

For the conduction band shift in the presence of the strain, Herring *et. al.* suggested an expression for the energy shift of valley i for a homogeneous deformation which is described by the strain tensor $\mathbf{e}$ as [41],

$$\Delta E_c^i = [\Xi_d \mathbf{1} + \Xi_u \{\hat{\boldsymbol{a}}_{\boldsymbol{i}} \hat{\boldsymbol{a}}_{\boldsymbol{j}}\}] : \mathbf{e} \tag{4.22}$$

where Ξ_u and Ξ_d are called uniaxial and dilation deformation potential, respectively, $\mathbf{1}$ is the unit tensor, $\hat{\boldsymbol{a}}_{\boldsymbol{i}}$ is a unit vector parallel to the $\vec{k}$ vector of the valley i, $\{\}$ denote a dyadic form from I. Balslev [5] and the dyadic product $\mathbf{a} : \mathbf{b}$ is defined as,

$$\mathbf{a} : \mathbf{b} = \sum_i \sum_{j \leqslant i} a_{ij} b_{ij} \tag{4.23}$$

From Eq. 4.22, we can express the shifts of individual bands with respect to the average $E_{c,av}$. Under the uniaxial strain along [001] direction, the bands along [001] split off from the bands along [100] and [010]. Then, Eq. 4.22 along [001] can be written,

$$\begin{aligned} \Delta E_c^{001} &= \Xi_d \mathbf{1} : \mathbf{e} + \Xi_u \{\hat{\boldsymbol{a}}_{\mathbf{001}} \hat{\boldsymbol{a}}_{\mathbf{001}}\} : \mathbf{e} \\ &= \Xi_d \mathbf{1} : \mathbf{e} + \Xi_u \boldsymbol{D}_{\mathbf{001}} : \mathbf{e} \end{aligned} \tag{4.24}$$

where we define $(\boldsymbol{D_{001}})_{ij} = (\hat{\boldsymbol{a}}_{\mathbf{001}}\hat{\boldsymbol{a}}_{\mathbf{001}})_{ij}$. Then the first term on the right side can be expanded as,

$$\begin{aligned}\Xi_d\mathbf{1} : \mathbf{e} &= \Xi_d\left[1_{11}e_{11} + 1_{21}e_{21} + 1_{22}e_{22} + 1_{31}e_{31} + 1_{32}e_{32} + 1_{33}e_{33}\right] \\ &= \Xi_d\left[1_{11}e_{11} + 1_{12}e_{12} + 1_{13}e_{13} + 1_{22}e_{22} + 1_{23}e_{23} + 1_{33}e_{33}\right] \qquad (4.25)\end{aligned}$$

by symmetry of $\mathbf{1}$ and $\mathbf{e}$. The second term on the right side becomes,

$$\begin{aligned}\Xi_u\boldsymbol{D_{001}} : \mathbf{e} &= \Xi_u\{(D_{001})_{11}e_{11} + (D_{001})_{12}e_{12} + (D_{001})_{13}e_{13} \\ &+ (D_{001})_{22}e_{22} + (D_{001})_{23}e_{23} + (D_{001})_{33}e_{33}\} \qquad (4.26)\end{aligned}$$

Then Eq. 4.24 can be expanded as,

$$\begin{aligned}\Delta E_c^{001} &= \Xi_d\{1_{11}e_{11} + 1_{12}e_{12} + 1_{13}e_{13} + 1_{22}e_{22} + 1_{23}e_{23} + 1_{33}e_{33}\} \\ &+ \Xi_u\{(D_{001})_{11}e_{11} + (D_{001})_{12}e_{12} + (D_{001})_{13}e_{13} \\ &+ (D_{001})_{22}e_{22} + (D_{001})_{23}e_{23} + (D_{001})_{33}e_{33}\} \qquad (4.27)\end{aligned}$$

Similarly,

$$\begin{aligned}\Delta E_c^{100} &= \Xi_d\{1_{11}e_{11} + 1_{12}e_{12} + 1_{13}e_{13} + 1_{22}e_{22} + 1_{23}e_{23} + 1_{33}e_{33}\} \\ &+ \Xi_u\{(D_{100})_{11}e_{11} + (D_{100})_{12}e_{12} + (D_{100})_{13}e_{13} \\ &+ (D_{100})_{22}e_{22} + (D_{100})_{23}e_{23} + (D_{100})_{33}e_{33}\} \qquad (4.28)\end{aligned}$$

Therefore, the splitting of the conduction bands along [001] and [100] can be written,

$$\begin{aligned}\Delta E_c^{001} - \Delta E_c^{100} &= \Xi_u\big\{\{(D_{001})_{11} - (D_{100})_{11}\}e_{11} + \{(D_{001})_{12} - (D_{100})_{12}\}e_{12} \\ &+ \{(D_{001})_{13} - (D_{100})_{13}\}e_{13} + \{(D_{001})_{22} - (D_{100})_{22}\}e_{22} \\ &+ \{(D_{001})_{23} - (D_{100})_{23}\}e_{23} + \{(D_{001})_{33} - (D_{100})_{33}\}e_{33}\big\} \qquad (4.29)\end{aligned}$$

where,

$$(\boldsymbol{D_{001}})_{ij} = (\hat{\boldsymbol{a}}_{\mathbf{001}}\hat{\boldsymbol{a}}_{\mathbf{001}})_{ij} = \begin{bmatrix} 0 & 0 & 0 \\ 0 & 0 & 0 \\ 0 & 0 & 1 \end{bmatrix}, \quad (\boldsymbol{D_{100}})_{ij} = (\hat{\boldsymbol{a}}_{\mathbf{100}}\hat{\boldsymbol{a}}_{\mathbf{100}})_{ij} = \begin{bmatrix} 1 & 0 & 0 \\ 0 & 0 & 0 \\ 0 & 0 & 0 \end{bmatrix} \tag{4.30}$$

Then, we can simplify the Eq. 4.29 as,

$$\begin{aligned} \Delta E_c^{001} - \Delta E_c^{100} &= \Xi_u(e_{33} - e_{11}) \\ &= \Xi_u(e_{zz} - e_{xx}) \\ &= \Xi_u^{\Delta}(\epsilon_{\perp} - \epsilon_{\parallel}) \end{aligned} \tag{4.31}$$

where the superscript Δ on Ξ_u indicates which type of conduction band valley (at Δ or L). Similarly, the splitting of the conduction bands along [001] and [010] can be shown as,

$$\Delta E_c^{001} - \Delta E_c^{010} = \Xi_u(e_{33} - e_{22}) = \Xi_u^{\Delta}(\epsilon_{\perp} - \epsilon_{\parallel}) \tag{4.32}$$

We can notice that the Eq. 4.31 and Eq. 4.32 are equivalent, so we can simply write as,

$$\Delta E_c^{001} - \Delta E_c^{100,010} = \Xi_u^{\Delta}(\epsilon_{\perp} - \epsilon_{\parallel}) \tag{4.33}$$

The conduction band shifts at L valley also can be derived in a similar way using Eq. 4.24. However, the strain along [001] direction does not affect on the splitting of the conduction band at L valley. Instead, the strain along [110] and [111] split off the bands at L valley. The conduction bands splitting of L valley due to the [111] strain can be shown as,

$$\Delta E_c^{111} - \Delta E_c^{\bar{1}11,1\bar{1}1,11\bar{1}} = \frac{8}{3}\Xi_u^L e_{xy} = \frac{8}{9}\Xi_u^L(\epsilon_{\perp} - \epsilon_{\parallel}) \tag{4.34}$$

and due to the [110] strain is,

$$\Delta E_c^{111,11\bar{1}} - \Delta E_c^{\bar{1}11,1\bar{1}1} = \frac{4}{3}\Xi_u^L e_{xy} = \frac{2}{3}\Xi_u^L(\epsilon_\perp - \epsilon_\parallel) \tag{4.35}$$

The shift of the mean energy of the conduction band minimum is given by

$$\Delta E_c = (\Xi_d + \frac{1}{3}\Xi_u)\mathbf{1} : \mathbf{e} \tag{4.36}$$

and the shift of mean energy of the valence band maximum at Γ is given

$$\Delta E_v = a\mathbf{1} : \mathbf{e} \tag{4.37}$$

where a is the valence band dilation deformation potential and ΔE_v is often known as the hydrostatic shift. Therefore, the shift of the mean energy gap can be shown using Eq. 4.24 and Eq. 4.27 as,

$$\Delta E_g = (\Xi_d + \frac{1}{3}\Xi_u - a)\mathbf{1} : \mathbf{e} \tag{4.38}$$

We can now extract the relative shifts of the valence and conduction band minima corresponding to the deformation potentials b, d, Ξ_u^Δ, Ξ_u^L and the linear combination $(\Xi_d + \frac{1}{3}\Xi_u - a)$ corresponding to relative shifts of band extrema as a function of the strain along [001] and [111] directions.

Extracting these deformation potentials from the band structure calculation using EPM with strain is straightforward [30]. For example, in Fig. 4.8, we plot three top of the valence bands from both EPM (symbols) and the linear deformation potential theory (lines) for the biaxial strain on (111) interface of GaAs to extract the deformation potential d as a fitting parameter. We modulate the d until the 'DFT' (lines) match the 'EPM' (symbols) in a small range of strain (or linear region), for instance

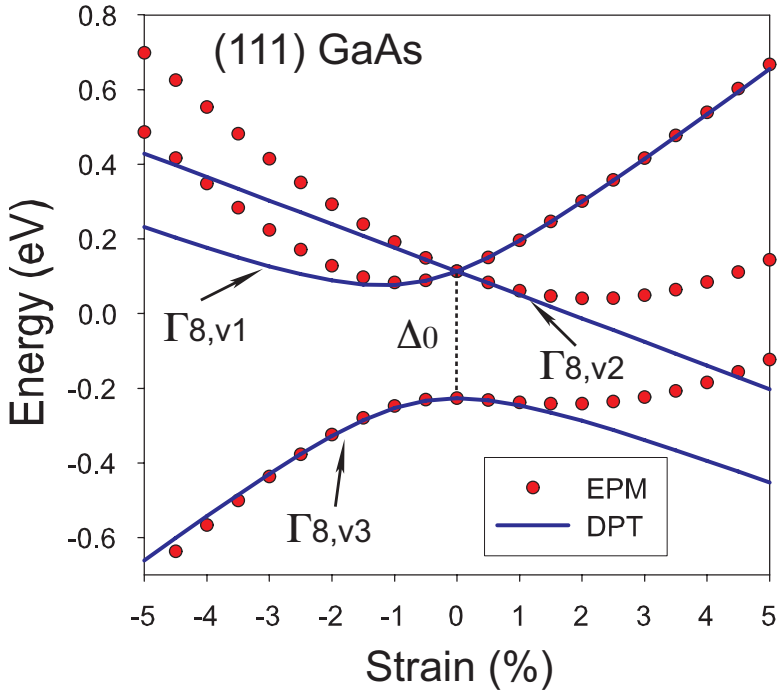

Figure 4.8. Calculated maxima of the three highest-energy valence bands for GaAs under biaxial strain on (111) plane. The red symbols are obtained from EPM and blue lines from the linear deformation potential approximation, $\delta E_{111} = 2\sqrt{3}de_{xy}$. The bdeformation potential d is determined by fitting the blue lines to the red symbols.

-0.01 to 0.01 corresponding to 1% compressive and tensile strain, respectively. In this case, the deformation potential d is determined to be -4.5. Also, we can notice that $\Delta E_{\Gamma_{8,v1}} + \Delta E_{\Gamma_{8,v3}} + \Delta E_{\Gamma_{8,v3}} = 0$ in Fig. 4.8 as expected from Eq. 4.20. However, dilation deformation potentials, Ξ_d and a are related to absolute shifts of the band extrema, which simply cannot be extracted from the EPM calculation with periodic boundary condition, since the absolute position of an energy level in an infinity periodic crystal is not well defined for, so called, the 'absolute deformation potential' calculation [52]. Several approaches have been made to compute the absolute deformation potential using 'model solid theory' [84], 'ab initio all-electron method and lattice harmonic expansion' [52], carrier mobilities fitting to known experimental data [30] and so on. However, in this study we do not calculate the absolute deformation potential. Instead, we directly extract the linear combination $(\Xi_d + \frac{1}{3}\Xi_u - a)$

from the EPM as mentioned above by setting arbitrary value of the top of the valence band.

In Tables 4.6 and 4.7 we list deformation potentials for the valence and conduction bands, respectively, extracted from EPM calculations compared to available data from literatures. The valence band deformation potentials b and d are all negative and the magnitude of d is larger than b, implying that the valence-band energy-shifts are larger under (111) biaxial strain than (001). The uniaxial deformation potential Ξ_u is larger at the L minima than at the Δ minima in all semiconductors, implying that the conduction band minima at L are also more sensitive to (111) strain than (001). The linear combination of the dilation deformation potential $(\Xi_d + \Xi_u/3 - a)$ at the Δ minima is larger than at the L minima. In addition, for Si and Ge they have opposite signs at Δ and L, implying an opposite behavior of the average $\Gamma - L$ and $\Gamma - \Delta$ gaps under biaxial strain. As we mentioned earlier, the deformation potentials are sensitive to the cubic spline interpolation parameters, especially to the slopes of the local pseudopotential at a given q. Also, it is known that the d and Ξ_u^L are sensitive to the internal displacement parameter ζ [85].

4.5 Effective Masses

The various effective masses of carriers also can be calculated from the band structure at different symmetric points (X, Γ and L). Numerically the effective mass can be calculated as a finite difference:

$$m^* = \frac{\hbar^2 (\Delta k)^2}{E_{i+1} - 2E_i + E_{i-1}} \ , \tag{4.39}$$

where $\Delta k = \sqrt{{\Delta k_x}^2 + {\Delta k_y}^2 + {\Delta k_z}^2}$ and Δk_x, Δk_x and Δk_x have a dependence of the strain direction in k-space. For (001) biaxial strain,

Table 4.6. Shear deformation potentials (in units of eV) extracted from calculated relative shifts of top of the valence bands as a function of in-plane strain along (001) and (111).

Compound		b	d
Si	This work	-2.3	-5.5
	literature	-2.33[a] -2.35[b] -2.27[c]	-4.75[a] -5.32[b] -3.69[c]
Ge	This work	-1.8	-7.0
	literature	-2.16[a] -2.55[b] -3.11[c]	-6.06[a] -5.5[b] -4.65[c]
GaAs	This work	-2.79	-7.5
	literature	-1.9[b] -2.0[d] -2.79[e] -1.7[f]	-4.23[b] -4.5[d] -4.77[e] -4.8[g]
GaSb	This work	-1.6	-5.0
	literature	-2.0[d] -2.3[e] -1.9[f] -2.0[f]	-4.7[d] -3.98[e] -4.8[h]
InAs	This work	-1.72	-3.3
	literature	-1.55[b] -1.8[d] -2.33[e] -1.7[f] -1.8[f]	-3.1[b] -3.6[d] -3.83[e]
InSb	This work	-2.3	-5.2
	literature	-2.0[d] -2.0[e] -1.9[f]	-4.8[d] -5.0[d] -3.55[e] -4.7[g]
InP	This work	-1.6	-4.2
	literature	-2.0[d] -1.55[d] -2.11[e] -1.9[f]	-5.0[d] -4.2[d] -3.54[e]

[a] From Ref. [30]
[b] From Ref. [84]
[c] From Ref. [31]
[f] From Ref. [57]
[e] From Ref. [71]
[f] From Ref. [79]
[g] From Ref. [87]
[h] From Ref. [62]

Table 4.7. Uniaxial deformation potential Ξ_u and its linear combination $\Xi_d + \Xi_u/3$ with the dilation deformation potentials (in units of eV) extracted from the relative shifts of conduction band extrema as a function of in-plane strain on the (001) and (111) surfaces.

Compound		Ξ_u^{Δ}	Ξ_u^{L}	$\Xi_d^{\Delta} + \Xi_u^{\Delta}/3 - a$	$\Xi_d^{L} + \Xi_u^{L}/3 - a$
Si	This work	10.1	15.1	6.6	-3.0
	literature	10.5[a]; 9.16[b]; 8.47[c]	18.0[a]; 16.14[b]; 12.35[c]	2.5[a]; 1.72[d]	-3.1[a]; -3.12[d]
Ge	This work	9.65	15.5	5.9	-1.13
	literature	9.75[a]; 9.42[b]; 7.46[c]	16.8[a]; 15.13[b]; 11.07[c]	5.75[a]; 1.31[d]	-0.83[a]; -2.78[d]
GaAs	This work	4.7	10.2	13	7.6
	literature	8.61[b]	14.26[b]	-	-
GaSb	This work	8.0	10.9	13.6	3.9
	literature	-	-	-	-
InAs	This work	5.5	12.1	11.8	4.5
	literature	4.5[b]	11.35[b]	-	-
InSb	This work	6.8	8.2	13.6	5.8
	literature	-	-	-	-
InP	This work	6.7	8.6	14.8	4.24
	literature	-	-	-	-

[a] From Ref. [30]
[b] From Ref. [84]
[c] From Ref. [31]
[d] From Ref. [85]

$$\Delta k_x = (\delta k \sin\beta \cos\alpha)/(1+\epsilon_{\parallel})$$
$$\Delta k_y = (\delta k \sin\beta \sin\alpha)/(1+\epsilon_{\parallel})$$
$$\Delta k_z = (\delta k \cos\beta)/(1+\epsilon_{\perp}) \ , \tag{4.40}$$

where α and β are the angle from x and z-axis, respectively, in Cartesian coordinates and determined by the position of symmetric points in the first BZ. For instance, longitudinal $m_{e,l}^{*(L)}$ and transverse $m_{e,t}^{*(L)}$ electron effective masses at L as a function of strain is calculated using $\alpha = \pi/4$, $\beta = \cos^{-1}(1/\sqrt{3})$ and $\alpha = \pi/4$, $\beta = \pi/2 - \cos^{-1}(1/\sqrt{3})$, respectively. The quantity δk in Eq. 4.40 originates from the second derivative in the analytical expression in Eq. 4.39. It is important to find an optimum value for it, small enough to approximate correctly the derivative but simultaneously large enough to avoid artifacts due to the numerical noise affecting the calculation of the eigenvalues. As an example of how we have optimized the quantity δk, in Fig. 4.9 we show the transverse electron effective mass of Ge at the symmetry point L, $m_{e,t}^{*(L)}$, as a function of strain and δk. Evidently $m_{e,t}^{*(L)}$ at a given value of strain shows unreliable numerical noises as the δk decreases, but it 'saturates' to a constant value as δk increases above a critical value as a function of strain, symmetry point, and material. In order to save computational efforts, rather than optimizing δk in each case, we employ a fixed value of about $10^{-6} \sim 10^{-5}$. In Fig. 4.9 that for strained Ge, $\delta k = 10^{-5}$ is numerically tolerable in all cases.

In this study, the longitudinal ($m_{e,l}^{*}$) and transverse ($m_{e,t}^{*}$) electron effective masses at Δ, L, Γ, and the effective masses of the heavy, light, and split-off hole at the top of the three highest-energy valence bands at Γ, $m_{hh}^{*(\Gamma)}$, $m_{lh}^{*(\Gamma)}$ and $m_{so}^{*(\Gamma)}$, respectively, are calculated as a function of biaxial strain on surfaces of different orientations, (001), (110), and (111). We should mention that $m_{hh}^{*(\Gamma)}$ and $m_{lh}^{*(\Gamma)}$ are computed along three different crystal orientations due to the highly anisotropic nature of the constant energy surfaces. The effective masses for relaxed semiconductors are shown

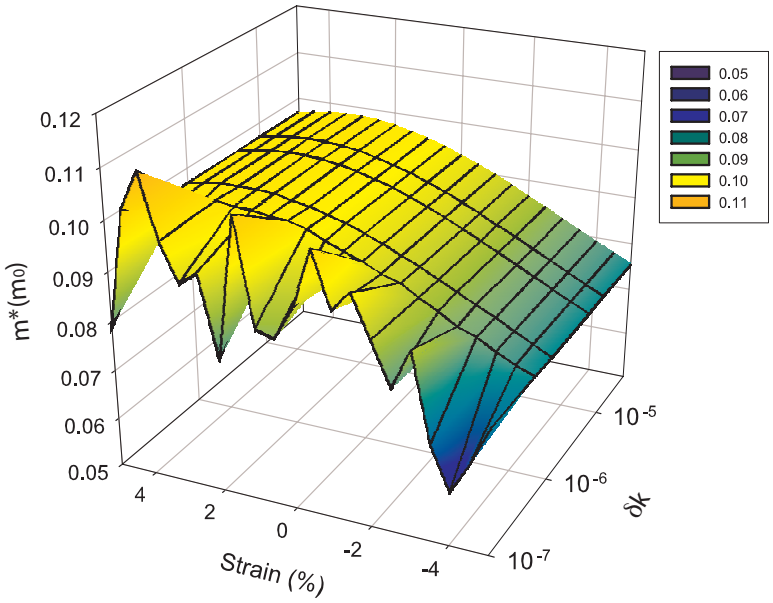

Figure 4.9. Transverse electron effective mass (in units of m_0) of Ge at L. Strain is varied from 5% tensile to 5% compressive. The quantity δk is selected so as to minimize the effect of numerical noise.

in Tables 4.8 and 4.9, compared to data from various literatures. In Table 4.8 note the isotropy of $m_e^{*(\Gamma)}$ due to the isotropic (s-like) nature of the conduction band minimum at Γ. Note also that $m_{e,l}^*$ and $m_{e,t}^*$ are almost proportional to the band gaps since the curvature of the bands at symmetry points (denominator in Eq. 4.39) is inversely proportional to the gaps. The valence bands at Γ are highly anisotropic (p-like state), as shown by the fact that $m_{hh}^{*(\Gamma)}$ and $m_{lh}^{*(\Gamma)}$ exhibit a strong dependence on crystal orientation. The effective mass $m_{hh}^{*(\Gamma)}$ is the largest along the [111] direction but $m_{lh}^{*(\Gamma)}$ is the largest along the [001] direction. Finally, $m_{so}^{*(\Gamma)}$ shows no dependence on crystal orientation, showing that the split-off band is 'almost' isotropic.

Having shown above the effect of strain on the band structure, so now we present the dependence of the effective masses on biaxial strain on different interface orientations. In Fig. 4.10 we show the hole effective masses in units of m_0 as biaxial strain varies from -5% to 5% on (001), (110), and (111) interfaces. We observe a crossover between $m_{lh}^{*(\Gamma)}$ and $m_{so}^{*(\Gamma)}$ at $\sim$ 1% compressive strain in GaAs along all directions we have

Table 4.8. Bulk conduction band effective masses at various symmetry points (L, Γ and Δ minima) in k-space (in units of m_0) where the subscripts l and t represent longitudinal and transverse effective masses, respectively.

Compound		$m_{e,l}^{*(L)}$	$m_{e,t}^{*(L)}$	$m_{e,(l,t)}^{*(\Gamma)}$	$m_{e,l}^{*(\Delta)}$	$m_{e,t}^{*(\Delta)}$
Si	This work	1.950	0.154	0.488	0.891	0.202
	literature	1.418[a], 1.973[b]	0.130[a], 0.153[b]	0.188[a], 0.212[b]	0.9163[a], 0.905[b]	0.1905[a], 0.191[b]
Ge	This work	1.578	0.093	0.047	0.889	0.194
	literature	1.61[a], 1.568[b]	0.081[a], 0.094[b]	0.038[a], 0.049[b]	1.35[a], 1.851[b]	0.29[a], 0.195[b]
GaAs	This work	1.610	0.126	0.082	1.705	0.236
	literature	1.9[a], 1.648[b]	0.0754[a], 0.123[b]	0.067[a], 0.071[b]	1.3[a], 1.460[b]	0.23[a], 0.243[b]
GaSb	This work	1.493	0.103	0.049	0.950	0.210
	literature	1.4[a], 1.3[c]	0.085[a], 0.10[c]	0.039[a], 0.039[c]	1.3[a], 1.51[c]	0.33[a], 0.22[c]
InAs	This work	1.707	0.106	0.026	7.079	0.232
	literature	3.57[a], 1.875[b]	0.12[a], 0.120[b]	0.024[a], 0.038[b], 0.023-0.03[c]	1.32[a], 1.981[b]	0.28[a], 0.246[b]
InSb	This work	1.697	0.113	0.017	0.956	0.232
	literature			0.013[a], 0.012-0.015[c]		
InP	This work	1.783	0.137	0.085	1.409	0.243
	literature	1.64[a], 2.188[b]	0.13[a], 0.172[b]	0.07927[a], 0.104[b], 0.068-0.084[c]	1.26[a], 0.985[b]	0.34[a], 0.276[b]

[a] From Ref. [2]
[b] From Ref. [29]
[c] From Ref. [87]

Table 4.9. Bulk heavy($m_{hh}^{*(\Gamma)}$), light($m_{lh}^{*(\Gamma)}$) and spin-orbit($m_{sp}^{*(\Gamma)}$) hole effective masses (in units of m_0) along [001], [110] and [111] at the three top of the valence bands at Γ in k-space. The $m_{sp}^{*(\Gamma)}$ is almost identical along all directions due to isotropy of spin-orbit band.

Compound		$m_{hh}^{*(\Gamma)}$			$m_{lh}^{*(\Gamma)}$			$m_{sp}^{*(\Gamma)}$
		(001)	(110)	(111)	(001)	(110)	(111)	
Si	This work	0.312	0.609	0.750	0.229	0.169	0.161	0.271
	literature	0.346[a]	0.618[a]	0.732[a]	0.229[a]	0.171[a]	0.163[a]	0.234[b]
Ge	This work	0.251	0.467	0.623	0.060	0.053	0.052	0.128
	literature	0.254[a]	0.477[a]	0.390[a]	0.049[a]	0.056[a]	0.055[a]	0.097[b]
GaAs	This work	0.382	0.696	0.903	0.106	0.094	0.091	0.206
	literature	0.388[a], 0.35[d]	0.658[a]	0.920[a], 0.87[d]	0.089[a]	0.081[a]	0.079[a]	0.154[b], 0.133-0.388[c]
GaSb	This work	0.289	0.534	0.712	0.056	0.052	0.050	0.190
	literature	0.23[d]	-	0.57[d]	-	-	-	0.12-0.14[c]0.17[d]
InAs	This work	0.310	0.547	0.720	0.032	0.030	0.030	0.109
	literature	0.341[a], 0.39[d]	0.583[a], 0.98[d]	0.757[a]	0.042[a]	0.041[a]	0.014[a]	0.09-0.15[d]
InSb	This work	0.304	0.534	0.705	0.019	0.018	0.018	0.155
	literature	0.26[d]	-	0.68[d]	-	-	-	0.11[c], 0.2[d]
InP	This work	0.392	0.697	0.892	0.112	0.099	0.096	0.189
	literature	0.564[a], 0.415[e]	0.963[a]	1.220[a], 0.95[e]	0.173[a], 0.118[e]	0.148[a]	0.149[a]	0.121[b], 0.17-0.21[c], 0.19[d]

[a] From Ref. [29]
[b] From Ref. [57]
[c] From Ref. [87]
[d] From Ref. [47]
[e] From Ref. [32] and references therein.

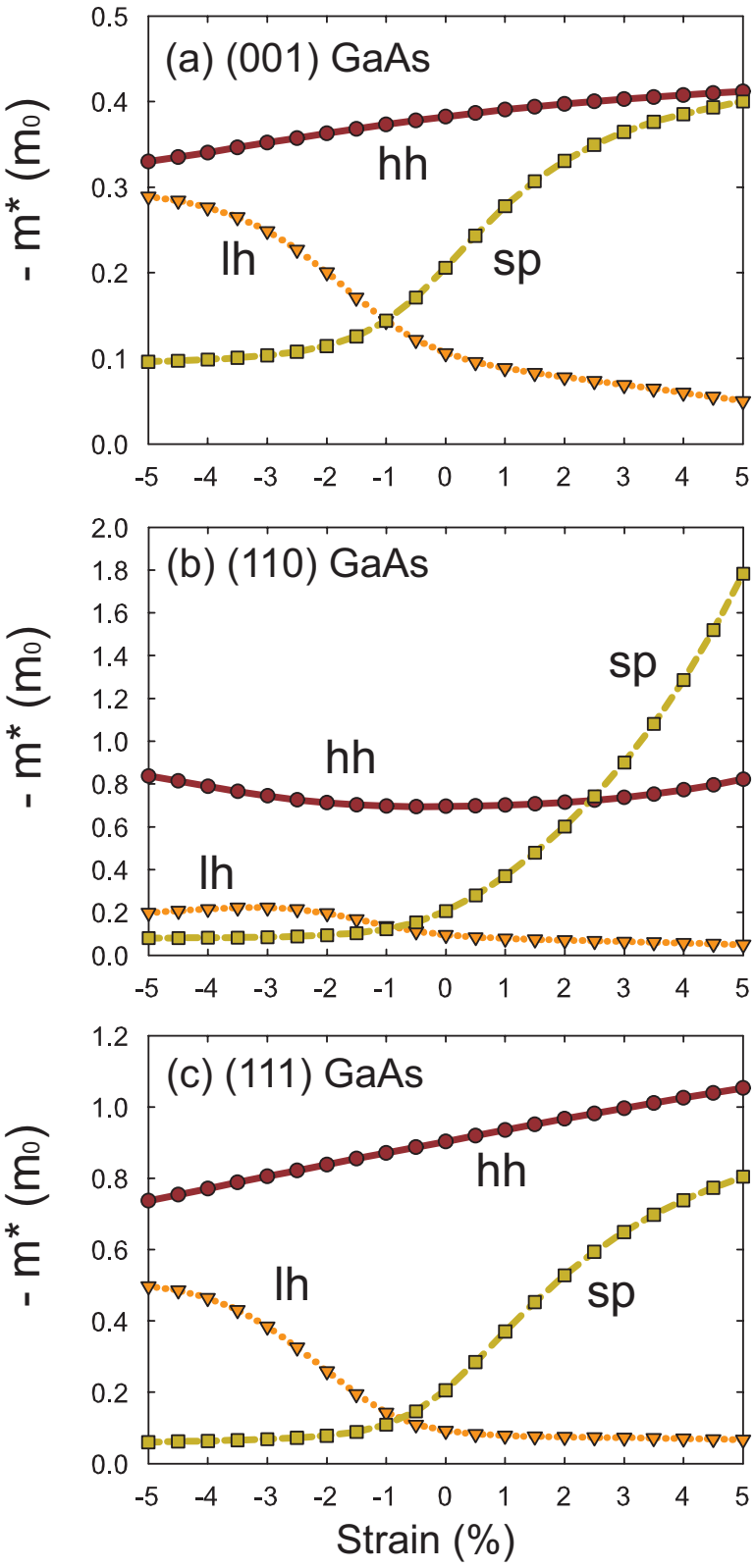

Figure 4.10. GaAs top of the valence band effective masses (in units of m_0) (heavy(hh) , light(lh) and split-off(sp) hole) at Γ as a function of biaxial strain on (001), (110) and (111) plane.

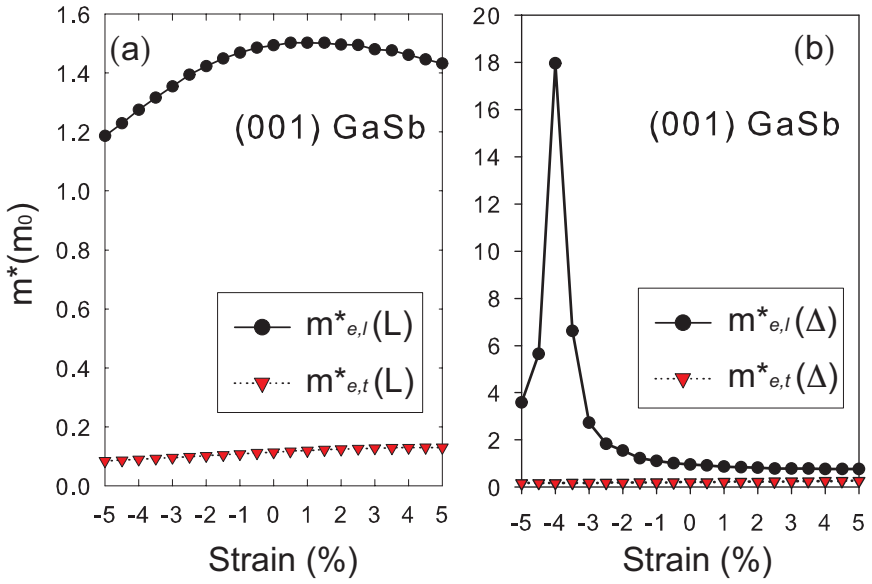

Figure 4.11. Longitudinal ($m^*_{e,l}$) and transverse ($m^*_{e,t}$) electron effective masses (in units of m_0) of GaSb at (a) L and (b) Δ minimum as a function of (001) biaxial strain in unit of m_0. A sudden variation of $m^*_l(\Delta)$ is caused by flatness of the dispersion near Δ minimum.

considered. A similar behavior is in other semiconductors except for compressively strained GaSb and InSb. Figure 4.11 shows $m^*_{e,l}$ and $m^*_{e,t}$ of GaSb at the symmetry points L and Δ as a function of (001) biaxial strain. Notice that $m^*_{e,l}(L)$ exhibits a larger variation than $m^*_{e,t}(L)$, resulting from the fact that the change of the constant-energy ellipsoid caused by strain along the longitudinal direction is larger than the change along the transverse direction at L. Also, $m^*_{e,l}(L)$ and $m^*_{e,t}(L)$ exhibit a continuous variation as a function of strain, but sudden changes appear in $m^*_{e,l}$ at the Δ minimum, resulting in a very large value of $m^*_{e,l}(\Delta)$. This is caused by the 'flatness' of the dispersion along the Δ line near the minimum where the denominator of Eq. 4.39 vanishes. Similar observations hold for the variation of $m^*_{e,l}(\Delta)$ as a function of strain in other semiconductors but the appearance of the peak is not an universal feature among semiconductors in this study.

We have also obtained the effective masses of III-V alloys from band structure results. The electron effective mass at Γ for relaxed $In_xGa_{1-x}As$ and $In_xGa_{1-x}Sb$ is

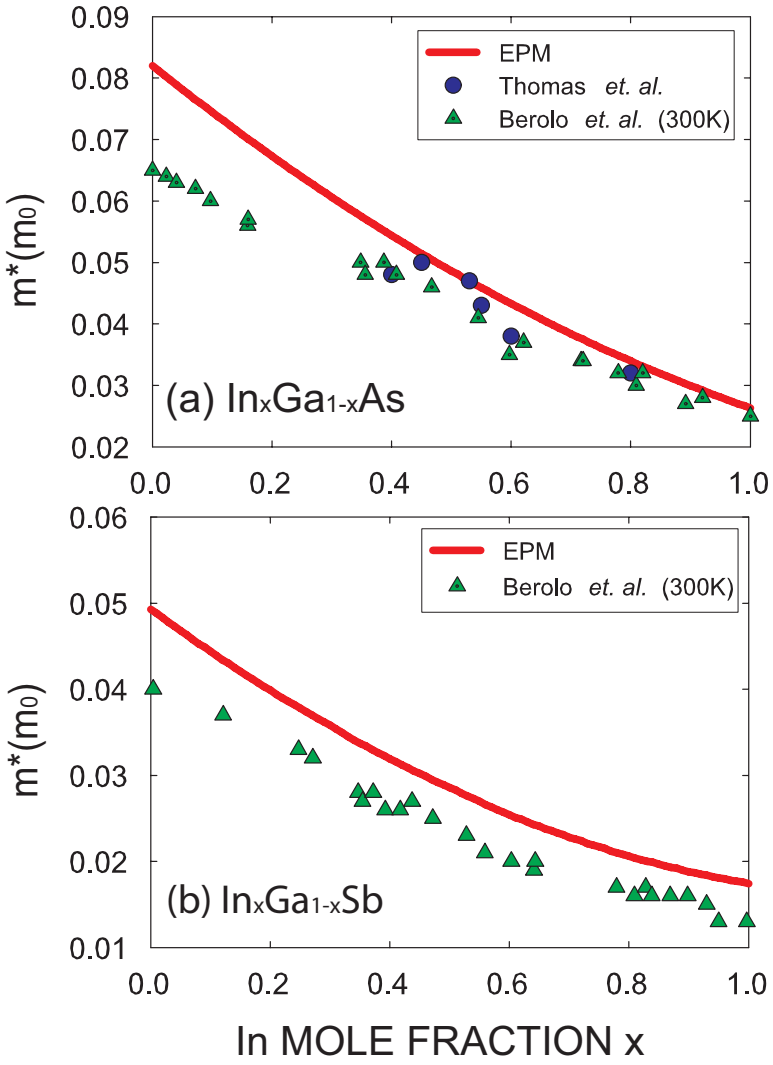

Figure 4.12. Electron effective mass (in units of m_0) at the bottom of the conduction band at Γ for relaxed (a) $In_xGa_{1-x}As$ and (b) $In_xGa_{1-x}As$ as a function of In mole fraction x where the 'EPM' (line) from this study is compared to Ref. [9] and references therein (symbols). The calculated data (EPM) show a discrepancy in absolute values due to the temperature dependence but exhibit a very similar bowing.

shown in Fig. 4.12. We see small differences our results ('EPM') and the experimental values reported by Berolo *et. al.* and references therein [9]. These differences would be negligible if we had considered the temperature dependence shown in Fig. 4.4. We can also observe a nonlinear variation (or bowing effect) of $m_e^{*(\Gamma)}$ as a function of In mole fraction x, variation which can be expressed by a quadratic dependence on x. From a least-square fit of the calculated data we have derived the following bowing equation for the effective mass $m_e^{*(\Gamma)}$ in relaxed $In_xGa_{1-x}As$:

$$m_e^{*(\Gamma)} = 0.082 - 0.078x + 0.022x^2 \tag{4.41}$$

and for relaxed $In_xGa_{1-x}Sb$,

$$m_e^{*(\Gamma)} = 0.049 - 0.051x + 0.019x^2 \tag{4.42}$$

where we show larger bowing effect compared to the Refs. [87, 9] in both cases.

We have also investigated the effect of strain on the effective masses of $In_xGa_{1-x}As$ and $In_xGa_{1-x}Sb$ alloys. In Fig. 4.13 we show the electron effective mass $m_e^{*(\Gamma)}$ of $In_xGa_{1-x}As$ (left) and $In_xGa_{1-x}Sb$ (right) on (001), (110) and (111) InP and InAs substrate, respectively, as a function of In mole fraction x. For $In_{0.53}Ga_{0.47}As$ (lattice matched to InP), $m_e^{*(\Gamma)}$ is isotropic, as expected. However, the 'transverse' and 'longitudinal' masses begin to deviate nonlinearly from the relaxed value $m_e^{*(\Gamma)}$ as the x varies. For $In_xGa_{1-x}As$ on (001) and (110) InP, $m_{e,t}^{*(\Gamma)}$ is larger than both $m_{e,l}^{*(\Gamma)}$ and the relaxed value $m_e^{*(\Gamma)}$ when the $In_xGa_{1-x}As$ is 'stretched' ($x < 0.53$). On the other hand, $m_{e,l}^{*(\Gamma)}$ becomes larger as $In_xGa_{1-x}As$ is compressively strained ($x > 0.53$). A larger value for $m_{e,l}^{*(\Gamma)}$ in compressively strained alloys is also seen in $In_xGa_{1-x}Sb$ on InAs over the entire range of x. The bowing equations of $m_{e,l}^{*(\Gamma)}$ and $m_{e,t}^{*(\Gamma)}$ are listed in Table 4.10, where we show separately the bahavior for tensile and compressive strain for $In_xGa_{1-x}As$ on InP. All bowing parameters appear to be positive with the

exception of $m_{e,l}^{*(\Gamma)}$ for $In_xGa_{1-x}As$ on (001) InP and $m_{e,l}^{*(\Gamma)}$ and $m_{e,t}^{*(\Gamma)}$ for $In_xGa_{1-x}Sb$ on (111) InAs.

The hole effectives masses have also been calculated for relaxed and strained $In_xGa_{1-x}As$ and $In_xGa_{1-x}Sb$ on InP and InAs, respectively. Figure 4.14 shows the nonlinear variation of $m_{hh}^{*(\Gamma)}$, $m_{lh}^{*(\Gamma)}$ and $m_{so}^{*(\Gamma)}$ as a function of In concentration x where the effective masses in relaxed and strained alloys are plotted as lines and symbols, respectively. Note that $m_{hh}^{*(\Gamma)}$ and $m_{so}^{*(\Gamma)}$ for strained $In_xGa_{1-x}As$ and $In_xGa_{1-x}Sb$ become smaller than their values in relaxed alloys as the alloys are compressively strained ($x > 0.53$ in $In_xGa_{1-x}As$ and $0 < x < 1$ in $In_xGa_{1-x}Sb$) along all interface orientations. Also, $m_{so}^{*(\Gamma)}$ is larger than $m_{lh}^{*(\Gamma)}$ in relaxed alloys but it becomes smaller as the alloys are compressively strained. In addition, the nonlinear variations of the hole effective masses are more significant in strained alloys than in relaxed alloys, resulting in larger bowing parameters. The bowing equations for the hole effective masses are listed in Table 4.11 for both relaxed and strained alloys. Note in Fig. 4.14 that the magnitude of the bowing parameter in strained alloys are larger than in relaxed alloys. The signs of the bowing parameters are positive for most of the cases but we do not see any clear trend for the sign (concave or convex) and magnitude of the bowing parameters. However, the signs of the bowing parameters in compressively strained alloys follow the behavior in relaxed alloys, except for $m_{lh}^{*(\Gamma)}$ in $In_xGa_{1-x}As$ on (110) InP.

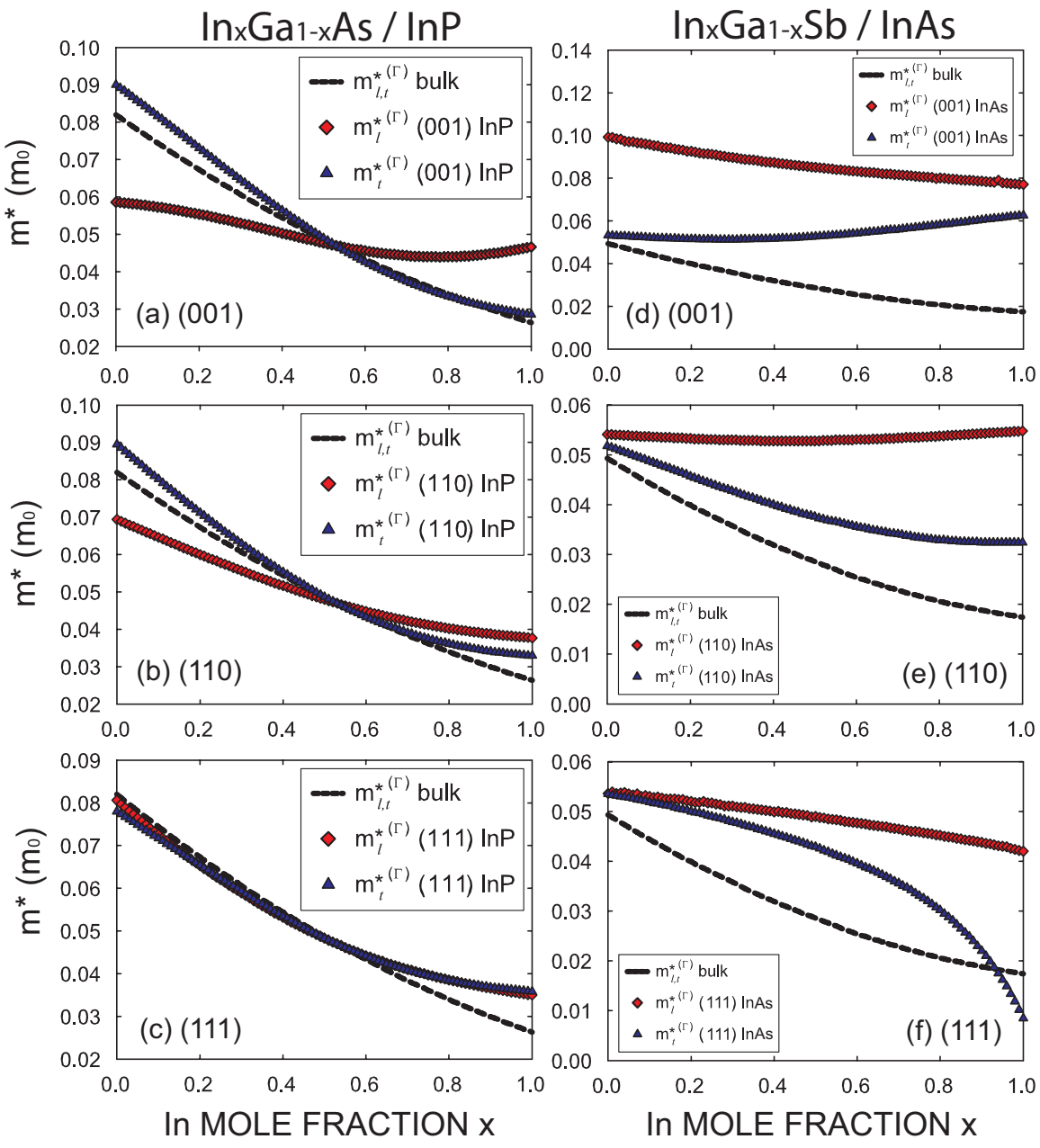

Figure 4.13. Longitudinal, $m_{e,l}^{*(\Gamma)}$, and transverse, $m_{e,t}^{*(\Gamma)}$, electron effective mass at the conduction band minimum (Γ) (in units of m_0) for relaxed (dashed lines) and strained alloys (symbols). The nonlinear variation of the electron effective mass is shown for different interface orientations (001), (110) and (111) of the substrate (InP for $In_xGa_{1-x}As$ ((a), (b) and (c)) and InAs for $In_xGa_{1-x}Sb$ ((d), (e) and (f))) as a function of In concentration x.

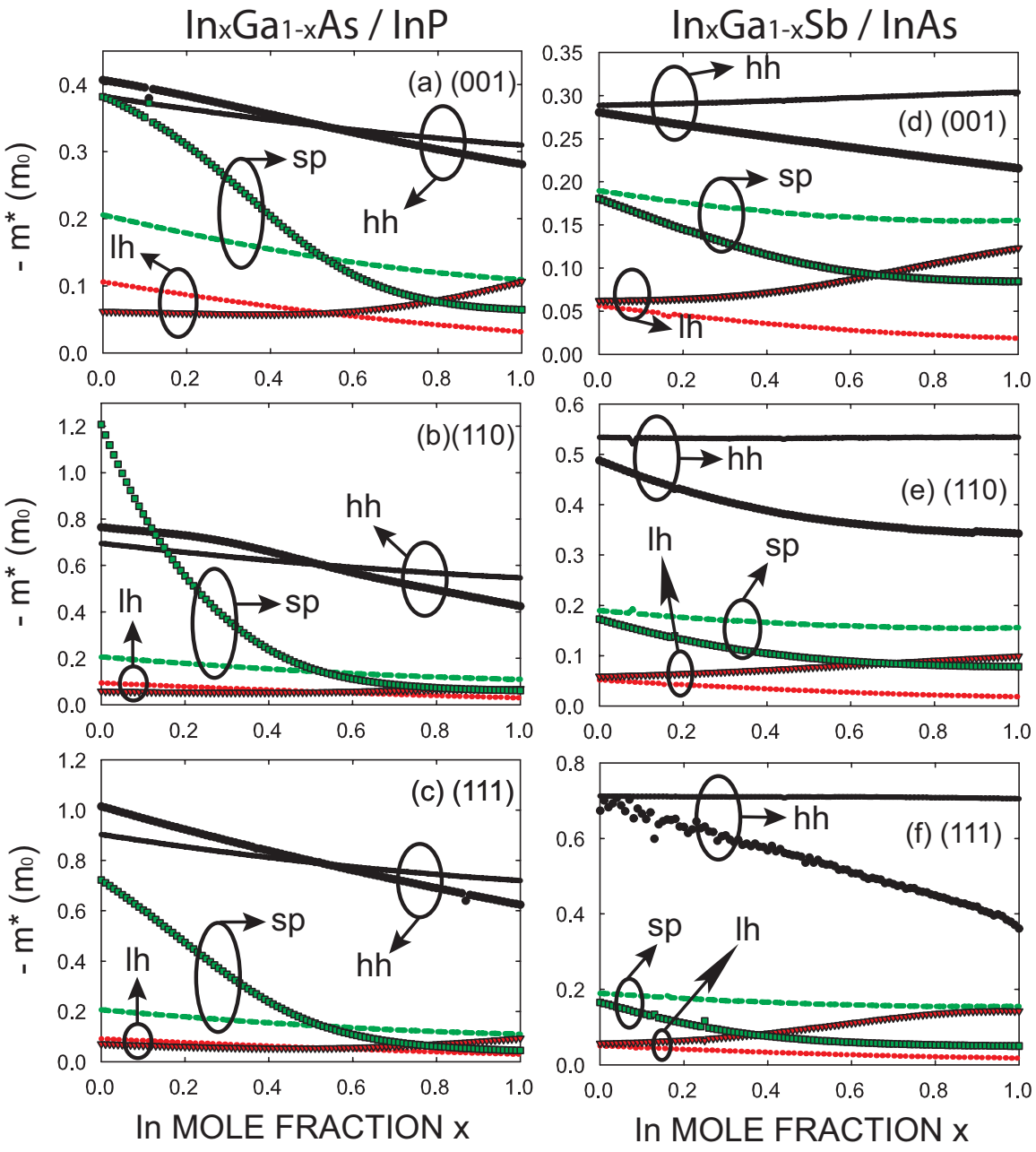

Figure 4.14. Valence-band effective masses (in units of m_0) (heavy (hh), light (lh) and split-off (so) hole) for relaxed (lines) and strained alloys (symbols) as a function of In mole fraction x. The nonlinear variation of the hole effective masses are shown for different orientations, (001), (110), and (111), of the substrates (InP for $In_xGa_{1-x}As$ ((a), (b) and (c)) and InAs for $In_xGa_{1-x}Sb$ ((d), (e) and (f))).

Table 4.10. The bowing equations of longitudinal ($m_{e,l}^{*(\Gamma)}$) and transverse ($m_{e,t}^{*(\Gamma)}$) electron effective masses (in units of m_0) at the bottom of the conduction band at Γ for strained $In_xGa_{1-x}As$ and $In_xGa_{1-x}Sb$ as a function of In concentration x. The $In_xGa_{1-x}As$ on InP is separated into $x < 0.53$ (tensile strain) and $x > 0.53$ (compressive strain)..

Compound	Orientation	Effective Mass	
		$m_{e,l}^{*(\Gamma)}$	$m_{e,t}^{*(\Gamma)}$
$In_xGa_{1-x}As/InP$	(001)	$0.059 - 0.015x - 0.016x^2$	$0.090 - 0.090x + 0.013x^2$
($x < 0.53$: tensile)	(110)	$0.070 - 0.050x + 0.014x^2$	$0.090 - 0.100x + 0.036x^2$
	(111)	$0.081 - 0.084x + 0.039x^2$	$0.078 - 0.068x + 0.015x^2$
$In_xGa_{1-x}As/InP$	(001)	$0.075 - 0.080x + 0.052x^2$	$0.097 - 0.123x + 0.055x^2$
($x > 0.53$: compressive)	(110)	$0.071 - 0.060x + 0.026x^2$	$0.090 - 0.110x + 0.052x^2$
	(111)	$0.076 - 0.070x + 0.029x^2$	$0.080 - 0.085x + 0.040x^2$
$In_xGa_{1-x}Sb/InAs$	(001)	$0.099 - 0.034x + 0.013x^2$	$0.053 - 0.011x + 0.021x^2$
(compressive)	(110)	$0.054 - 0.006x + 0.007x^2$	$0.053 - 0.039x + 0.018x^2$
	(111)	$0.054 - 0.008x - 0.003x^2$	$0.051 + 0.005x - 0.043x^2$

Table 4.11. The hole effective mass bowing equations for bulk and strained $In_xGa_{1-x}As$ and $In_xGa_{1-x}Sb$ (in units of m_0) as a function of In concentration x. The $In_xGa_{1-x}As$ on InP is separated into $x < 0.53$ (tensile strain) and $x > 0.53$ (compressive strain).

Compound	Orientation	Effective Mass		
		$m_{hh}^{*(\Gamma)}$	$m_{lh}^{*(\Gamma)}$	$m_{sp}^{*(\Gamma)}$
Bulk $In_xGa_{1-x}As$	(001)	$0.038 - 0.098x + 0.025x^2$	$0.106 - 0.103x + 0.028x^2$	
	(110)	$0.696 - 0.207x + 0.058x^2$	$0.094 - 0.085x + 0.020x^2$	$0.206 - 0.151x + 0.054x^2$
	(111)	$0.903 - 0.259x + 0.075x^2$	$0.091 - 0.081x + 0.019x^2$	
Bulk $In_xGa_{1-x}Sb$	(001)	$0.288 + 0.013x + 0.004x^2$	$0.056 - 0.061x + 0.023x^2$	
	(110)	$0.532 - 0.002x + 0.005x^2$	$0.052 - 0.052x + 0.019x^2$	$0.190 - 0.079x + 0.044x^2$
	(111)	$0.711 + 0.0004x - 0.005x^2$	$0.050 - 0.050x + 0.018x^2$	
$In_xGa_{1-x}As$/InP	(001)	$0.407 - 0.115x - 0.031x^2$	$0.062 - 0.022x + 0.030x^2$	$0.388 - 0.354x - 0.242x^2$
($x < 0.53$: tensile)	(110)	$0.762 - 0.075x - 0.439x^2$	$0.059 - 0.035x + 0.052x^2$	$1.177 - 3.768x + 3.496x^2$
	(111)	$1.015 - 0.479x + 0.094x^2$	$0.071 - 0.072x + 0.074x^2$	$0.737 - 1.465x + 0.591x^2$
$In_xGa_{1-x}As$/InP	(001)	$0.419 - 0.172x + 0.034x^2$	$0.085 - 0.127x + 0.149x^2$	$0.428 - 0.755x + 0.394x^2$
($x > 0.53$: compressive)	(110)	$0.844 - 0.519x + 0.101x^2$	$0.020 + 0.083x - 0.034x^2$	$0.433 - 0.780x + 0.413x^2$
	(111)	$1.017 - 0.474x + 0.081x^2$	$0.073 - 0.100x + 0.120x^2$	$0.479 - 0.893x + 0.462x^2$
$In_xGa_{1-x}Sb$/InAs	(001)	$0.280 - 0.072x + 0.008x^2$	$0.061 + 0.006x + 0.059x^2$	$0.182 - 0.212x + 0.115x^2$
(compressive)	(110)	$0.485 - 0.305x + 0.167x^2$	$0.058 + 0.032x + 0.010x^2$	$0.170 - 0.208x + 0.120x^2$
	(111)	$0.692 - 0.283x - 0.031x^2$	$0.050 + 0.087x + 0.017x^2$	$0.161 - 0.273x + 0.168x^2$

CHAPTER 5

PSEUDOPOTENTIAL WITH SUPERCELL METHOD

5.1 Supercell Method

In dealing with non-periodic structures, such as homo- or hetero-layers, nanowires or quantum dots, it is customary to build a larger cell – thus abandoning the primitive two-ion Wigner-Seitz cell of diamond or zinc-blende crystals [18], for example – retaining the primitive periodicity in two directions (*e.g.*, the plane of thin-layers) or in one direction (*e.g.*, the axial direction of nanowires) – but artificially introducing periodicity in the other direction(s) by repeating the structure employing translation vectors large enough to span the entire structure (*e.g.*, the thickness of the thin film plus 'vacuum padding' to ensure isolation of each film; the cross-section of a nanowire with a similar vacuum padding). This is so called supercell structure as shown in Fig. 5.1 and the artificial periodicity comes with the advantage of allowing the use of plane-wave expansions, but the number of plane-waves required obviously grows with the growing size of the supercell. This determines the rank n of the single-electron Hamiltonian matrix H of rank n. Explicitly building and storing this $n \times n$ dense matrix requires n^2 matrix-vector operations and large memory spaces in solving the associated eigenvalue problem. In this work we have employed conventional scalar numerical algorithm, thus limiting our study to small systems with up to, for example, $\sim$250 of atoms for Si nanowire, corresponding to a rank $n \sim 15,000$. This requires about 2 CPU hours in order to obtain the ~ 700 lowest-energy eigenpairs at a single k-point in our IBM POWER6 workstation using the IBM Engineering and Scientific Subroutine Library (ESSL). The study of larger system, already routine practice,

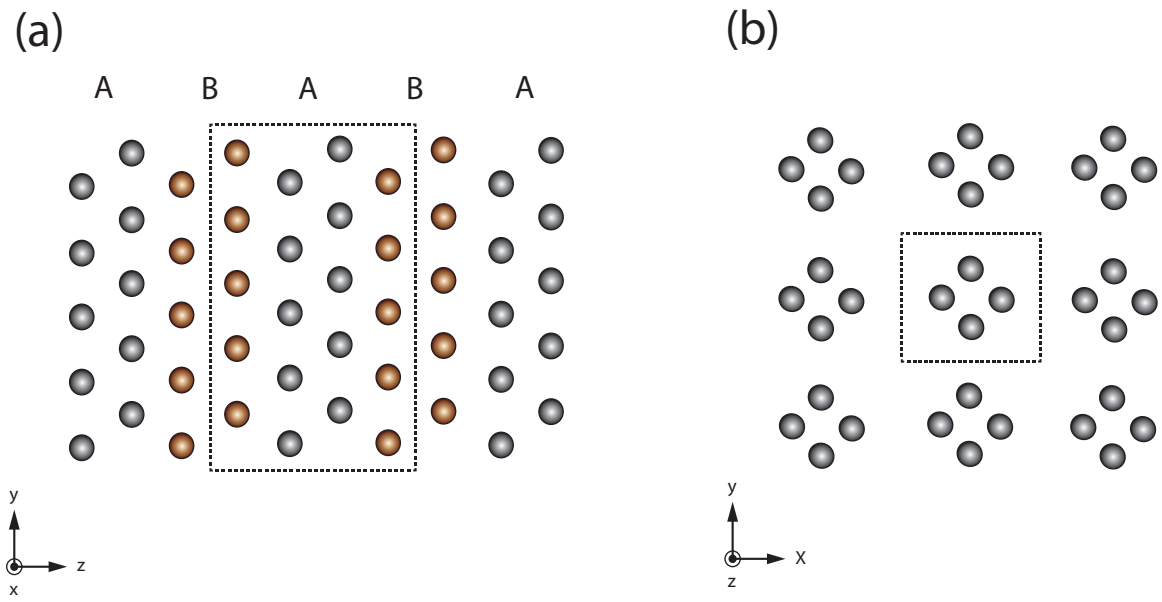

Figure 5.1. Schematic of (a) 1D supercell for the case of zinc-blende thin-layer structure where the hetero-layer is artificially periodic along the z-direction, and (b) 2D supercell for the case of nanowire where the wire is artificially periodic along (x,y)-plane. The dotted box represent the choice the supercell where vacuum cells can be placed to insulate adjacent layers or wires.

requires the use of highly efficient, robust, accurate and scalable algorithms with parallelized eigenvalue solvers such as the FEAST algorithm [69] or the folded spectrum method (FSM) implemented in Parallel Energy SCAN (PESCAN) code [89, 14, 90].

5.2 Transferability of Local Empirical Pseudopotential

As we discussed in Chap. 4, the full Fourier transform of the atomic pseudopotential, $V(q)$, is required when we extend the EPM to strained or confined systems and this is usually obtained by interpolating among form factors which reproduce experimental band gaps at high symmetry points, effective masses, and correct work function in confined systems. Clearly, once a form particular for $V(q)$ is determined in order to reproduce the properties of a particular structure, the main problem – related to the 'predictive power' mentioned above – is to assess how the pseudopotential changes as the compositional or geometric (or both) characteristics of the

structure change. In principle, the pseudopotential should change, since, for example, the pseudopotential of atom C in the binary compound AC must reflect the bonding and valence-charge distribution of that compound. Thus, the pseudopotential of the same atom C in the compound BC should be expected to be different. As we shall see below, despite these considerations, often the empirical pseudopotentials are 'portable' (or 'transferable') to a large extent, thus allowing some predictions power, which are nevertheless to be taken with a grain of salt. Finally, regarding structures confined by vacuum or heterostructures, it is imperative to calibrate correctly the workfunctions and band-alignment. As discussed by Mäder *et al.* [59, 10], these properties are determined by the value of $V(q)$ at $q = 0$, so that by empirically modifying the low-q behavior of the pseudopotential one can obtain the correct workfunction. In the following, we will compare the results of our calculations to results – when available – obtained using self-consistent first-principles calculations in order to assess how strongly our pseudopitentials may be affected by these 'portability' problems. Several forms are available from the literature. One such notable form, as an example, for the local Si pseudopotential, calibrated when ignoring the spin-orbit interaction, has been obtained by Zhang *et al.* [99] This parametrized form of $V(q)$ yields the correct value of the workfunction and of the energy gaps of the bulk band structure at high symmetry points. A parametrized form for the pseudopotentials of H has been similarly obtained by Wang *et al.* [89] by fitting the surface local density of states of primary surfaces to the experimental data. Previously in Chap. 4, we have employed a cubic spline interpolation for $V(q)$ with a fast cutoff term at large $q(> 3k_F)$ for bulk semiconductors with nonlocal and spin-orbit corrections calibrated to reproduce experimental band gaps at various high symmetry points, the electron and hole effective masses, and valence- and conduction-band deformation potentials. As an another constraint, we had also fitted the $q = 0$ value (namely, $V(q = 0) =$ -1.113 Ry for Si) to the value from Ref. [89], thus reproducing correct workfunction.

CHAPTER 6

BAND STRUCTURES FOR 1D SUPERCELL

As discussed in the previous chapter, transferability of the local empirical pseudopotential enables us to calculate the band structure of confined systems with supercell method. In this chapter, we describe our choice of the supercell and atomic positions in the cell for the different surface orientations (001), (110) and (111) of one dimensionally confined system, *e.g.* 1D supercell, which is employed to calculate the band structure of Si thin- and Si/$Si_{1-x}Ge_x$/Si hetero-layers. The layer structures are assumed to be free-standing and its surfaces are hydrogen passivated. Also, strain dependence of the band structure of layer structures are investigated with uniform biaxial strain along the plane directions.

6.1 Crystal Structure in 1D Supercell : Thin-Layer

6.1.1 (001) Interface

On (001) interface, we can choose the real space primitive translation vectors for the supercell as,

$$\vec{a_1} = \frac{1}{2}a_0(1+\epsilon_{\parallel})(\hat{x}+\hat{y}), \quad \vec{a_2} = \frac{1}{2}a_0(1+\epsilon_{\parallel})(-\hat{x}+\hat{y}), \quad \vec{a_3} = a_0 N_t(1+\epsilon_{\perp})\hat{z} \quad (6.1)$$

where $a_0 = 0.543$ nm is the Si lattice constant and $\epsilon_{\parallel}$ and $\epsilon_{\perp}$ denote the value of the strain on the (x, y)-plane (*i.e.*, in-plane biaxial strain) and along the z-direction (*i.e.*, out-of-plane uniaxial strain), respectively, and the linear relations between $\epsilon_{\parallel}$ and $\epsilon_{\perp}$ are given in Eq. 2.39. The $N_t = N + N_v$ is an integer number and the N and N_v

each represent the number of Si unit cells in the supercell and the number of vacuum cells used to insulate repeated Si layers along the z-direction, respectively. For (001) interface, four Si atoms are enough to construct the Si unit cell in which we can place the Si atoms in the first unit cell at,

$$\begin{aligned}
\vec{\tau}_1 &= 0 \\
\vec{\tau}_2 &= \frac{1}{4}a_0(\hat{x}+\hat{y}+\hat{z}) \\
\vec{\tau}_3 &= \frac{1}{4}a_0(2\hat{y}+2\hat{z}) \\
\vec{\tau}_4 &= \frac{1}{4}a_0(-\hat{x}+\hat{y}+3\hat{z})
\end{aligned} \tag{6.2}$$

then the Si unit cell is repeated N times along the z-direction which is equivalent to [001] direction in this case. The positions of Si atoms in the repeated unit cell can be proceeded as,

$$\begin{aligned}
\vec{\tau}_{4(j-1)+1} &= \vec{\tau}_1 + (j-1)a_0\hat{z} \\
\vec{\tau}_{4(j-1)+2} &= \vec{\tau}_2 + (j-1)a_0\hat{z} \\
\vec{\tau}_{4(j-1)+3} &= \vec{\tau}_3 + (j-1)a_0\hat{z} \\
\vec{\tau}_{4(j-1)+4} &= \vec{\tau}_4 + (j-1)a_0\hat{z}
\end{aligned} \tag{6.3}$$

where the subscript of $\vec{\tau}$ represent label of each Si atom and the index j runs from 2 to N. The dangling bonds of Si atoms at both surfaces (top and bottom along the z-direction) of the layer are terminated with four hydrogen (H) atoms at the following positions,

$$
\begin{aligned}
\vec{\tau}_{H,1} &= \vec{\tau}_1 + 0.158a_0(-\hat{x} + \hat{y} - \hat{z}) \\
\vec{\tau}_{H,2} &= \vec{\tau}_1 + 0.158a_0(\hat{x} - \hat{y} - \hat{z}) \\
\vec{\tau}_{H,3} &= \vec{\tau}_{4N} + 0.158a_0(-\hat{x} + \hat{y} + \hat{z}) \\
\vec{\tau}_{H,4} &= \vec{\tau}_{4N} + 0.158a_0(\hat{x} - \hat{y} + \hat{z})
\end{aligned} \tag{6.4}
$$

where the Si-H boding length is taken to be $d = 0.2738a_0$ and the bonding angle is taken to be the same as Si-Si bonding which is $\theta = 109.47°$ [89] without surface reconstruction. Then,the total number of atoms in the supercell would be $4N_{Si} + 4_H$. Additional displacement of the each atom due to the strain is taken into account using Eq. 4.13.

6.1.2 (110) Interface

For (110) interface, we choose the real space primitive translation vectors for the supercell as,

$$
\vec{a_1} = \frac{\sqrt{2}}{2}a_0(1 + \epsilon_{\parallel})\hat{x}, \quad \vec{a_2} = a_0(1 + \epsilon_{\parallel})\hat{y}, \quad \vec{a_3} = \frac{\sqrt{2}}{2}a_0 N_t(1 + \epsilon_{\perp})\hat{z} \tag{6.5}
$$

As well as (001) interface layer, we need only four Si atoms in the unit cell located at,

$$
\begin{aligned}
\vec{\tau}_1 &= 0 \\
\vec{\tau}_2 &= \frac{1}{4}a_0(\hat{y} + \sqrt{2}\hat{z}) \\
\vec{\tau}_3 &= \frac{1}{4}a_0(\sqrt{2}\hat{x} + 2\hat{y} + \sqrt{2}\hat{z}) \\
\vec{\tau}_4 &= \frac{1}{4}a_0(\sqrt{2}\hat{x} + 3\hat{y})
\end{aligned} \tag{6.6}
$$

then the positions of atoms in the repeated cells along the z-direction equivalent to [110] are,

$$
\begin{aligned}
\vec{\tau}_{4(j-1)+1} &= \vec{\tau}_1 + \frac{\sqrt{2}}{2}(j-1)a_0\hat{z} \\
\vec{\tau}_{4(j-1)+2} &= \vec{\tau}_2 + \frac{\sqrt{2}}{2}(j-1)a_0\hat{z} \\
\vec{\tau}_{4(j-1)+3} &= \vec{\tau}_3 + \frac{\sqrt{2}}{2}(j-1)a_0\hat{z} \\
\vec{\tau}_{4(j-1)+4} &= \vec{\tau}_4 + \frac{\sqrt{2}}{2}(j-1)a_0\hat{z}
\end{aligned} \tag{6.7}
$$

The Si dangling bonds also can terminated with four H atoms as same as the case of (001) interface using Eq. 6.4.

6.1.3 (111) Interface

In the case of (111) interface, we choose the real space primitive translation vectors for the supercell as,

$$
\vec{a_1} = \frac{\sqrt{2}}{2}a_0(1+\epsilon_\parallel)\hat{x}, \quad \vec{a_2} = \frac{1}{2}a_0(1+\epsilon_\parallel)\left(\frac{1}{\sqrt{2}}\hat{x} + \sqrt{\frac{3}{2}}\hat{y}\right), \quad \vec{a_3} = \sqrt{3}a_0N_t(1+\epsilon_\perp)\hat{z} \tag{6.8}
$$

However, the number of atoms needed in the unit cell for (111) interface is six instead of four in the cases of (001) and (110). The atomic positions of Si atoms in the first unit cell is then,

$$
\begin{aligned}
\vec{\tau}_1 &= \frac{\sqrt{2}}{4}a_0\hat{x} \\
\vec{\tau}_2 &= a_0\left[\frac{\sqrt{2}}{4}\hat{x} + \frac{1}{\sqrt{6}}\hat{y} + \left(\frac{1}{\sqrt{3}} - \frac{\sqrt{3}}{4}\right)\hat{z}\right] \\
\vec{\tau}_3 &= a_0\left[\frac{\sqrt{2}}{4}\hat{x} + \frac{1}{\sqrt{6}}\hat{y} + \frac{1}{\sqrt{3}}\hat{z}\right] \\
\vec{\tau}_4 &= a_0\left[\frac{1}{\sqrt{2}}\hat{x} + \frac{1}{2\sqrt{6}}\hat{y} + \left(\frac{2}{\sqrt{3}} - \frac{\sqrt{3}}{4}\right)\hat{z}\right] \\
\vec{\tau}_5 &= a_0\left[\frac{1}{\sqrt{2}}\hat{x} + \frac{1}{2\sqrt{6}}\hat{y} + \frac{2}{\sqrt{3}}\hat{z}\right] \\
\vec{\tau}_6 &= a_0\left[\frac{1}{\sqrt{2}}\hat{x} + \frac{\sqrt{3}}{2\sqrt{2}}\hat{y} + \left(\frac{3}{\sqrt{3}} - \frac{\sqrt{3}}{4}\right)\hat{z}\right]
\end{aligned} \tag{6.9}
$$

and the positions of atoms in the repeated cells can be obtained by translating above by an amount $\sqrt{3}(j-1)a_0$ (j=2,N) along the z-direction equivalent to [111]. The number of H atoms needed to terminate the dangling bonds are two in this case instead of four in the case of (001) and (111) which are located at,

$$\begin{aligned} \vec{\tau}_{H,1} &= \vec{\tau}_1 - 0.2738a_0\hat{z} \\ \vec{\tau}_{H,2} &= \vec{\tau}_{6N} + 0.2738a_0\hat{z} \end{aligned} \tag{6.10}$$

6.2 Band Structure of Strained Si Thin-Layers

Figure 6.1 shows the band structure of 9 cells of free-standing Si thin layer with 2 cells of vacuum in 2D BZ using local pseudopotentials for Si and hydrogen from Zunger's group [99, 89] without nonlocal and spin-orbit corrections. The surface Si dandling bonds are passivated by hydrogen atoms. The band gap of (001) layer shows direct gap at the center of the BZ, Γ, while (110) and (111) layers have indirect band gap near the $\overline{X}$ which can be explained by well-known affect of zone folding [77]. Layer thickness dependence of the band gap is shown in Fig. 6.2 where the direct and indirect gap are represented as 'filled' and 'empty' symbols, respectively. As can be seen, the nature of the band gap in (001) and (111) layers does not change as a function of the layer thickness while direct-to-indirect band gap transition occurs in (110) layers as the layer thickness increases. The band gap decreases nonlinearly as the layer thickness increases which is due to a quantum confinement effect. Also, there is different band gap ordering depending on the layer thickness. The band gap in (001) layer is the largest while the gap in (110) layer is the smallest at a small layer thickness ($<$ 2nm). But the order is changed as the layer thickness increases. Strain effect of the band gap is also investigated at a given layer thickness. Figure 6.3 shows the band gap of different surface orientations of Si layers with thickness $\sim$ 3nm as a function of biaxial strain along the layer surface ((x,y) plane). In all surface

orientations, the band gap nonlinearly decreases as amount of strain increases except 1% compressively strained (001) layer and the band gap variation with strain is the most sensitive in (110) layer. It is worth noting that we show the direct-to-indirect band gap transition in the (001) layer at 2% compressive strain while the nature of the band gap remains indirect in (111) layer. However, there is unexpected direct-to-indirect gap transition occurs at 4% compressive strain in (110) layer which needs further study.

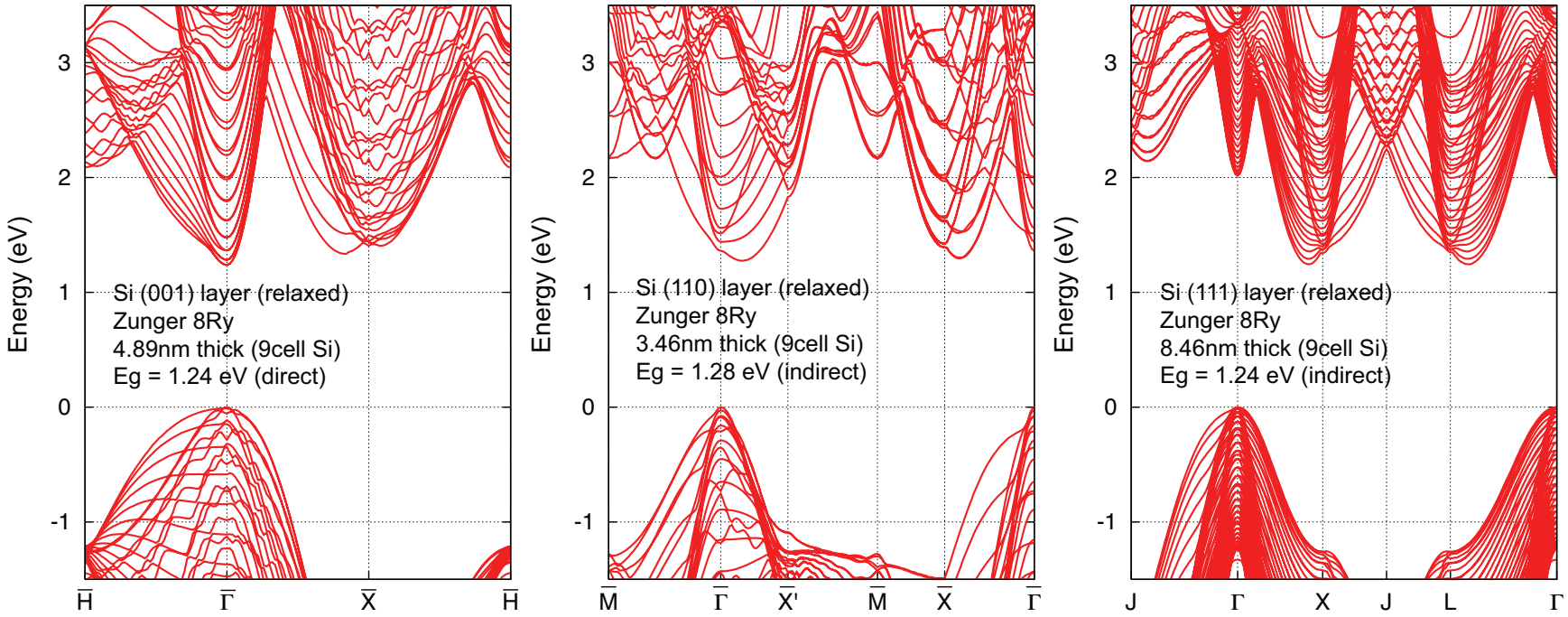

Figure 6.1. Band structure of different crystal orientation, relaxed, free-standing 9 cells of Si with 2 vacuum cells thin-layer in 2D BZ.

6.3 Band Structure of $Si/Si_{1-x}Ge_x/Si$ Hetero-Layers

In this section, we calculate the band structure of free standing $Si/Si_{1-x}Ge_x/Si$ hetero-layer mimicking the structure recently investigated by Gomez *et al.* [37] in which they studied the hole mobility characteristics of asymmetrically strained-SiGe p-MOSFETs. Gomez *et al.* showed an enhanced hole mobility in biaxial compressive strained SiGe relative to relaxed Si and also they showed that the mobility is further increased by $< 110 >$ longitudinal uniaxial compressive strain. Figure 6.4 (a) shows the device structure investigated by Gomez *et al.* and (b) shows the $Si/Si_{1-x}Ge_x/Si$ hetero-layer mimicking the device (a) where the '4 cells of $Si_{1-x}Ge_x$' layer is biaxially strained depending the Ge concentration x due to the lattice mismatch with relaxed Si substrate which is not explicitly included in the supercell. Surface Si dangling bonds are passivated by hydrogen atoms as well.

A major problem that we have to face in calculating the band structure of hetero-layer is how we can obtain the correct band discontinuity between Si and $Si_{1-x}Ge_x$ layers since there is no absolute energy scale for bulk semiconductors in EPM to which all energies can be referred because of the long range Coulomb interaction, zero of energy is undefined for an bulk crystal [85]. According to Van de Walle *et al.*, one has to carry out self-consistent calculation in which the electrons are allowed to redistribute to the specific environment around the interface to obtain full picture of the interface problem in which electron distribution is different from the bulk near the interface [85].

In this study, instead of self-consistent calculation, we empirically adjust the $q = 0$ of $V(q)$ to obtain correct band alignment between Si and $Si_{1-x}Ge_x$. For $Si/Si_{1-x}Ge_x/Si$ hetero-layer, we use the local pseudopotential for Si and Ge in Table. 4.3 with nonlocal correction rather than using Zunger's group local only pseudopotential employed for Si-thin layer band structure calculation in the previous section. We retain the $V(q = 0)$ for Si as shown in Table. 4.3 but the $V(q = 0)$ for

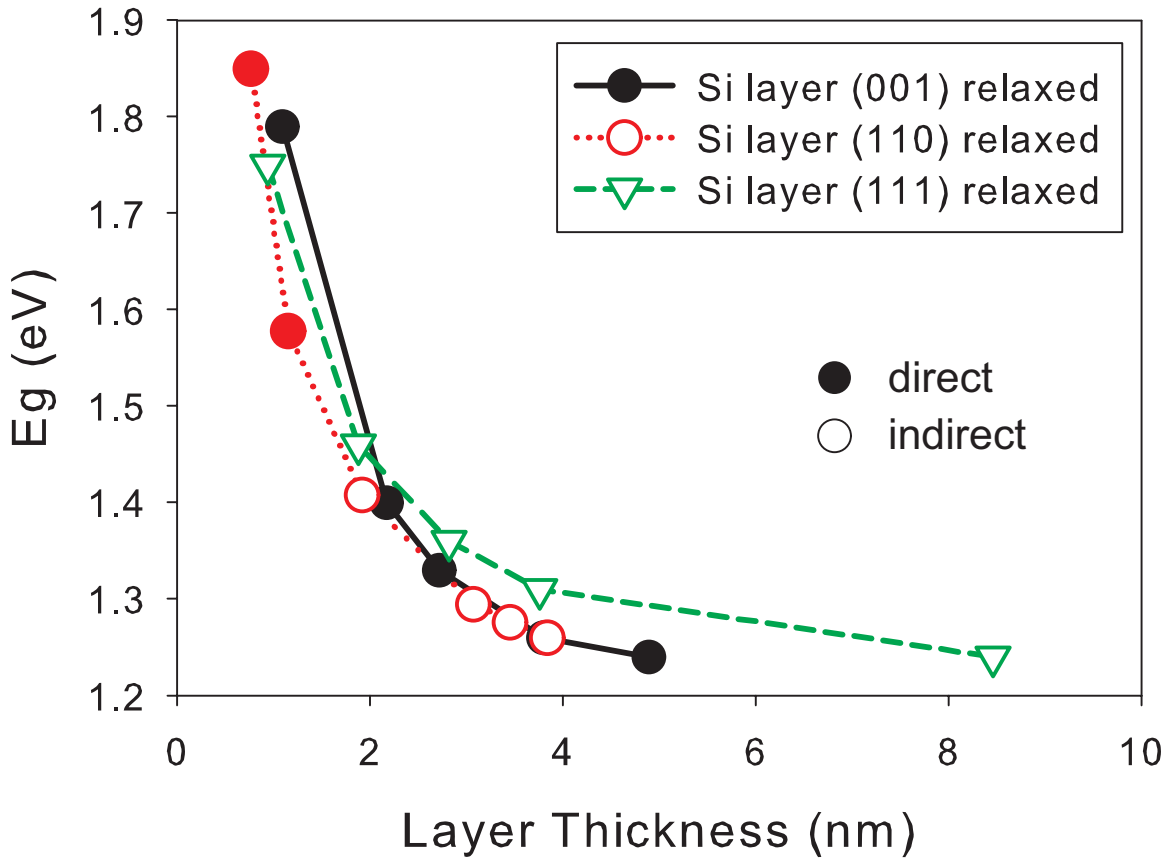

Figure 6.2. Band gap of different surface orientations of relaxed Si thin-layers as a function of layer thickness. The 'filled' symbols and 'empty' symbols represent direct and indirect band gap, respectively.

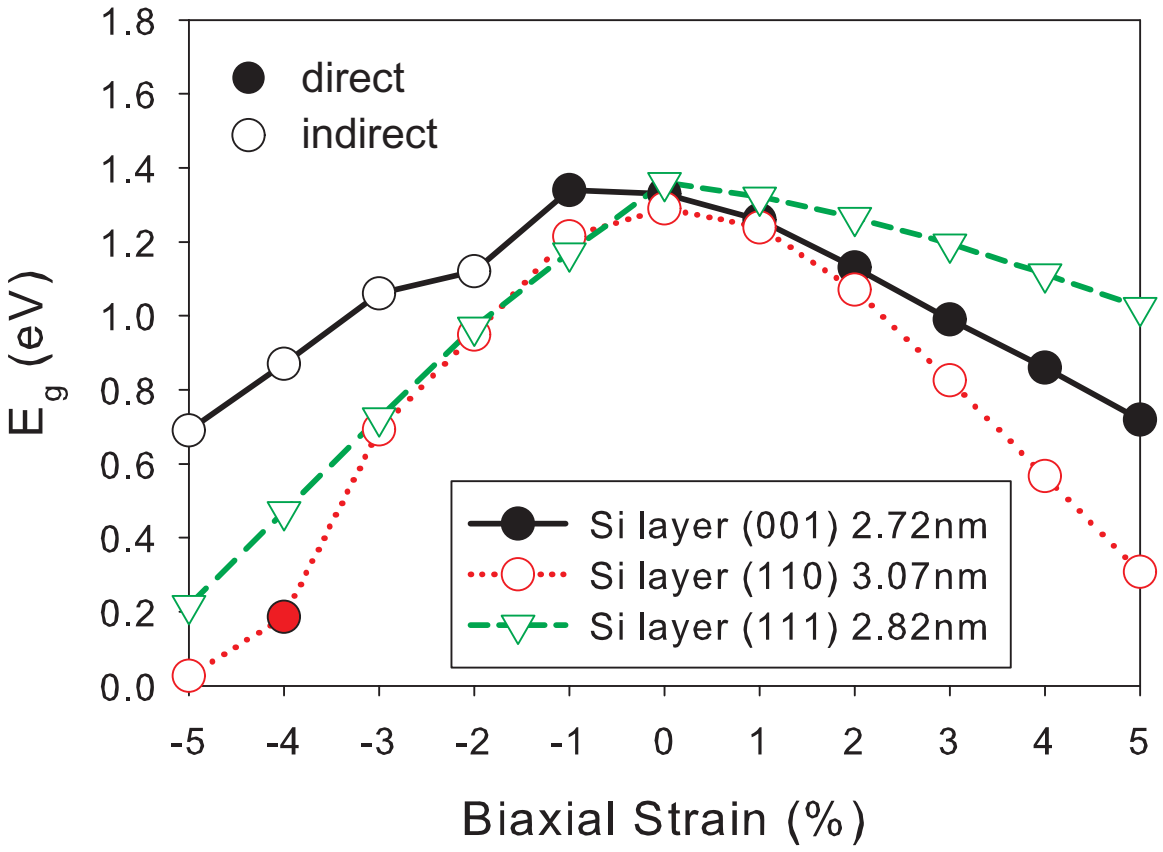

Figure 6.3. Band gap of different surface orientations of Si ∼3nm thickness thin-layers as a function of biaxial strain along the surface where the negative and positive strain indicate compressive and tensile strain, respectively. The 'filled' symbols and 'empty' symbols represent direct and indirect band gap, respectively.

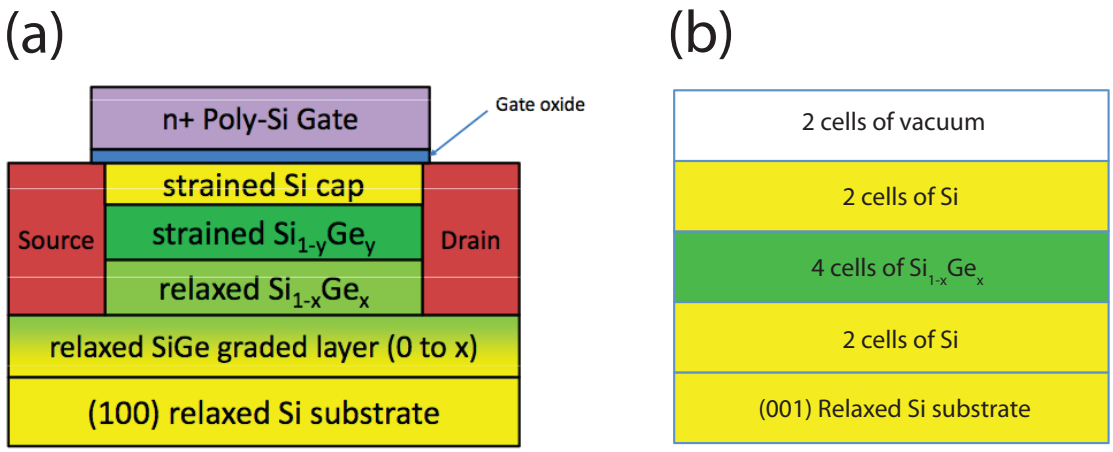

Figure 6.4. (a) Device structure of biaxially strained SiGe p-MOSFET in Ref. [37]. (b) Free standing $Si/Si_{1-x}Ge_x/Si$ hetero-layer mimicking the device structure (a) using supercell method. Amount of in-plane (biaxial) strain on '4 cells of $Si_{1-x}Ge_x$' layer (colored in 'green') is controlled by Ge concentration x and '2 cell of Si' layers (colored in 'yellow') are relaxed. Two vacuum cells (colored in 'white') are added on the top of the '2 cell of Si' layers which is enough to isolate the repeating layers but the Si substrate is not explicitly included in the supercell structure. Si dangling bonds at the top and bottom '2 cell of Si' layers are passivated by hydrogen.

Ge is slightly re-adjusted to $V(q = 0) = -0.980$ Ry. Figure 6.5 shows the squared amplitude of the wave functions along the z-direction of three lowest energy conduction and highest valence band states in the (001) Si (2 cells)/$Si_{0.53}Ge_{0.43}$ (4 cells)/Si (2cells) hetero-layer along with band alignment diagram where $Si_{0.53}Ge_{0.43}$ layer is compressively strained due to the lattice mismatch and the surface Si dangling bonds are hydrogen terminated. As seen, the wave functions of conduction bands are confined in Si layers and of valence bands are confined in $Si_{0.53}Ge_{0.47}$ layer ensuring us that the band alignment between Si and $Si_{0.53}Ge_{0.47}$ layers are well calibrated. Then we calculate the 2D band structure of the $Si/Si_{0.53}Ge_{0.43}/Si$ hetero-layer as shown in Fig. 6.6 together with energy dispersion along the k_z direction perpendicular to the interface at the $\overline{\Gamma}$ in 2D BZ. Note that the there is no variation of the energy dispersion along the k_z direction up the energy of about 3 eV since the energy dispersion is expected to be two-dimensional at low energies. However, the dispersion begin

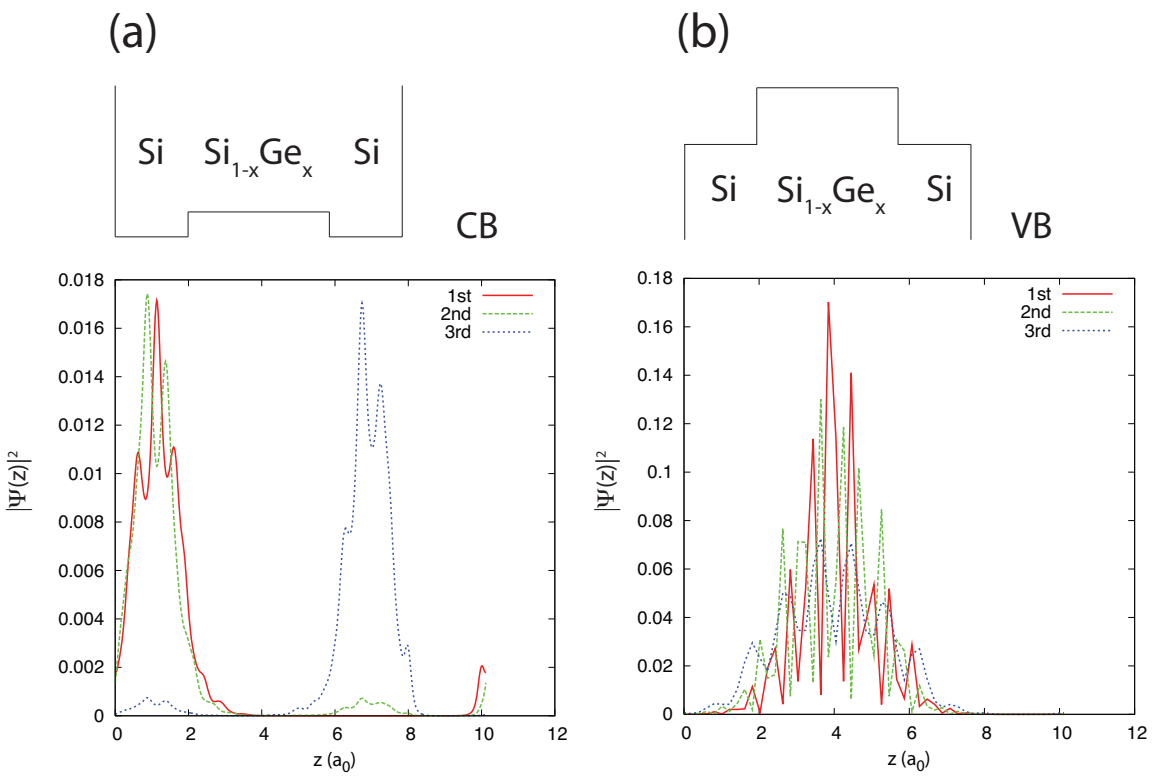

Figure 6.5. Squared amplitude - averaged over a supercell along (x,y) plane - of the wave functions as a function of z in unit of Si lattice constant a_0 of the (a) three lowest energy conduction and (b) highest valence band states in the Si (2 cells)/$Si_{0.57}$Ge0.43 (4 cells)/Si (2 cells) hetero-layer with 2 cells of vacuum padding. The $Si_{0.57}Ge_{0.43}$ layer is compressively strained along (x,y) plane while the top and bottom Si layers are relaxed assuming implicitly the substrate is (001) Si.

to vary with k_z at higher energies (> 3 eV) which exceeds the confinement energy caused by vacuum workfunction.

As introduced, Gomez *et al.* [37] showed an enhanced hole mobility in compressively strained SiGe MOSFETs with external (110) uniaxial strain and also showed that the hole mobility is larger in biaxially compressively strained Si/$Si_{0.57}Ge_{0.43}$/Si than Si only layer structure in the absence of the (110) uniaxial strain. However, it was not clearly shown in their work if the larger hole mobility in Si/$Si_{0.57}Ge_{0.43}$/Si layer is driven by effective mass modulated by strain or change in scattering. Thus, we calculate the band structure of Si/$Si_{1-x}Ge_x$/Si hetero-layers with different Ge

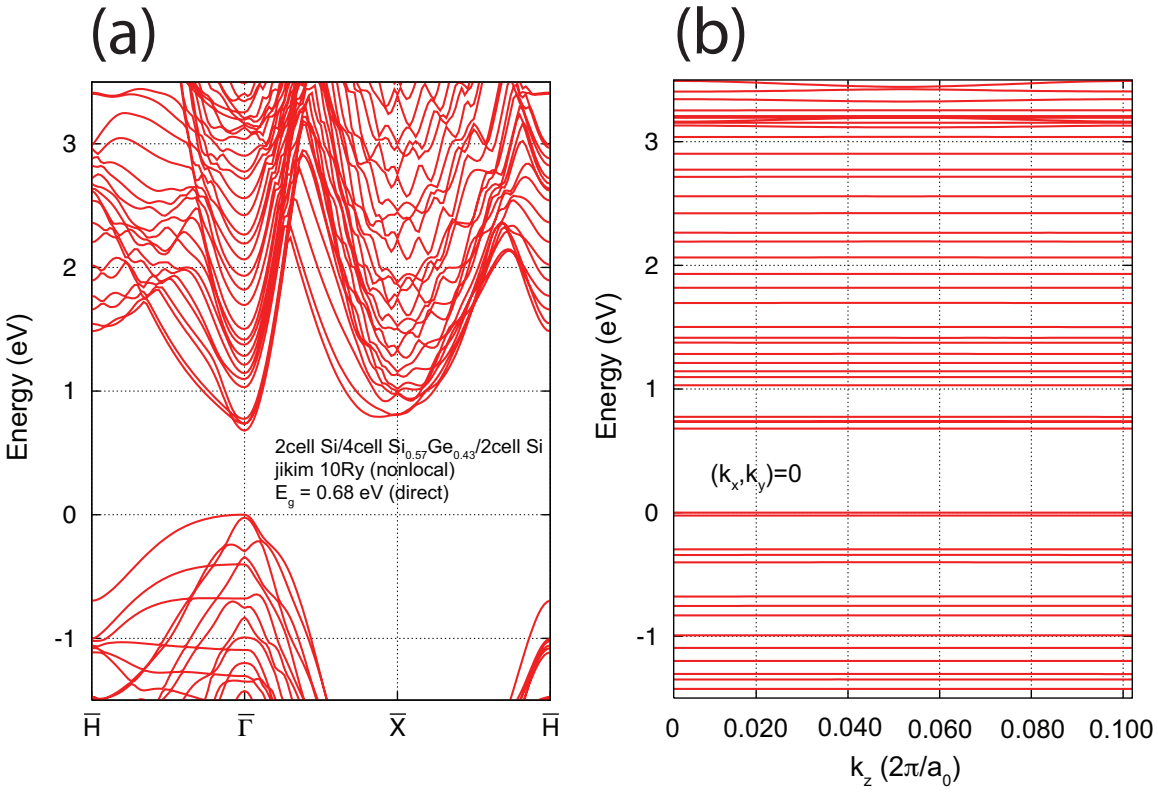

Figure 6.6. (a) Band structure of hydrogen passivated free standing (001) $Si/Si_{0.57}Ge_{0.43}/Si$ hetero-layer in 2D BZ. (b) Energy dispersion along the 'transverse' k_z direction at $\overline{\Gamma}$ point ($(k_x, k_y) = 0$)

concentration x to study if the change of the effective mass of carriers with Ge x can explain the larger hole mobility in $Si/Si_{0.57}Ge_{0.43}/Si$ layer. Figure 6.7 shows the calculated band structure of (a) Si-only, (b) $Si/Si_{0.57}Ge_{0.43}/Si$ and (c) Si/Ge/Si layers with the same layer thickness. The nature of the band gap changes from direct gap at $\overline{\Gamma}$ for Si-only to indirect gap near the $\overline{X}$ for $Si/Si_{0.57}Ge_{0.43}/Si$ with Ge $x = 0.43$ but the nature of the band gap returns to direct when the $x = 1.0$ in the case of Si/Ge/Si layer and also the band gap is slightly increased relative to the case of $x = 0.43$. In order to evaluate the effective mass of carriers at the zone center $\overline{\Gamma}$, we can employ the finite difference scheme to calculate the curvature effective mass from the band structure. However, instead of calculating curvature effective mass, we can still qualitatively estimate the effective mass by comparing the energy dispersion near the $\overline{\Gamma}$ since the effective mass is inversely proportional to the second derivatives of $E(k)$ so the effective mass increases as the curvature of the energy dispersion decreases. In Fig.6.8 we show the conduction and valence band structures near the $\overline{\Gamma}$ for the Si-only, $Si/Si_{0.57}Ge_{0.43}/Si$ and Si/Ge/Si layers. In the conduction bands the curvature of the energy dispersion along the $\overline{H}$ for the $Si/Si_{0.57}Ge_{0.43}/Si$ layer is the largest while it is the smallest for the Si-only layer implying the electron effective mass at the bottom of the conduction bands is the largest in the Si-only layer while the smallest in the $Si/Si_{0.57}Ge_{0.43}/Si$ layer. Similarly, the hole effective mass is the largest in the Si/Ge/Si layer while the smallest in the Si-only layer. In other word, the hole mobility is the largest in the Si-only layer since the carrier mobility is inversely proportional to the effective mass in the very approximated sense without taking into account the scattering rate. However, the larger hole mobility in the Si-only layer relative to the $Si/Si_{0.57}Ge_{0.43}/Si$ layer disagrees with the experiment by Gomez *et al.*. Thus the enhanced hole mobility in the $Si/Si_{0.57}Ge_{0.43}/Si$ layer from Gomez *et al.* can not be simply explained by the curvature effective mass from the band structure so the thorough evaluation of the scattering rate is needed.

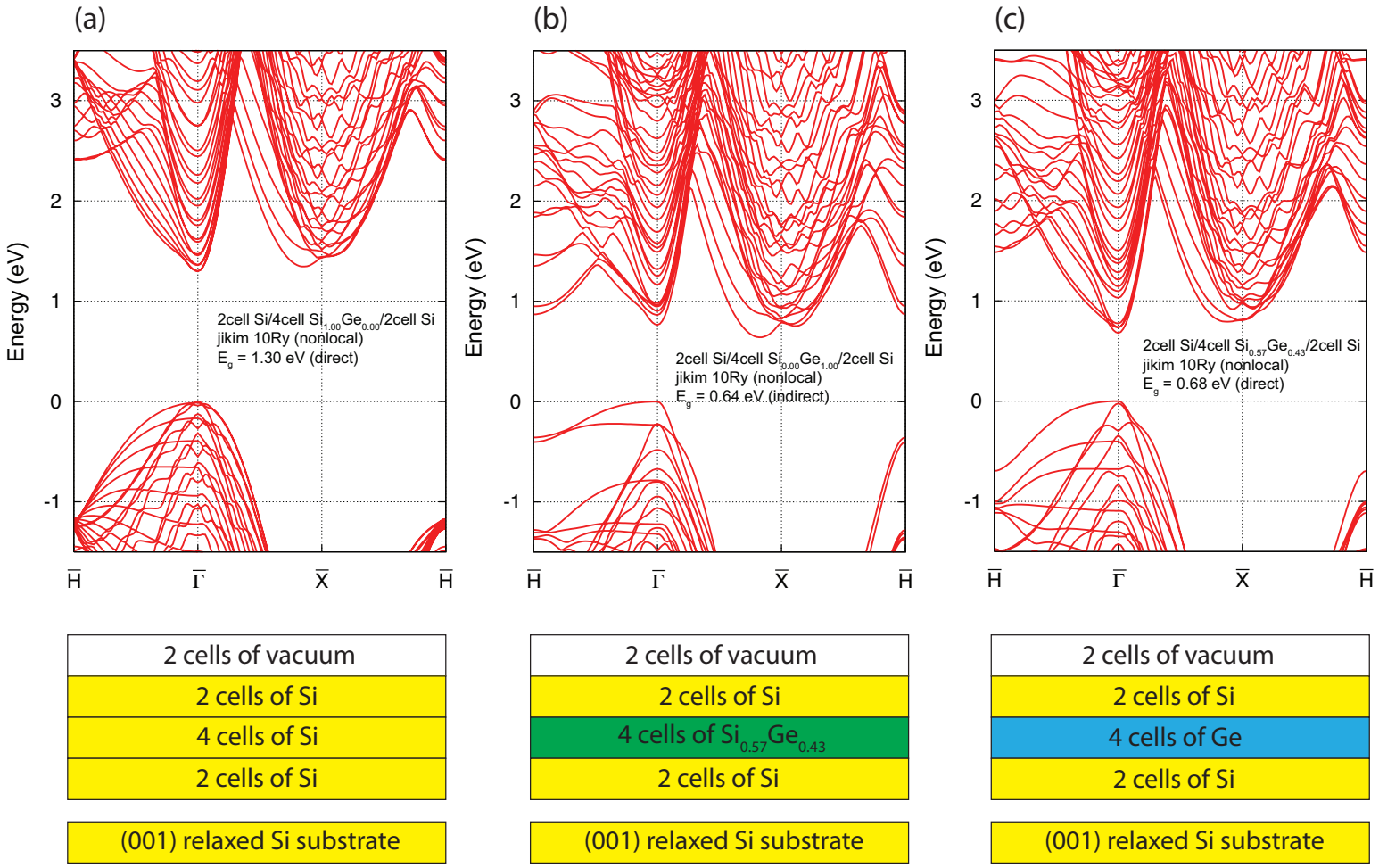

Figure 6.7. Band structure of hydrogen passivated free standing (001) (a) $Si/Si_{1.00}Ge_{0.00}/Si$ (Si-only), (b) $Si/Si_{0.57}Ge_{0.43}/Si$ and (c) $Si/Si_{0.00}Ge_{1.00}/Si$ (Si/Ge/Si) hetero-layers in 2D BZ along with schematic diagram of the layer structures. The Si substrate is not explicitly included in the structure but it gives a lattice constant for the whole layers structure and thus strain profile of the each layers are determined by the substrate lattice constant.

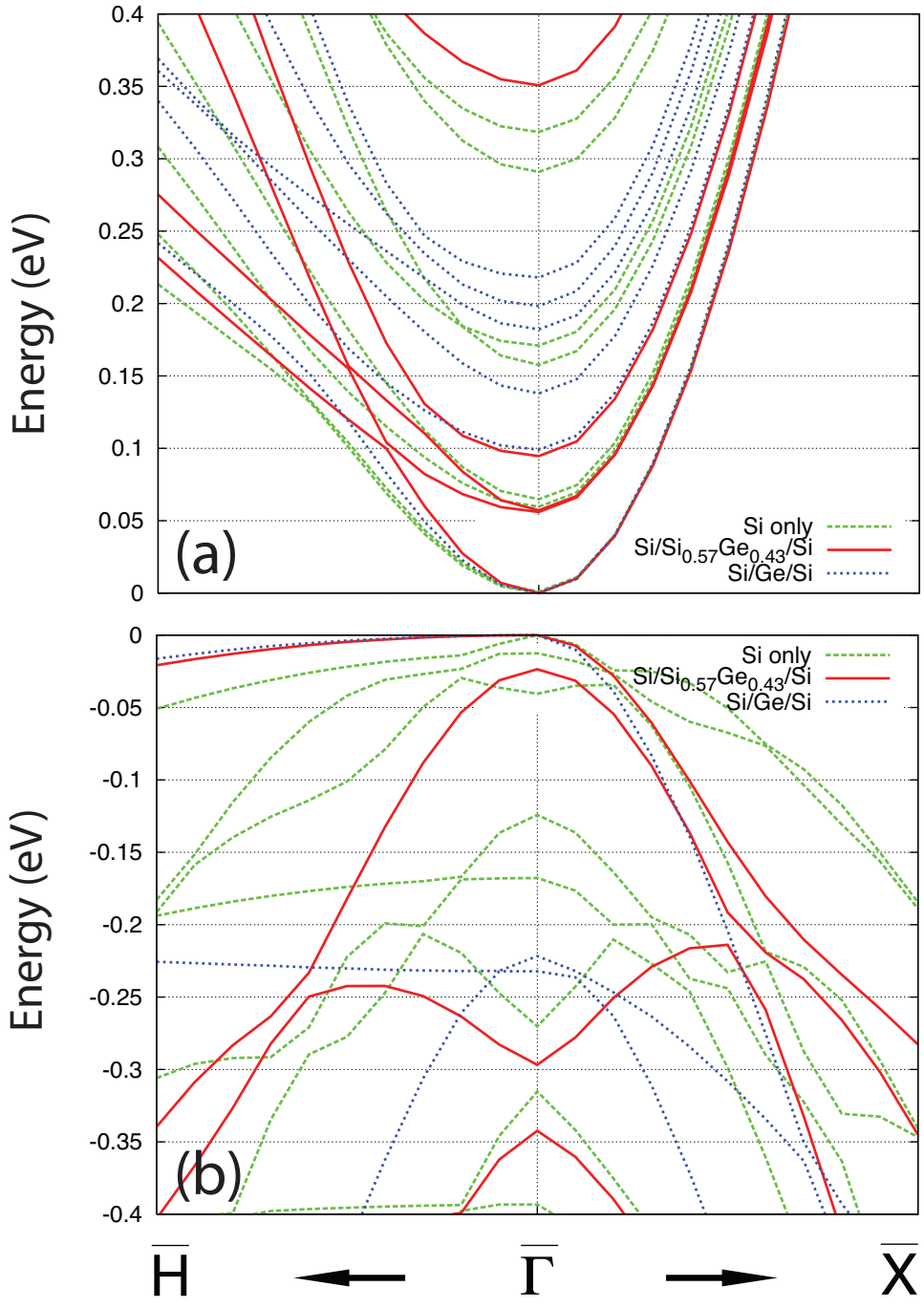

Figure 6.8. (a) Conduction and (b) valence band structures around the zone center $\overline{\Gamma}$ of Si-only (dashed line), $Si/Si_{0.57}Ge_{0.43}/Si$ (solid line) and Si/Ge/Si (dotted line) hetero-layers.

CHAPTER 7

BAND STRUCTURES FOR 2D SUPERCELL

The supercell method within plane-wave basis EPM can be also used for electronic structure calculation of two dimensionally confined system, *e.g.* 2D supercell, such as nanowires. Especially, Si nanowire (Si NW) FETs exhibit larger average transconductance and hole mobility when compared to state-of-the-art planar MOSFET [24]. Moreover, Si NWs have been shown to constitute excellent building blocks in assembling various types of semiconductor nanometer-scale devices via 'bottom-up' [23, 95] and 'top-down' [19, 27] approaches with controlled growth and crystallography, thus providing us one of our best chances to replace conventional planar-MOSFET-based integrated circuits. Si NWs are also excellent candidates for optoelectronics devices since their energy band gap can be either direct or indirect and its magnitude can be controlled by employing various crystal orientations, cross-section and strain [38, 25, 86, 42, 60, 75, 77, 72, 51, 78]. Strain in particular plays a significant role in modulating the gap and in changing its nature from direct to indirect which, in turn, leads to a variation of the effective masses [78, 51, 65, 42].

We investigate the electronic band structure of uniaxially strained, hydrogen passivated, square (or rectangular) cross-section Si NWs with axial directions oriented along the [001], [110], and [111] crystallographic axes. We mainly focus on the band structure as a function of the wire diameter, of the uniaxial strain applied along the wire axis, and the axial crystal orientation of the wires. Also, from the calculated full band structure in the 1D Brillouin Zone (BZ) we can extract the density of states (DOS), ballistic conductance, and carrier effective masses. The latter information

can provide a rough preliminary knowledge of the ideal transport properties of the wires.

7.1 Crystal Structure : Nanowire

7.1.1 [001] Axis

For [001] Si NW, we consider square cross-section wires with supercell translation vectors:

$$\begin{aligned} \vec{a}_1 &= \frac{1}{2}a_0 N_t(1+\epsilon_\parallel)(\hat{x}+\hat{y}) \\ \vec{a}_2 &= \frac{1}{2}a_0 N_t(1+\epsilon_\parallel)(-\hat{x}+\hat{y}) \\ \vec{a}_3 &= a_0(1+\epsilon_\perp)\hat{z} \end{aligned} \tag{7.1}$$

where $N_t = N + N_v$ denotes the total number of cells which is the sum of four-atom Si unit-cells N and a number of 'vacuum cells' N_v sufficiently large to ensure isolation between adjacent wires. The quantities $\epsilon_\parallel$ and $\epsilon_\perp$ denote the value of the strain on the (x, y)-plane (*i.e.*, biaxial strain on the cross-sectional plane) and along the z-direction (*i.e.*, uniaxial strain along the axial direction), respectively and $a_0 = 0.543$ nm is the Si lattice constant. For uniaxial strain along the wire-axis z the linear relation between $\epsilon_\parallel$ and $\epsilon_\perp$ is given by Eq. 2.67. We need four atoms in the unit cell and the atoms in the first unit cell ('gold' filled circles in Fig. 7.1) are placed at,

$$\begin{aligned} \vec{\tau}_1 &= 0 \\ \vec{\tau}_2 &= \frac{1}{4}a_0(\hat{x}+\hat{y}+\hat{z}) \\ \vec{\tau}_3 &= \frac{1}{4}a_0(2\hat{y}+2\hat{z}) \\ \vec{\tau}_4 &= \frac{1}{4}a_0(-\hat{x}+\hat{y}+3\hat{z}) \end{aligned} \tag{7.2}$$

then the unit cell is replicated N times along diagonal directions $x = y$ and $x = -y$ and the Si atoms in the replicated cells are represented as 'black' filled circles in Fig. 7.1. An additional layer of atoms are added to obtain a symmetric configuration as 'black' empty circles as shown in Fig. 7.1 and N_v vacuum cells are added. Two cells of vacuum padding are found to be sufficient to isolate adjacent wires by preventing any significant tunneling of the wavefunctions among neighboring wires. Each Si dangling bonds are passivated by H without surface reconstruction as discussed in the case of Si thin-layer in the previous section. Thus the area of the cross-section of the wire is $\frac{Na_0}{\sqrt{2}} \times \frac{Na_0}{\sqrt{2}}$ with $\{4N(N+1)+1\}$ Si atoms surrounded by $(8N+4)$ H atoms. The application of stress causes all of the atoms – including the H atoms – to be rigidly displaced to new positions $\boldsymbol{\tau}_i^{'}$ given by:

$$\begin{aligned} \tau_{i,(x,y)}^{'} &= \left[1+\epsilon_{\parallel}\right]\tau_{i,(x,y)} \\ \tau_{i,z}^{'} &= \left[1+\epsilon_{\perp}\right]\tau_{i,z}\ . \end{aligned} \tag{7.3}$$

Note that we have ignored the so called 'built-in' strain due to surface effects as obtained from total energy calculations [51] and an additional displacement with an internal displacement parameter [56].

7.1.2 [110] Axis

For [110] Si NW, we consider rectangular cross-sectional areas of NWs and choose the primitive translation vectors:

$$\begin{aligned} \vec{a}_1 &= \frac{\sqrt{2}}{2}a_0(N_x+N_v)(1+\epsilon_{\parallel})\hat{x} \\ \vec{a}_2 &= a_0(N_y+N_v)(1+\epsilon_{\parallel})\hat{y} \\ \vec{a}_3 &= \frac{\sqrt{2}}{2}a_0(1+\epsilon_{\perp})\hat{z} \end{aligned} \tag{7.4}$$

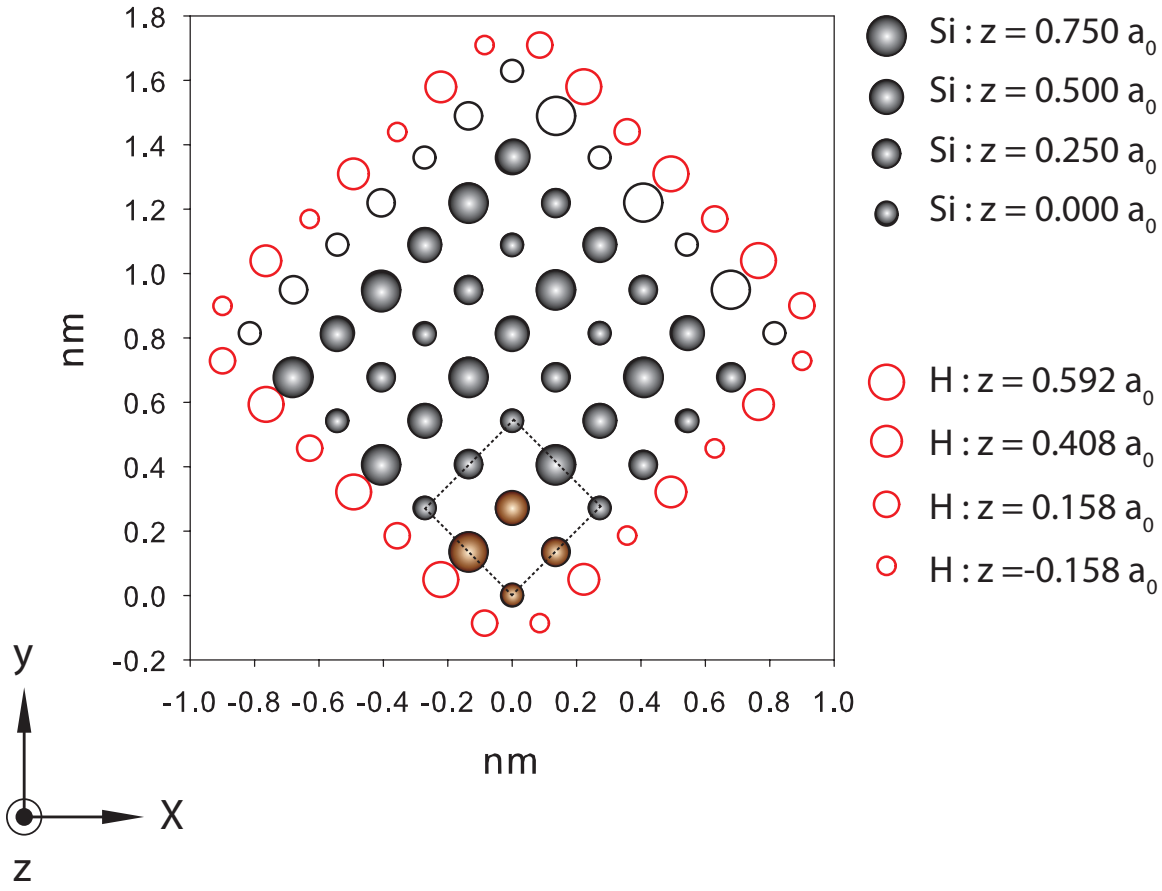

Figure 7.1. Positions of Si atoms for 3-cell×3-cell (1.15×1.15 nm^2) square cross-section, H passivated, relaxed [001] Si NW. Dotted square box indicate our choice of unit cell where the Si atoms in the unit cells from primitive lattice vector in Eq. 7.1 are represented as a filled 'gold' (first unit cell) and 'black' (repeated unit cell) circles while additional layer of atoms for symmetry configuration are represented as empty 'black' circles. Hydrogen atoms passivating Si dangling bonds without surface reconstruction are represented as empty 'red' circles.

where the N_x and N_y are the number of cells replicated along x- and y-direction. If uniaxial strain along the wire axis considered, the linear relation between $\epsilon_{\parallel}$ and $\epsilon_{\perp}$ can be determined using Eq. 2.73 as well. We consider four Si atoms in the unit cell as well as the [001] case and the atoms in the first unit cell ('gold' filled circles in Fig. 7.2) are placed at,

$$\begin{aligned}
\vec{\tau}_1 &= 0 \\
\vec{\tau}_2 &= \frac{1}{4}a_0(\hat{y} + \sqrt{2}\hat{z}) \\
\vec{\tau}_3 &= \frac{1}{4}a_0(\sqrt{2}\hat{x} + 2\hat{y} + \sqrt{2}\hat{z}) \\
\vec{\tau}_4 &= \frac{1}{4}a_0(\sqrt{2}\hat{x} + 3\hat{y})
\end{aligned} \tag{7.5}$$

then the cell is replicated N_x and N_y times along x- and y-direction in Fig. 7.2 where the Si atoms in the replicated cells are represented as 'black' filled circles. Also, additional layer of atoms for symmetric configuration is added as 'black' empty circles in Fig. 7.2 and N_v vacuum cells are added. H atoms also added to passivate the Si dangling bonds as 'red' empty circles in Fig. 7.2. The area of the cross-section of the wire is $\frac{\sqrt{2}}{2}N_x a_0 \times N_y a_0$ and contains $4N_xN_y + 2N_y + N_x + 1$ Si atoms surrounded by $4N_x + 4N_y + 4$ H atoms.

7.1.3 [111] Axis

For [111] Si NW, we also consider rectangular cross-sectional NWs and choose the primitive translation vectors:

$$\begin{aligned}
\vec{a}_1 &= \frac{\sqrt{2}}{2}a_0(N_x + N_v)(1 + \epsilon_{\parallel})\hat{x} \\
\vec{a}_2 &= \sqrt{\frac{3}{2}}a_0(N_y + N_v)(1 + \epsilon_{\parallel})\hat{y} \\
\vec{a}_3 &= \sqrt{3}a_0(1 + \epsilon_{\perp})\hat{z}
\end{aligned} \tag{7.6}$$

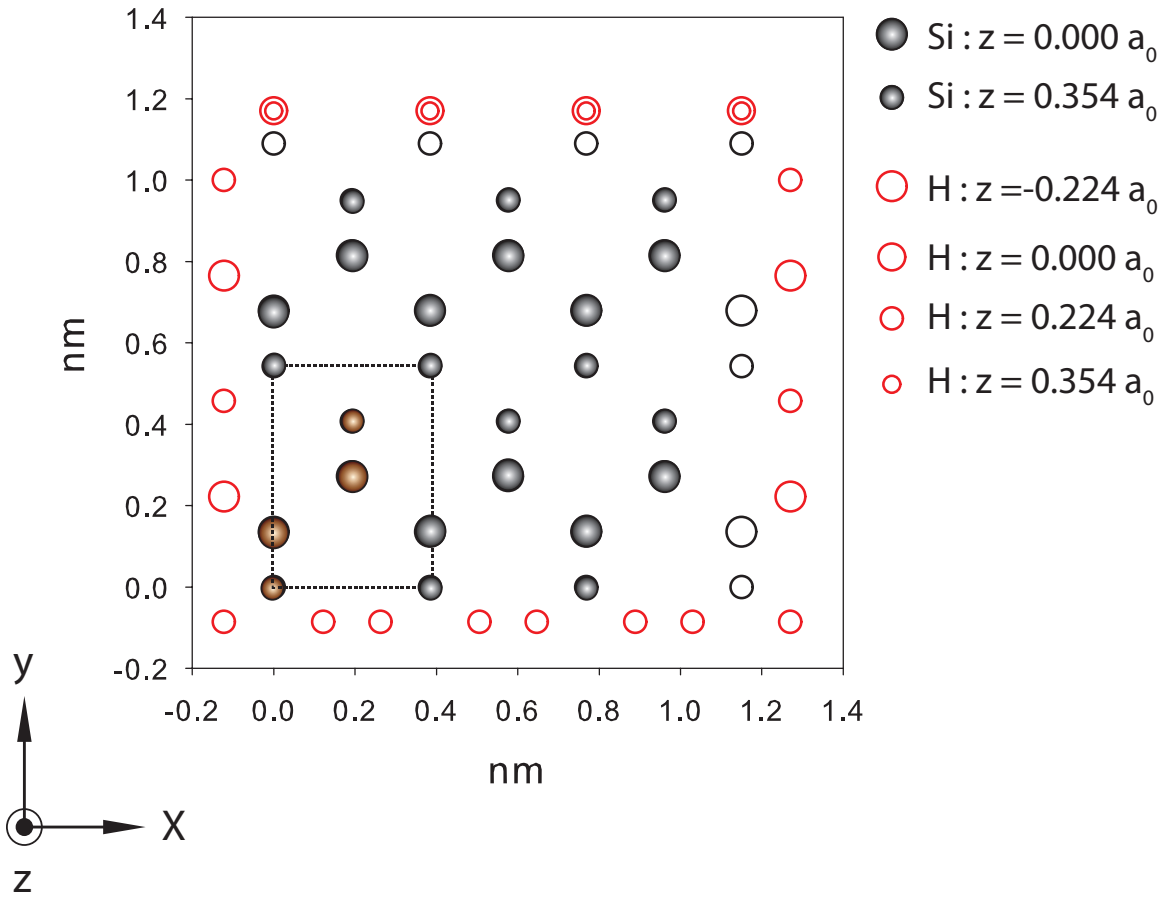

Figure 7.2. Positions of Si atoms for 3-cell×2-cell (1.15×1.09 nm^2) square (almost) cross-section, H passivated, relaxed [110] Si NW. See Fig. 7.1 for detailed descriptions of the figure.

where the N_x and N_y are the number of cells replicated along x- and y-direction. If uniaxial strain along the wire axis considered, the linear relation between $\epsilon_{\parallel}$ and $\epsilon_{\perp}$ can be determined using Eq. 2.80 as well. We consider twelve Si atoms in the unit cell since the periodicity along the [111] wire axis is much larger than the cases of the [001] and [110] wires requiring more plane waves in computation. For example, $N_x = 3$ and $N_y = 2$ (1.15×1.33 nm^2 cross-section) [111] wire with energy cut-off 8Ry requires about 12,000 G-vectors which is practically unable to compute. The Si atoms in the first unit cell ('gold' filled circles in Fig. 7.3) are placed at,

$$
\begin{aligned}
\vec{\tau}_1 &= 0 \\
\vec{\tau}_2 &= a_0 \left[\frac{1}{2\sqrt{2}}\hat{x} + \frac{\sqrt{3}}{2\sqrt{2}}\hat{y} \right] \\
\vec{\tau}_3 &= a_0 \left[\frac{\sqrt{3}}{4}\hat{z} \right] \\
\vec{\tau}_4 &= a_0 \left[\frac{1}{2\sqrt{2}}\hat{x} + \frac{\sqrt{3}}{2\sqrt{2}}\hat{y} + \frac{\sqrt{3}}{4}\hat{z} \right] \\
\vec{\tau}_5 &= a_0 \left[\frac{1}{\sqrt{6}}\hat{y} + \frac{1}{\sqrt{3}}\hat{z} \right] \\
\vec{\tau}_6 &= a_0 \left[\frac{1}{2\sqrt{2}}\hat{x} + \left(\frac{1}{\sqrt{6}} + \frac{\sqrt{3}}{2\sqrt{2}} \right) \hat{y} + \frac{1}{\sqrt{3}}\hat{z} \right] \\
\vec{\tau}_7 &= a_0 \left[\frac{1}{\sqrt{6}}\hat{y} + \left(\frac{\sqrt{3}}{4} + \frac{1}{\sqrt{3}} \right) \hat{z} \right] \\
\vec{\tau}_8 &= a_0 \left[\frac{1}{2\sqrt{2}}\hat{x} + \left(\frac{1}{\sqrt{6}} + \frac{\sqrt{3}}{2\sqrt{2}} \right) \hat{y} + \left(\frac{\sqrt{3}}{4} + \frac{1}{\sqrt{3}} \right) \hat{z} \right] \\
\vec{\tau}_9 &= a_0 \left[\frac{1}{2\sqrt{2}}\hat{x} + \frac{1}{2\sqrt{6}}\hat{y} + \frac{2}{\sqrt{3}}\hat{z} \right] \\
\vec{\tau}_{10} &= a_0 \left[\frac{1}{\sqrt{2}}\hat{x} + \left(\frac{1}{2\sqrt{6}} + \frac{\sqrt{3}}{2\sqrt{2}} \right) \hat{y} + \frac{2}{\sqrt{3}}\hat{z} \right] \\
\vec{\tau}_{11} &= a_0 \left[\frac{1}{2\sqrt{2}}\hat{x} + \frac{1}{2\sqrt{6}}\hat{y} + \left(\frac{2}{\sqrt{3}} + \frac{\sqrt{3}}{4} \right) \hat{z} \right] \\
\vec{\tau}_{12} &= a_0 \left[\frac{1}{\sqrt{2}}\hat{x} + \left(\frac{1}{2\sqrt{6}} + \frac{\sqrt{3}}{2\sqrt{2}} \right) \hat{y} + \left(\frac{2}{\sqrt{3}} + \frac{\sqrt{3}}{4} \right) \hat{z} \right]
\end{aligned}
\tag{7.7}
$$

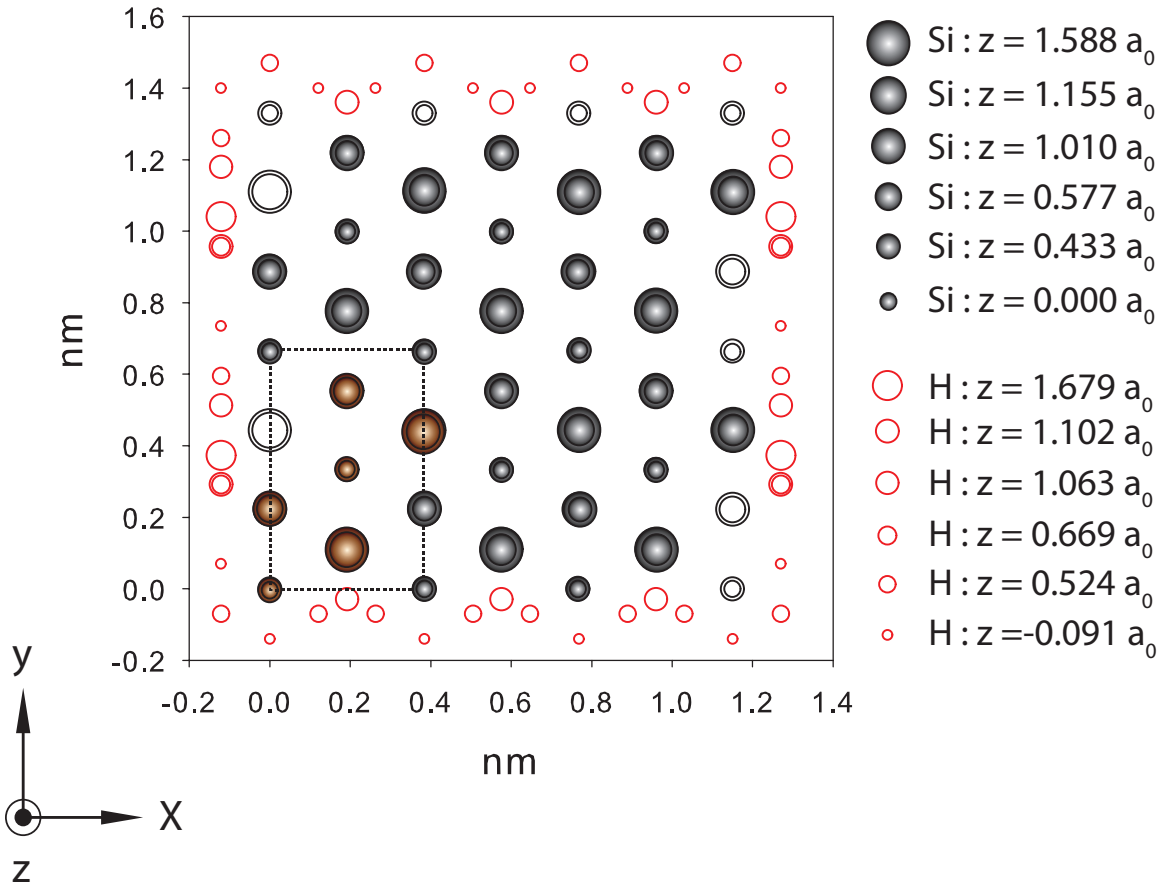

Figure 7.3. Positions of Si atoms for 3-cell×2-cell (1.15×1.33 nm^2) square (almost) cross-section, H passivated, relaxed [111] Si NW. See Fig. 7.1 for detailed descriptions of the figure.

then the cell is replicated N_x and N_y times along x- and y-direction in Fig. 7.3 where the Si atoms in the replicated cells are represented as 'black' filled circles. Additional layer of atoms for symmetric configuration is added as 'black' empty circles in Fig. 7.3 and N_v vacuum cells are added. H atoms also added to passivate the Si dangling bonds as 'red' empty circles in Fig. 7.3. The area of the cross-section of the [111] wire is $\sqrt{\frac{1}{2}}N_x a_0 \times \sqrt{\frac{3}{2}}N_y a_0$ and contains $12N_xN_y + 6N_y + 2N_x + 2$ Si atoms surrounded by $8N_x + 12N_y + 6$ H atoms.

7.2 Band Structure of Relaxed Si Nanowires

As discussed in Chap. 5, we employ our bulk Si $V(q)$ for Si NW with nonlocal corrections. Spin-orbit corrections, however, are ignored, since the spin-orbit splitting for bulk Si is not significant. In order to reduce the computational cost even further by reducing the rank of the Hamiltonian matrix, we have used a smaller energy cut-off $E_{cut} = 7$ Ry, choice which still leads to results satisfactorily close to those obtained by employing the value of 10 Ry used before [44]. For H we use the pseudopotential employed by Wang *et al.*, as mentioned [89]. Also, we employ the two cells of vacuum paddings to insulate adjacent wires. Figure 7.4, 7.5 and 7.6 show squared amplitude - averaged over a supercell along the axial direction (z-direction) - of wave functions of three lowest energy conduction and three highest energy valence bands states in the [001], [110] and [111] NWs. Note the wavefunctions slightly tunnel into the vacuum area but the wire appears to be well isolated from the neighboring wires with two cells of vacuum. If we take just one cell of vacuum, then the wavefunctions would tunnel into the neighboring wires resulting in undesirable coupling of wavefunctions.

Then, we have benchmarked our band-structure results to those obtained using Zhang's local pseudopotentials [99], as shown in Fig. 7.7 for the case of relaxed [001] Si NW. The good qualitative agreement gives us confidence about the 'portability' of our pseudopotentials. Also, the interpolated local pseudopotential $V(q)$ we employ augmented by nonlocal corrections shows a better qualitative agreement with *ab initio* calculations when the wire is uniaxially strained, especially for [110] wire, as we shall discuss in Sec. 7.3 below.

In Fig. 7.8 we present the band-structure for relaxed [001], [110], and [111] Si NWs – together with the 1D density of states (DOS) – as calculated using our local pseudopotential $V(q)$ with nonlocal corrections. Note that [001]- and [110]-oriented nanowires exhibit a direct band gap at Γ, while the band gap remains indirect for [111]-oriented wires. The nature of the direct band gap for [001] wires

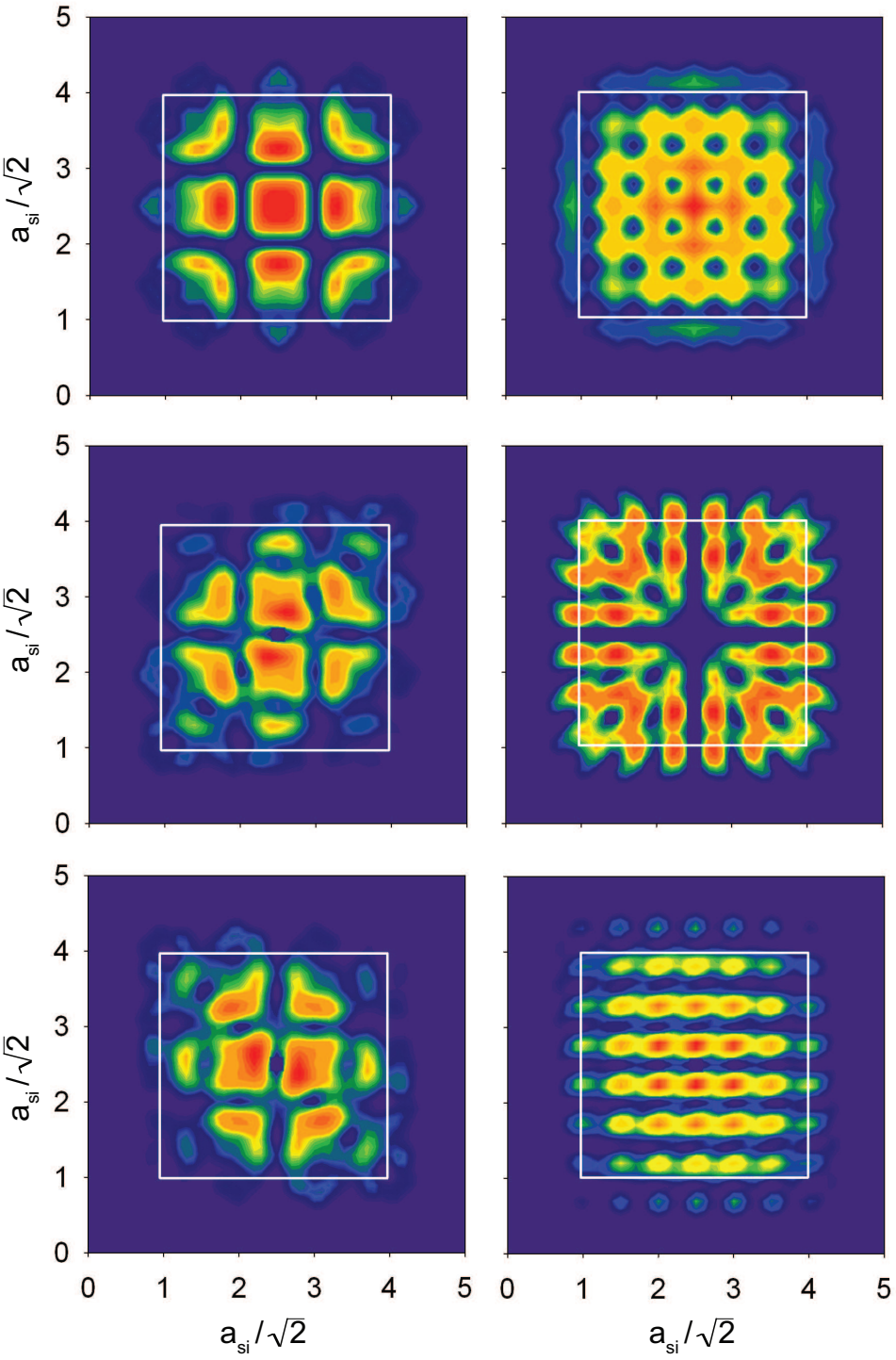

Figure 7.4. Squared amplitude - averaged over a supercell along the axial direction - of the wave functions of the three lowest energy conduction (left from the top) and highest valence (right from the top) band states in the square cross-section, 1.15×1.15 nm^2 represented as a white solid square indicating , [001] Si NW with two cells of vacuum paddings surrounding the Si square. The minimum of the squared amplitude is set to be 10^{-5}.

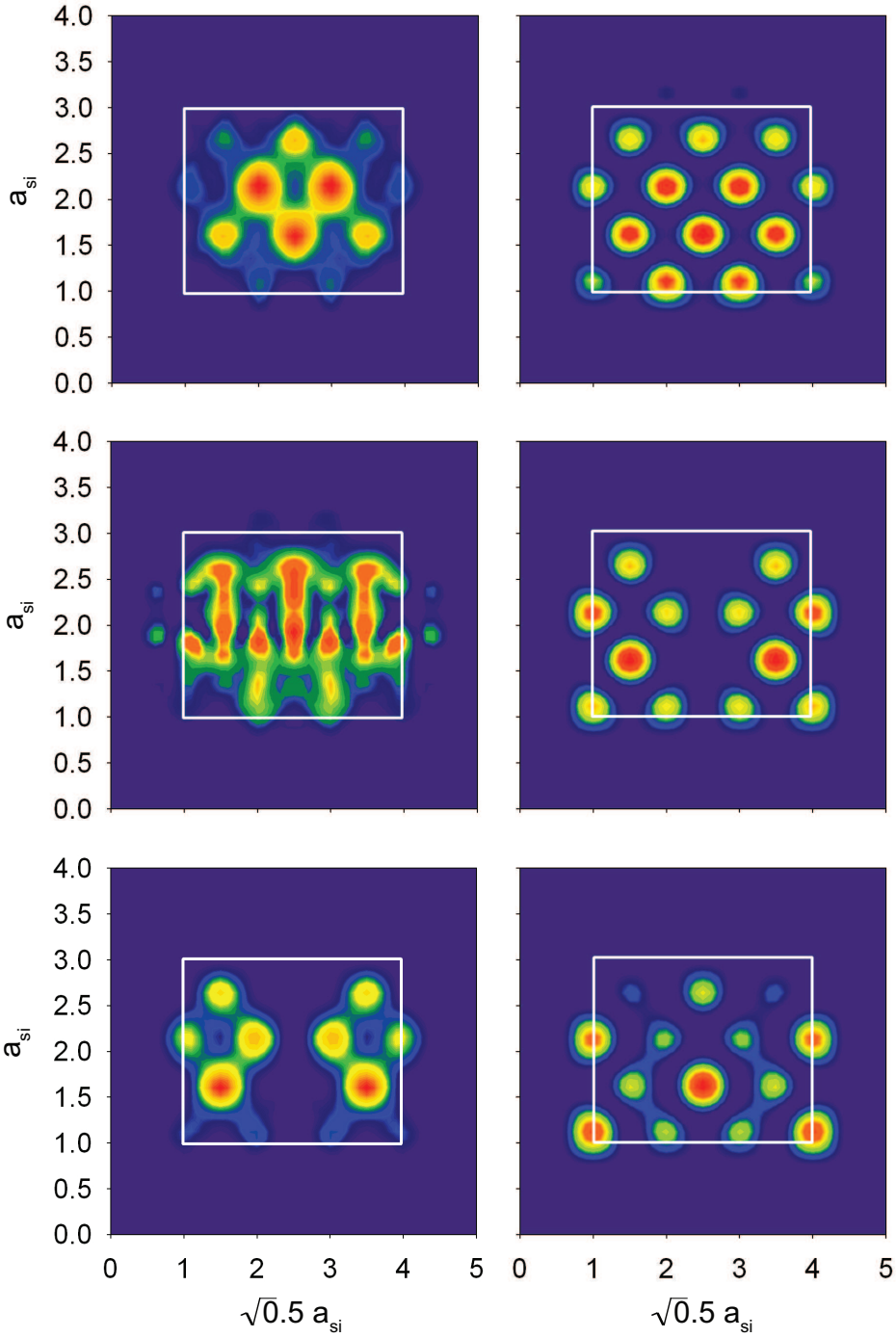

Figure 7.5. Squared amplitude - averaged over a supercell along the axial direction - of the wave functions of the three lowest energy conduction (left from the top) and highest valence (right from the top) band states in the square (almost) cross-section, 1.15×1.09 nm^2 represented as a white solid square indicating , [110] Si NW with two cells of vacuum paddings surrounding the Si square. The minimum of the squared amplitude is set to be 10^{-5}.

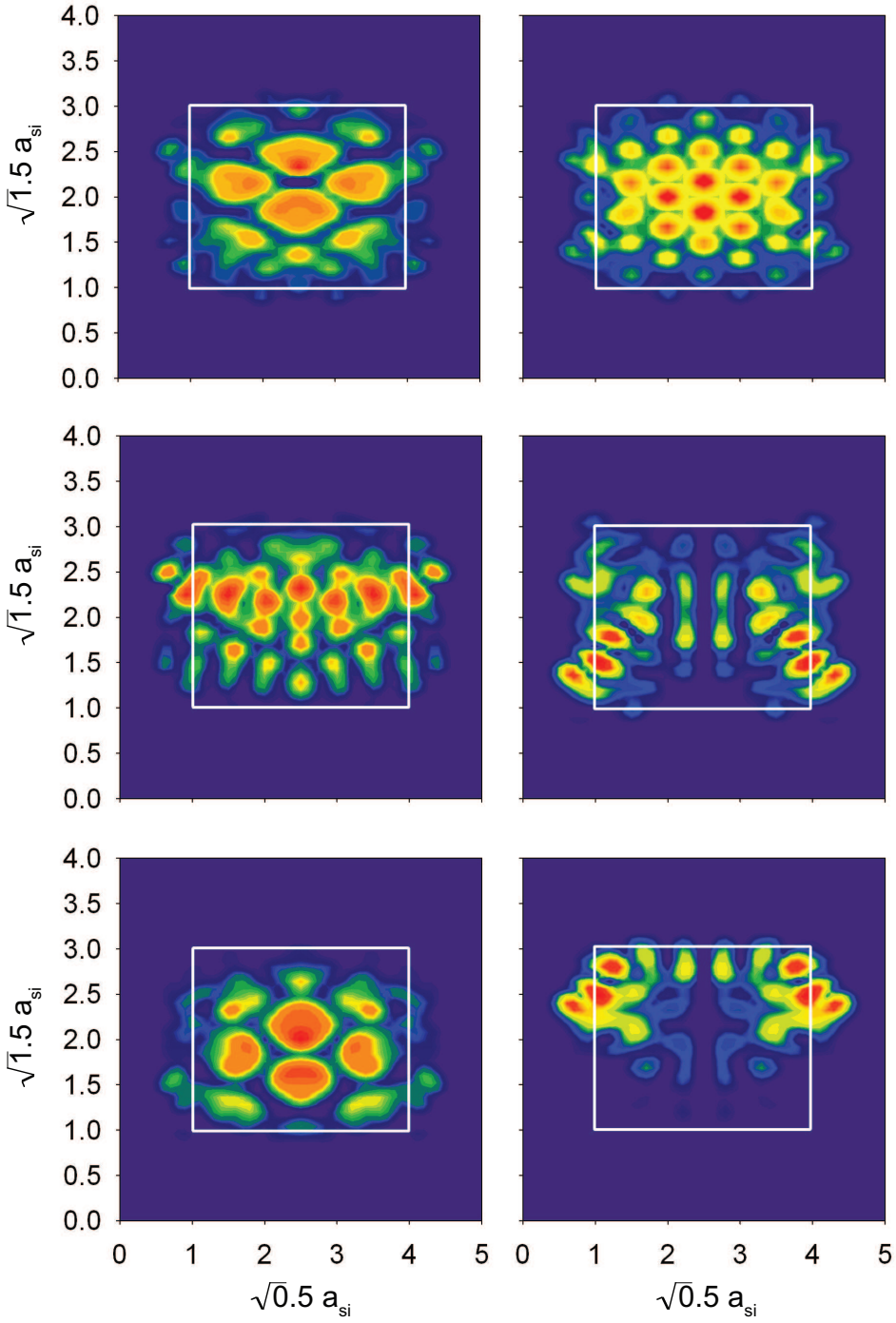

Figure 7.6. Squared amplitude - averaged over a supercell along the axial direction - of the wave functions of the three lowest energy conduction (left from the top) and highest valence (right from the top) band states in the square (almost) cross-section, 1.15×1.33 nm^2 represented as a white solid square indicating , [111] Si NW with two cells of vacuum paddings surrounding the Si square. The minimum of the squared amplitude is set to be 10^{-5}.

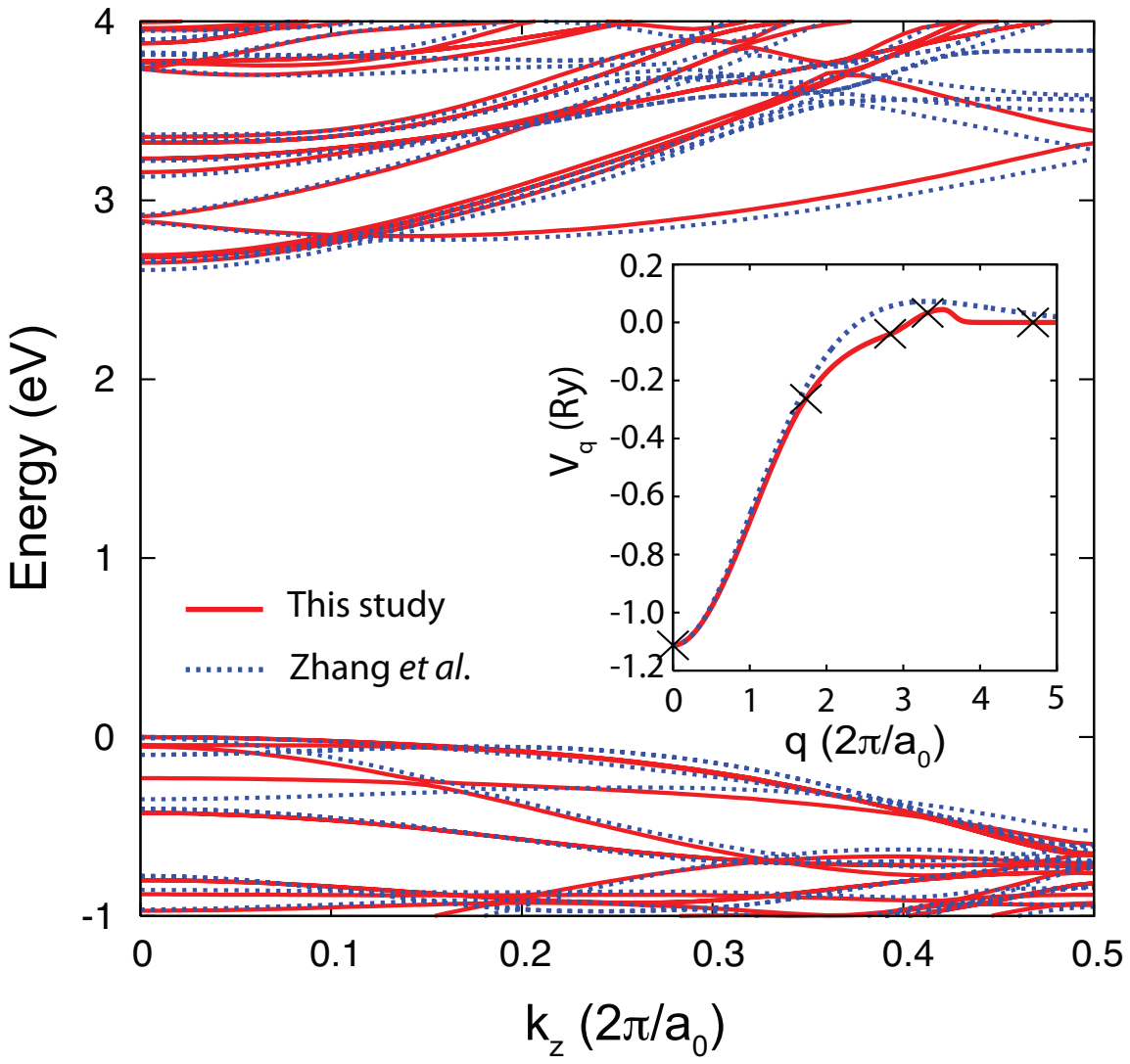

Figure 7.7. Band structure of a relaxed [001] Si NW with a square cross-section area of 1.54 × 1.54 nm^2. The energy scale is fixed by setting arbitrarily the top of the valence band to zero. We compare the band structure using two different pseudopotentials from Ref. [44] with E_{cut}=7 Ry, which is employed in this study, and from Ref. [99] with E_{cut}=8 Ry, shown in inset as solid and dashed lines, respectively.

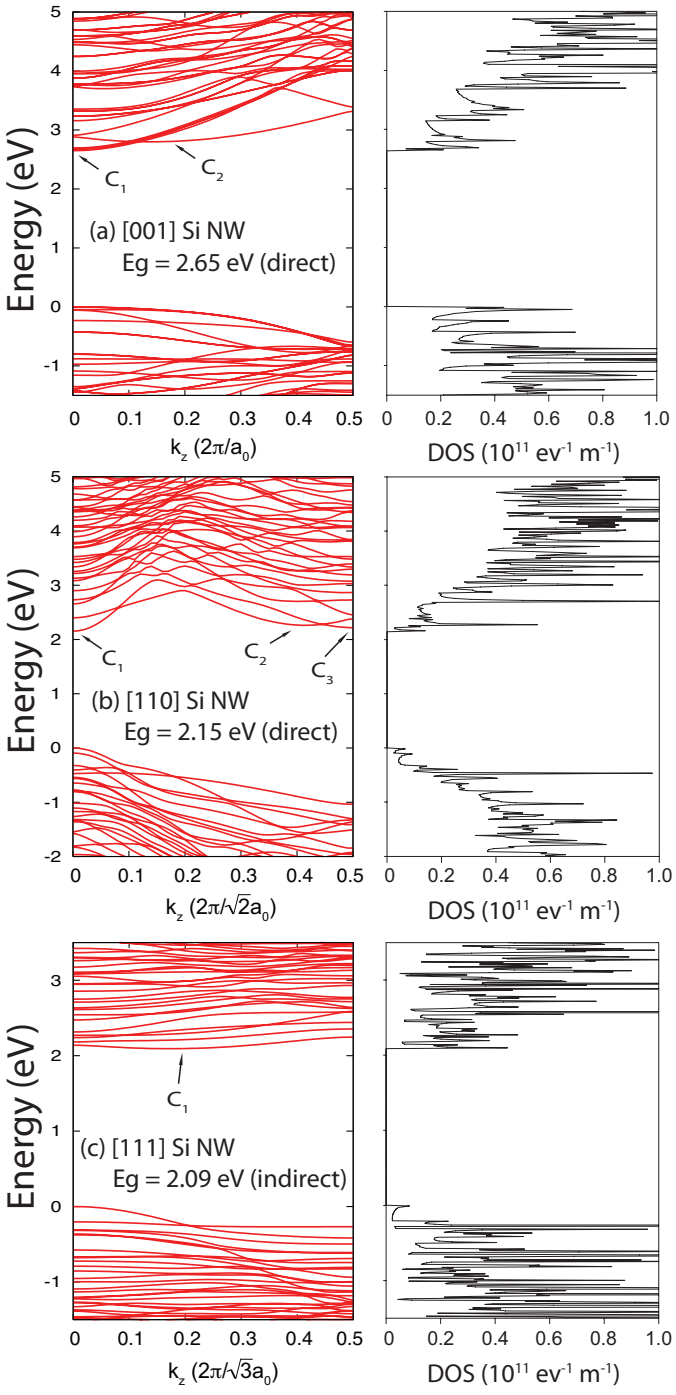

Figure 7.8. Band structure (left) and density of states (DOS) (right) of free-standing, relaxed, H passivated (a) [001] (1.15×1.15 nm^2), (b) [110] (1.15×1.09 nm^2) and (c) [111] (1.15×1.33 nm^2) square (almost) cross-section Si NWs with two cells of vacuum padding. The energy scale is fixed by setting arbitrarily top of the valence band to zero.

can be qualitatively explained from the bulk Si band structure with effective-mass theory [72] considering six equivalent conduction band minima (CBM) (Δ_6) located at $(0, 0, \pm 0.84)2\pi/a_0$, $(0, \pm 0.84, 0)2\pi/a_0$ and $(\pm 0.84, 0, 0)2\pi/a_0$ with ellipsoidal equi-energy surfaces with a longitudinal effective mass $m_{e,l}^{*(\Delta)} = 0.891m_0$ and a transverse effective mass $m_{e,t}^{*(\Delta)} = 0.202m_0$ [44] (where m_0 is the free electron mass). Since the Si NW is confined along the [100] and [010] directions for the case of a [001]-oriented wire, the two CBM (Δ_2) at $(0, 0, \pm 0.84)2\pi/a_0$ (labeled 'C_2' in Fig. 7.8 (a)) and the four CBM (Δ_4) at $(0, \pm 0.84, 0)2\pi/a_0$ and $(\pm 0.84, 0, 0)2\pi/a_0$ (labeled 'C_1' in Fig. 7.8 (a)) which are folded onto the Γ point, are shifted upward in energy – because of quantum-confinement effects – by a different amount. The C_2 valley shifts upward by a large amount due to the small transverse effective mass along the confinement direction, while the upward shift of the C_1 valley is smaller due to the large longitudinal effective mass in the confinement plane, thus resulting in a direct band gap at Γ [72, 42, 86].

Similarly, for the [110] Si NW, the two-fold CBM (Δ_2) at Γ (labeled C_1 in Fig. 7.8 (b)) is lower in energy than the four-fold CBM (Δ_4) (labeled C_2 in Fig. 7.8 (b)), resulting in a direct band gap since the shift of the C_1 valley in energy is determined by the large longitudinal effective mass, while the energy shift of C_2 valley is determined by the small transverse effective mass [51, 101, 77, 42]. However, for [110]-oriented wire only one of the [001] directions lies in the confinement plane, thus making the C_1 valleys less efficiently folded onto the Γ point. As can be seen in Fig. 7.8 (b), even though the CBM is located at Γ, the nature of the band gap remains indirect, although its nature is 'quasi-direct', as the DOS of C_1 valley is much smaller than the DOS of the C_2 valley because of the large longitudinal effective mass in the confinement plane [77]. In addition, we notice another conduction band valley C_3 near the point $k_z = 0.5 \times 2\pi/\sqrt{2}a_0$, which is the projection of bulk Si conduction band at X. This minimum is at a lower energy than the C_2 minimum since the transverse effective

mass at X ($m_{e,t}^{*(X)} = 0.215m_0$) [44] is larger than the mass at Δ_6 ($m_{e,t}^{*(\Delta)} = 0.202m_0$). Note that this C_3 valley does not seem to be present in the results of most *ab initio* calculations [42, 96, 77, 86], except for those of Ref. [51].

In the case of [111]-oriented wires, the CBM are associated with the Δ_6-minima (labeled 'C_1' in Fig. 7.8 (c)), which can not be folded onto Γ, being instead folded at a k-point near X, so that the wires still exhibit an indirect band gap. However, the nature of the indirect band gap of [111]-oriented wires can not be guaranteed by simple considerations based on effective-mass theory: First-principles calculations by Vo *et al.* [86] have shown that [111]-oriented Si NWs with a diameter of 2 nm and canted dihydride surfaces exhibit an indirect gap but remain direct when the surface is reconstructed. They have also shown that [111] wires with a diameter of 3 nm with both canted and reconstructed surfaces exhibit an indirect gap [86]. But things are even more complicated, since the indirect gap nature of the [111] Si NWs has been reported in Refs. [66], [51] and [42], while the direct nature of the gap has been reported in Refs. [65] and [38].

Because of a reduction of quantum-confinement effects, the band gap of NWs decreases nonlinearly as diameter of the wire increases [72, 63, 86, 101]. This effect, calculated here and compared to other theoretical results using *ab initio* DFT/LDA [77, 25, 86, 51] and semiempirical TBM [78] calculations, is shown in Fig. 7.9 for wire diameters in the range 0.65 nm - 2.04 nm. Our results for all orientations are summarized in Fig. 7.9 (d), having determined the diameter of the wires (not necessarily all having an exactly square cross section) by taking the square root of the wire cross-sectional area. In the following we shall use the term 'diameter' with this definition in mind. Note that the band gap of [001] wires is always the largest while [110] wires exhibit the smallest gap for a diameter larger than ~ 1 nm. Also note the transition from indirect gap (represented as 'empty' symbols) to direct gap (represented as 'solid' symbols) for [110]-oriented wires as the wire diameter increases. The direct-to-indirect band gap

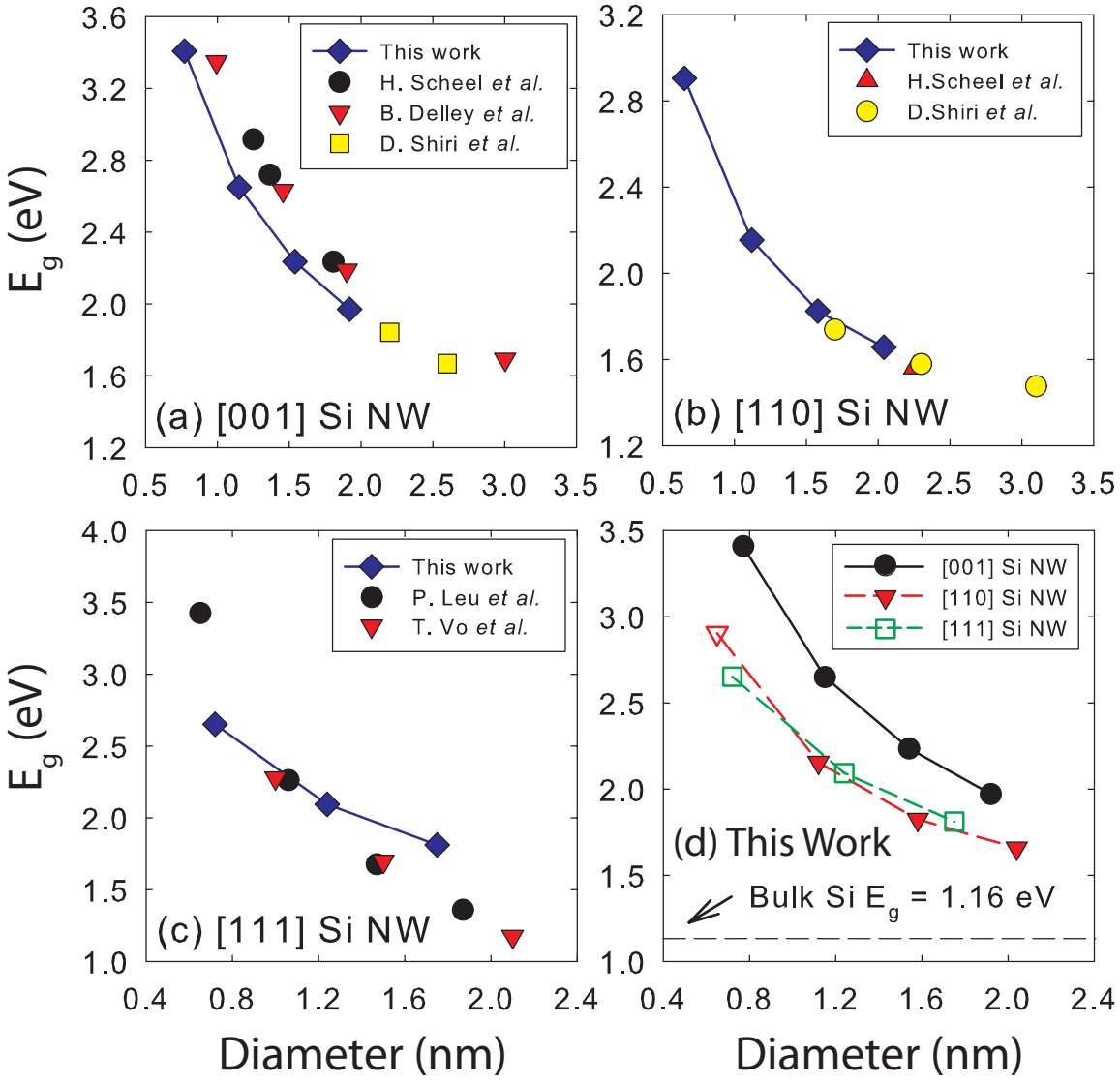

Figure 7.9. Energy band gap as a function of wire diameter for (a) [001], (b) [110] and (c) [111] Si NWs. Our results (solid lines with symbols) are compared to various theoretical calculations (symbols) including density functional theory (DFT) within the local density approximation (LDA) [77, 25, 86, 51] and semiempirical tight binding (TB) [78]. Our results for all orientations are shown in (d), having indicated the direct and indirect band gaps with solid and empty symbols, respectively, and the bulk Si band gap [44] is shown as a reference (horizontal dashed line). Note that the 'diameter' of the wire is defined as the square root of the wire cross-sectional area.

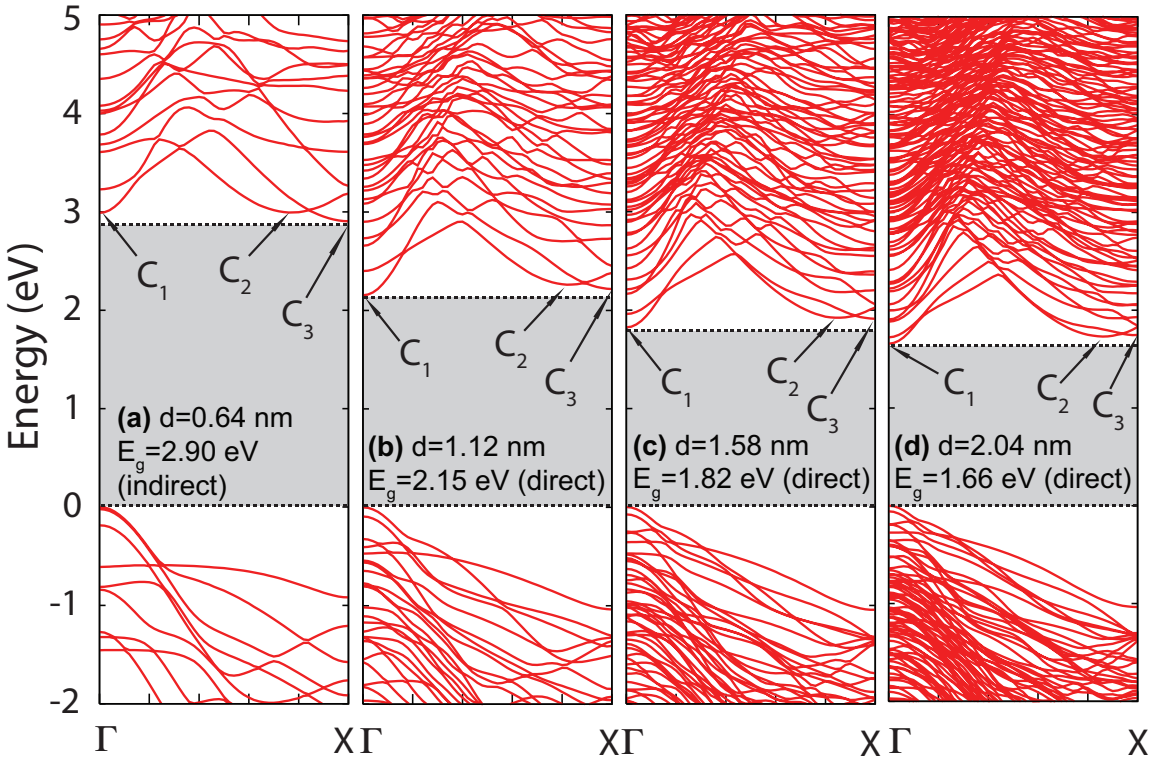

Figure 7.10. Band structure of relaxed [110] Si NWs with different diameters: (a) d = 0.64 nm, (b) d = 1.12 nm, (c) d = 1.58 nm, and (d) d = 2.04 nm. The conduction-band minimum (BCM) and the valence-band maximum (VBM) are represented as horizontal dashed lines and the VBM is arbitrarily set to zero. The band gap region is represented by a filled area.

transition for [110] wires is more clearly seen in Fig. 7.10 in which we have indicated with horizontal dashed lines the CBM and valence band maximum (VBM). For the smallest diameter (Fig. 7.10 (a)) the CBM stems from the C_3 valley, thus resulting in an indirect band gap. However, as the diameter of the wire increases, the C_1 valley shifts energetically down further than the C_3 valley, resulting in a direct band gap. Also, the C_2 valley shifts lower in energy than the C_3 valley which almost disappears at the largest diameter we have considered.

7.3 Band Structure of Strained Si Nanowires

In this section, we discuss the effect of uniaxial strain on the band structure of the Si NWs. Figure 7.11 shows the conduction band structure modulated by uniaxial strain for a 1.15 nm diameter [001] Si NW varying the strain from -2% (compressive) to +2% (tensile). As we discussed in the previous section, confinement effects split the bulk CBM (Δ_6) into $C_1(\Delta_4)$ and $C_2(\Delta_2)$ valleys. The C_1 energy is lower than the C_2 energy, resulting in a direct band gap in relaxed wires, as shown in Fig. 7.11 (c). However, the C_2 valley shifts significantly downward while the C_1 valley shifts energetically in the opposite direction (upward) as the amount of compressive strain increases. This causes a direct-to-indirect band gap transition at a value of -2% strain, as seen in Fig. 7.11 (a). On the other hand, when tensile strain is applied, the C_2 valley shifts significantly upward energetically, while the C_1 valley shifts downward, as shown in Fig. 7.11 (d) and (e). Note that in this case the band gap remains direct. These strain-induced energy shifts of the C_1 and C_2 valleys can be understood qualitatively from consideration derived from the bulk band-structure of strained Si, as discussed in Refs. [44] and [30]. In this case the energy of the C_2 valleys (denoted by Δ_{100} in Ref. [30]) decreases while the energy of the C_1 valleys (denoted by Δ_{001} in Ref. [30]) increases – relative to the relaxed case conduction-band minimum at Δ_6 – as the amount of compressive strain increases. Quantitatively, we can obtain an

uniaxial deformation potential Ξ_u^Δ for [001] Si NWs using linear deformation-potential theory [85] relating the relative energy shifts, ΔC_1 and ΔC_2, of the conduction bands C_1 and C_2 to the axial and cross-sectional strain components as follows:

$$\Delta C_1 - \Delta C_2 = \Xi_u^\Delta(\epsilon_\perp - \epsilon_\parallel) \ . \tag{7.8}$$

When the uniaxial strain is small (*e.g.*, when $\epsilon_\perp = -0.02$) we find that $\Xi_u^\Delta = 9.48$ for a 1.15 nm-diameter [001] Si NW, a value about 6% smaller than in bulk Si, $\Xi_u^\Delta = 10.1$ from Ref. [44].

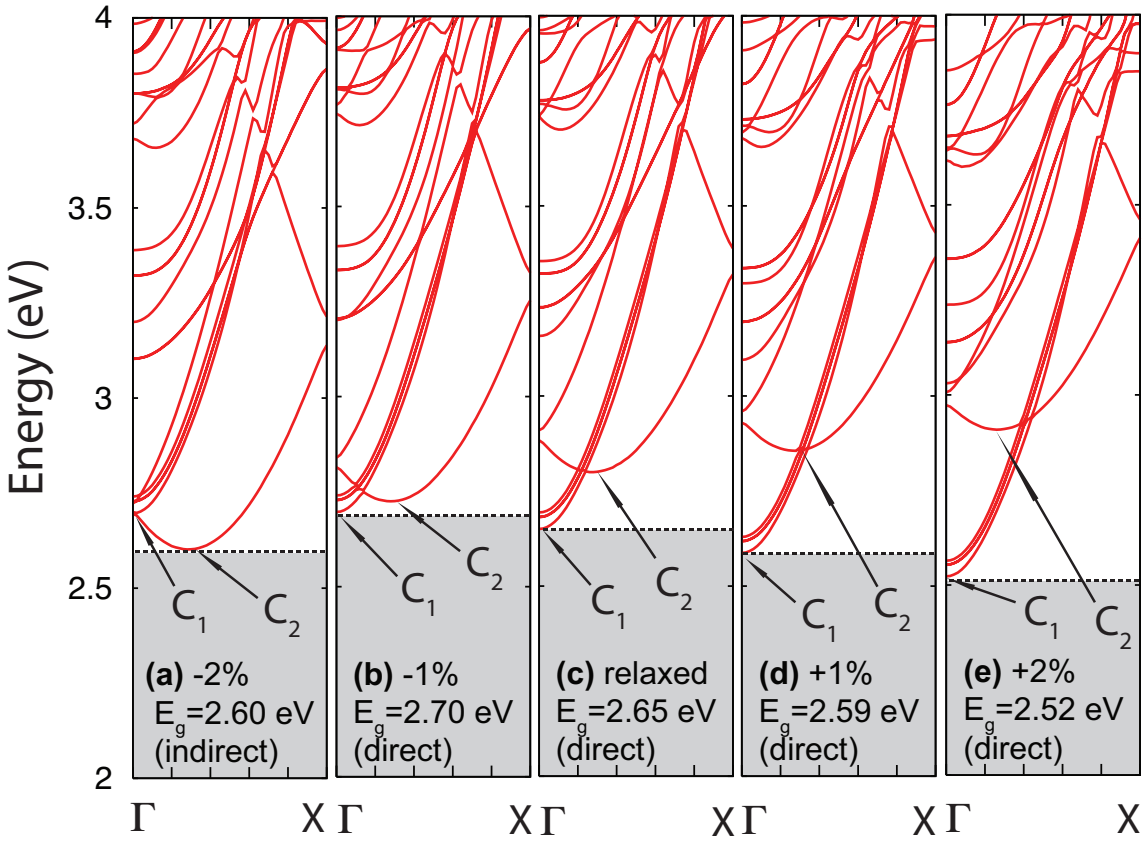

Figure 7.11. Conduction band structure (referenced to the VBM which is arbitrarily fixed to zero at Γ) of a uniaxially strained 1.15 nm diameter [001]-oriented Si NW with strain varying from (a) -2% (compressive) to (e) +2% (tensile). The horizontal dashed lines indicate the conduction-band minimum and the band gap region is represented by a filled area.

For the [001] and [111] Si NWs, the nonlocal corrections to our local pseudopotentials do not affect significantly the strain-induced shift of the conduction band valleys. However, nonlocal corrections play a major role in determining the direct-to-indirect band gap transition as a function of strain for [110] Si NWs. How strongly nonlocal effects influence the band structure of strained, 1.12 nm-diameter [110] Si NW is shown in Fig. 7.12 (a). Here we compare the results obtained using our local pseudopotential with nonlocal corrections (red solid line which shall be referred simply as 'nonlocal') to the results obtained using local-only Zhang's pseudopotential [99] (blue dashed line which shall be referred as 'local'). When relaxed, the conduction band structure from the nonlocal and local models are qualitatively similar except for the C_3 valley which is slightly lower in energy than the C_2 valley according to the nonlocal model but it is higher in energy than C_2 valley according to the local model. However, the CBM is determined by C_1 at Γ resulting in a direct gap for both models in the absence of strain. As the wire is compressively strained, the C_1 valley shifts significantly upward up to a value of about -3% strain while the C_2 and C_3 valleys shift downward and the gap between the C_2 and the C_3 valleys increases according to the nonlocal model, as shown in Fig. 7.12 (b). This results in a direct-to-indirect band gap transition at a value of about -1% strain. On the other hand, without the nonlocal corrections in the local model, the upward shift of the C_1 valley is less significant compared to the result of the nonlocal model and the gap between the C_2 and C_3 valleys decreases as the wire is compressively strained. This results in the a direct-to-indirect band gap transition at a value of about -3% of strain. When compared to the results of *ab initio* calculations [51], the modulation of the C_1, C_2 and C_3 valleys by strain according to the nonlocal model shows qualitatively better agreement with the *ab initio* results, but the direct-to-indirect band gap transition occurs at different value of strain possibly due to the slightly different wire diameters and geometries we have employed compared to those calculations [51, 78, 42, 96]. Thus,

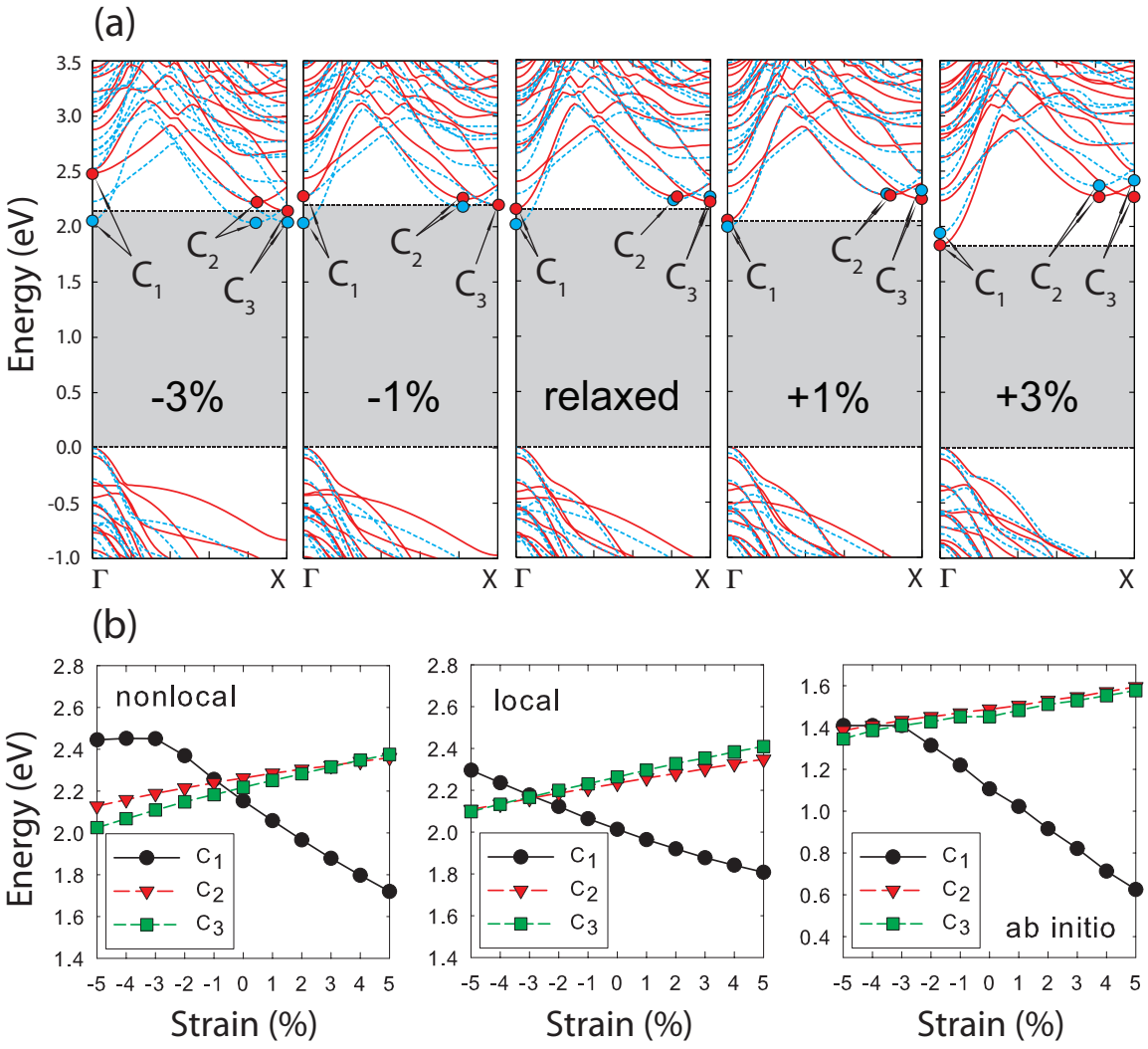

Figure 7.12. (a) Band structure of a uniaxially strained 1.12 nm diameter [110]-oriented Si NW with strain varying from -3% (compressive) to +3% (tensile). The band structure results obtained using our local pseudopotential with nonlocal corrections (red solid line) is compared to the results obtained using Zunger's group local-only pseudopotentials (blue dashed line) where the C_1, C_2 and C_3 minima are represented as circles. The VBM is arbitrarily set to zero and the horizontal dashed lines indicate the CBM and VBM from the band structure obtained using our local pseudopotential with nonlocal corrections. (b) Shifts of C_1, C_2 and C_3 as a function of uniaxial strain from our local pseudopotential with nonlocal corrections (left), Zunger's group local-only pseudopotentials (middle) and *ab initio* calculation in Ref. [51] (right).

we note that in order to obtain results at least in qualitative agreement with those of first-principles calculations regarding strained [110] Si NWs, one should account for nonlocal corrections.

Having discussed how the band structure and the direct-to-indirect band gap transition depend on uniaxial strain, we now consider how the magnitude of the band gap depends on strain. In Fig. 7.13 we show the variation of the band gap as a function of uniaxial strain for the two different diameters ($\sim$ 0.7 nm and $\sim$ 1 nm) for [001], [110] and [111] Si NWs. Direct and indirect band gaps are represented by solid and empty symbols, respectively. Overall, the general trend of the band gap modulation with strain agrees well with other theoretical results[78, 51, 42] and the maximum variation is smaller (less than $\sim$0.5 eV) than in bulk Si [30]. Our results indicate that the largest band gap occurs at a value of about -1% for both 0.77 nm and 1.15 nm diameter [001] wires; at values of about 1% and -1% for 0.64 nm and 1.12 nm [110] wires, respectively; and at values of about -3% for 0.72 nm and 1.24 nm [111] wires. Having reached its maximum value, the band gap decreases almost linearly as the amount of the strain increases for the [001] and [110] nanowires. In the tensile strain region this linear dependence can be approximately evaluated from the fitting expressions $E_g(x) = -6.194x + 3.404$ and $E_g(x) = -6.027x + 2.644$, where x is the amount of strain, for 0.77 nm and 1.15 nm [001] wires, respectively, expressions which are quite similar to those obtained employing the TBM [78]. However, the diameter dependence of the band gap modulation with strain is not significant for [001] NWs, while it is larger for the larger-diameter [110] and [111] wires.

The direct-to-indirect band gap transition is also clearly seen in Fig. 7.13 for all orientations of NWs considered above. Note that the direct-to-indirect band gap transition occurs at different value of strain depending on the diameter of [001] and [110] wires. For example, the transition occurs at -1% strain for 0.77 nm [001] wire in Fig. 7.13 (a) while it occurs at -2% strain for 1.15 nm [001] wire in Fig. 7.13 (b). In

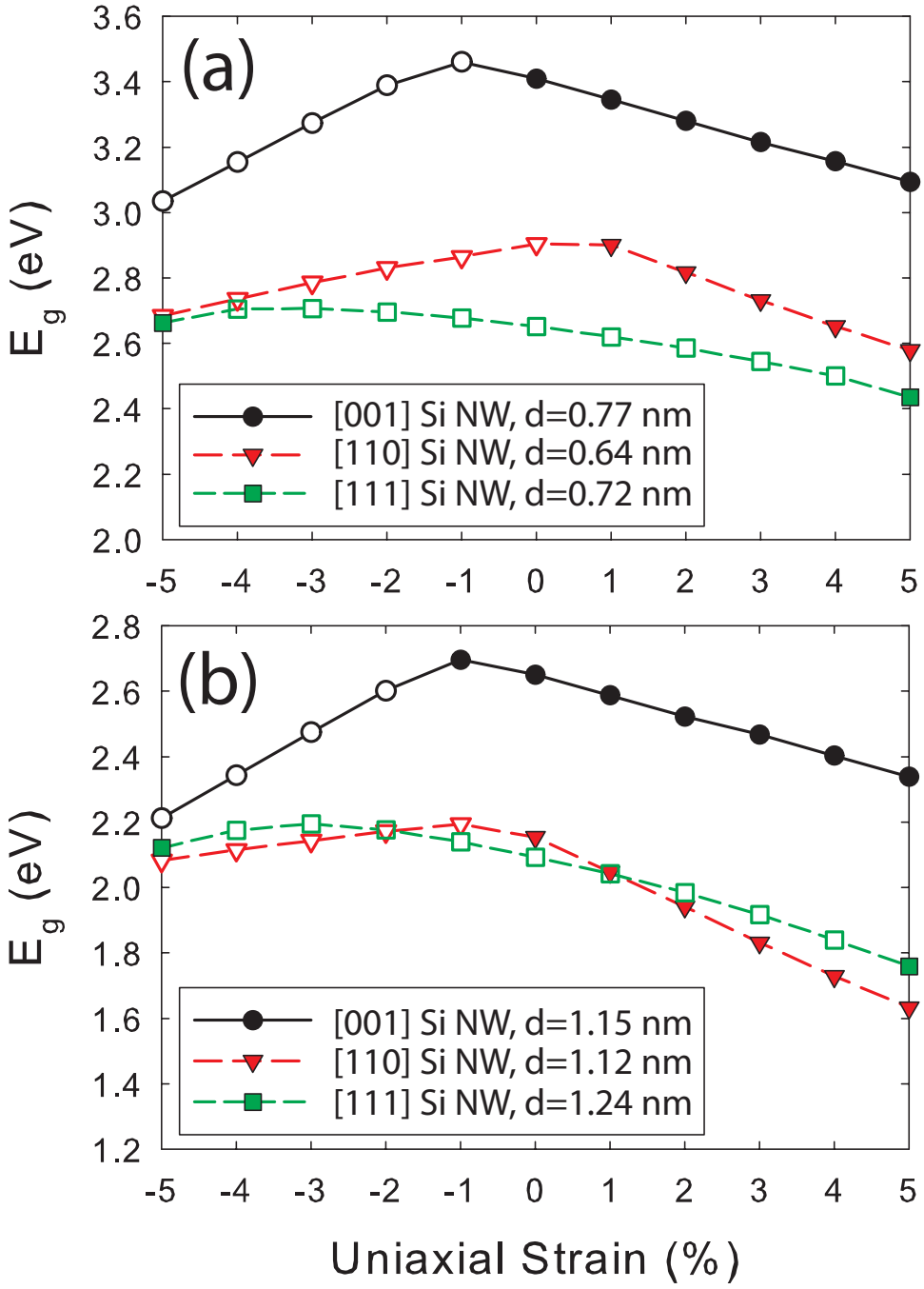

Figure 7.13. Band gap modulation for (a) ~ 0.7 nm and (b) ~ 1 nm diameter [001], [110] and [111] Si NWs as a function of uniaxial strain. The positive and negative values for the strain represent tensile and compressive strain, respectively. Direct and indirect band gaps are represented as solid and empty symbols, respectively.

other word, as the wire diameter decreases, the relative shifts of the C_1 and C_2 valleys in Fig. 7.11 become more sensitive to strain, effect which is qualitatively consistent with the results of Ref. [42].

7.4 Ballistic Conductance

In order to gain some understandings of the electronic-transport properties of the nanowires, we have calculated the ballistic conductance along the wire axis and the electron effective mass at the CBM. We have mainly focused on the diameter, orientation, and strain dependence of the conductance and of the effective mass.

The one dimensional (1D) ballistic conductance $G_{1D}(E)$ along the wire axis at energy E is given by:

$$\begin{aligned} G_{1D}(E) &= 2e^2\frac{1}{2}\sum_n \int \frac{dk_z}{2\pi}\, v_n(k_z)\, \delta\left[E_n(k_z) - E\right] \\ &= 2e^2\frac{1}{2}\sum_{n,i} \int \frac{dE'}{2\pi}\, v_n(k_{z,n,i}) \left|\frac{dE_n(k_{z,n,i})}{dk_z}\right|^{-1} \delta(E' - E) \\ &= \frac{2e^2}{h}\frac{1}{2}\sum_n p_n \ , \end{aligned} \tag{7.9}$$

where the index i labels the $p_n \geq 0$ solutions $k_{z,n,i}$ of the equation $E_n(k_{z,n,i}) = E'$, $E_n(k_z)$ being the dispersion of (sub)band n, $v_n(k_{z,n,i})$ is the group velocity $(1/\hbar)dE_n(k_{z,n,i})/dk_z$ at the k_z-point $k_{z,n,i}$, and the factor of $1/2$ in the equation above reflects the fact that the sum should be performed only over k_z-points corresponding to a positive group velocity $v_n(k_{z,n,i})$, and so, by symmetry, over $1/2$ of the entire 1D BZ.

Figure 7.14 shows $G_{1D}(E)$ near the valence-band maximum (left panel) and the conduction-band minimum (right panel) in units of the quantum conductance $G_0 = 2e^2/h$ for two different diameters ((a)$\sim$0.7 nm and (b)$\sim$1 nm) for relaxed [001], [110] and [111] Si NWs. As expected from previous theoretical [66] and experimental [55] studies, the conductance is larger at higher energies in larger diameter of wires due

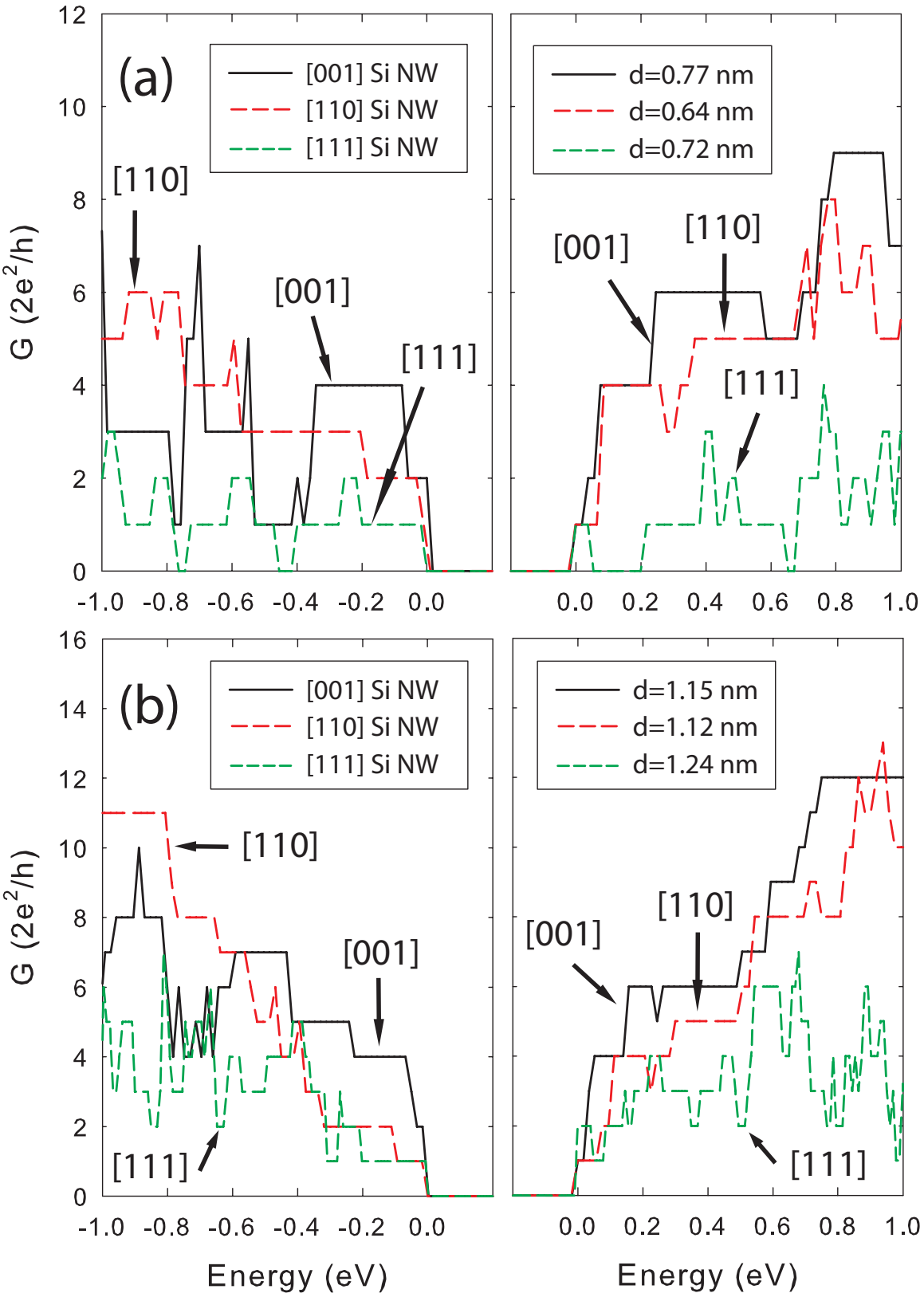

Figure 7.14. Ballistic conductance near the band edges for (a) ~ 0.7 nm and (b) $\sim$ 1 nm diameter [001], [110] and [111] Si NWs. The energies of the conduction-band minimum and the valence-band maximum are arbitrarily set to zero.

to confinement effects. Also note that the conductance for both electrons and holes is larger in [001] wires and smaller in [111] wires. This latter result is a consequence of the fact that, compared to [001]- and [110]-oriented NWs, [111]-oriented wires exhibit fewer band crossings (and so fewer 'Landauer channels') near the band edges, as shown in Fig. 7.8.

Regarding the effect of strain, in Fig. 7.15 we show the contour plots of the electron conductance in [001], [110], and [111] Si NWs as a function of energy and strain for two different diameters (∼0.7 nm (left) and ∼1 nm (right)) (the CBM has been arbitrarily set at zero). Note that the largest conductance occurs at the vertex of the V-shape of the contour seen for [001] and [110] wires vertex which stems from the direct-to-indirect band gap transition occurring at that particular value of strain. This V-shaped contour is not seen in the case of [111] wires, as a result of the fact that the direct-to-indirect band gap transition occurs at ±5% of strain (and so outside the range of the plot), as shown in Fig. 7.13. In summary, we expect that the largest conductance will be observed in large-diameter, compressively strained [001] wires.

7.5 Effective Masses

It is now interesting to consider the variation of the electron and hole effective masses with wire diameter and strain. Having ignored the spin-orbit interaction, which can affect the details of the dispersion at the top of the valence bands, and so the hole effective mass, we have considered only the electron masses. This has been calculated as the 'curvature' mass using a finite difference scheme as follows:

$$m_e^* = \frac{\hbar^2(\Delta k_z)^2}{E_{i+1} - 2E_i + E_{i-1}} \ , \tag{7.10}$$

having employed the values of $\Delta k_z = 10^{-5}$ (in units of $2\pi/a_0$ for [001] NWs, $2\pi/\sqrt{2}a_0$ for [110] NWs and $2\pi/\sqrt{3}a_0$ for [111] wires). Figure 7.16 shows the electron effective

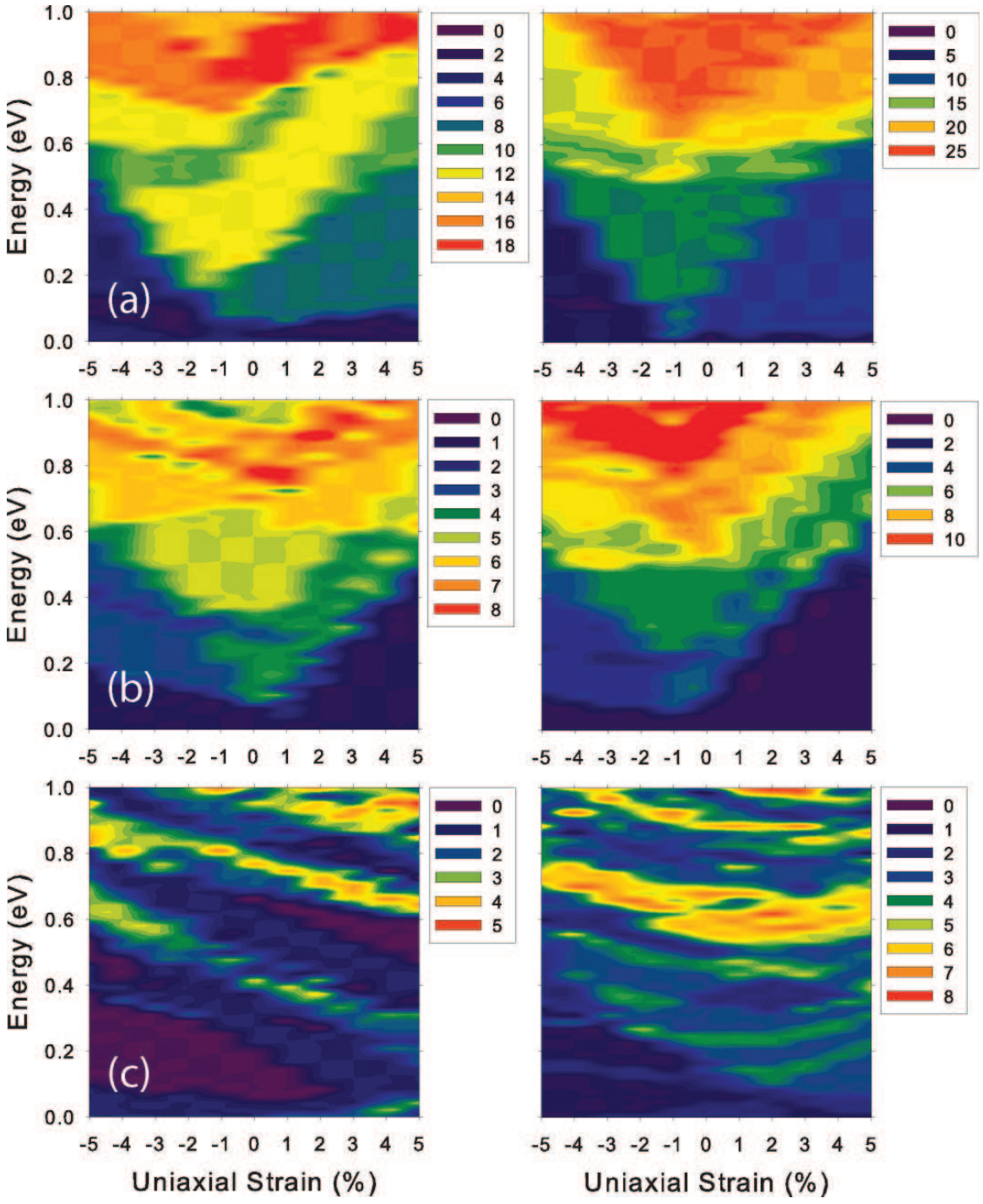

Figure 7.15. Contour plot of the ballistic electron conductance in unit of the universal conductance $G_0 = 2e^2/h$ as a function of energy and uniaxial strain for diameters of $\sim$ 0.7 nm (left) and $\sim$ 1 nm (right)for (a) [001], (b) [110] and (c) [111] Si NWs. The energy of the conduction-band maximum CBM is arbitrarily set to zero.

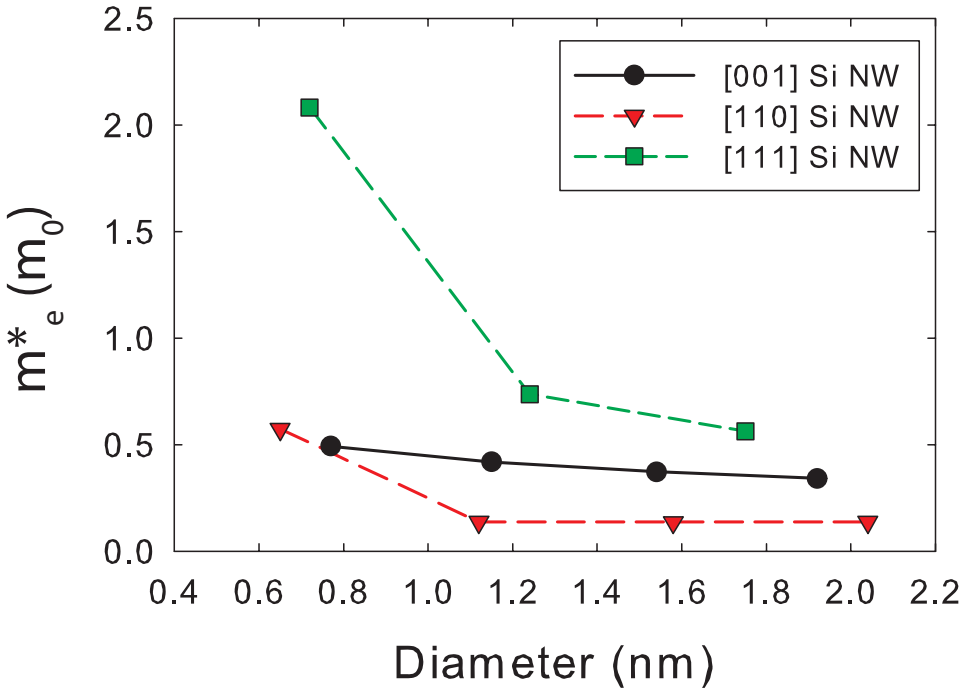

Figure 7.16. Electron effective masses in unit of m_0 at the conduction-band minimum as a function of wire diameter for [001], [110] and [111] Si NWs.

mass m_e^* at the CBM (in units of m_0) as a function of the diameter of [001], [110] and [111] relaxed Si NWs. For [001] wires, m_e^* decreases nonlinearly from $0.49m_0$ to about $0.34m_0$ due to a reduction of confinement effects, thus slowly approaching the value of the transverse effective mass in bulk Si at the Δ minimum ($m_{e,t}^{*(\Delta)} = 0.202m_0$) [44] for large values of the diameter. This is expected from the fact that the CBM for [001] wire is formed by the four-fold degenerated C_1 valleys associated with $m_{e,t}^{*(\Delta)}$ along the transport direction k_z. Similarly, the value of m_e^* in [110] wires is also close to $m_{e,t}^{*(\Delta)}$ as it originates from the transverse mass, $m_{e,t}^{*(\Delta)}$, associated with the two-fold degenerated C_1 valleys. Note also that the effective mass in [110] NWs is almost constant ($\sim 0.13m_0$) and smaller than the value of $m_{e,t}^{*(\Delta)}$ when the diameter is larger than 1 nm, result which is consistent with what reported in Refs. [86] and [51]. In [111] wires we also find a strong nonlinear decrease of m_e^*, from $2.08m_0$ to about $0.56m_0$, as the diameter increases but m_e^* approaches to a value intermediate

between $m_{e,t}^{*(\Delta)}$ and $m_{e,l}^{*(\Delta)}$ since the CBM of [111] wires originates from the six-fold degenerate C_1 valleys whose effective mass along the transport direction results from both $m_{e,t}^{*(\Delta)}$ and $m_{e,l}^{*(\Delta)}$. At a given diameter, m_e^* is the smallest in [110] wires but the largest in [111] wires, since the [111] wires exhibit a very flat dispersion near the CBM compared to [001] and [110] wires, trend in good agreement with the result of Ref. [86].

Figure 7.17 shows m_e^* for [001], [110], and [111] Si NWs for two different diameters ($\sim$0.7 nm and $\sim$1 nm) as a function of uniaxial strain in the range -5% to +5%. Notice a sudden changes of the effective mass for the [001] and [110] wires at the direct-to-indirect band gap transition. As discussed, when the [001] wires are relaxed or under tensile strain the CBM originates from the C_1 valley associated with $m_{e,t}^{*(\Delta)}$. Therefore, the transport effective mass approaches the value of $m_{e,t}^{*(\Delta)}$, as shown in Fig. 7.17 (a). However, the direct-to-indirect gap transition occurs under compressive strain, so that the CBM now originates from the C_2 valleys with mass $m_{e,l}^{*(\Delta)}$ along the transport direction, as shown in Fig. 7.11. Thus m_e^* in compressively strained [001] wires is close to $m_{e,l}^{*(\Delta)}$. Similar considerations also apply to strained [110] wires. On the contrary, the value of m_e^* in [111] wires cannot be understood in terms of such a simple effective mass picture, even though we also see the sudden jump of m_e^* at the direct to indirect gap transition in this case. It should be noted that the value of m_e^* in large-diameter [110] wires under the tensile stress is the smallest, so that we can roughly expect a high electron mobility in these wires (although penalized by a small ballistic conductance). The largest electron mobility in [110]-oriented oriented Si NWs has also been predicted theoretically in Ref. [66].

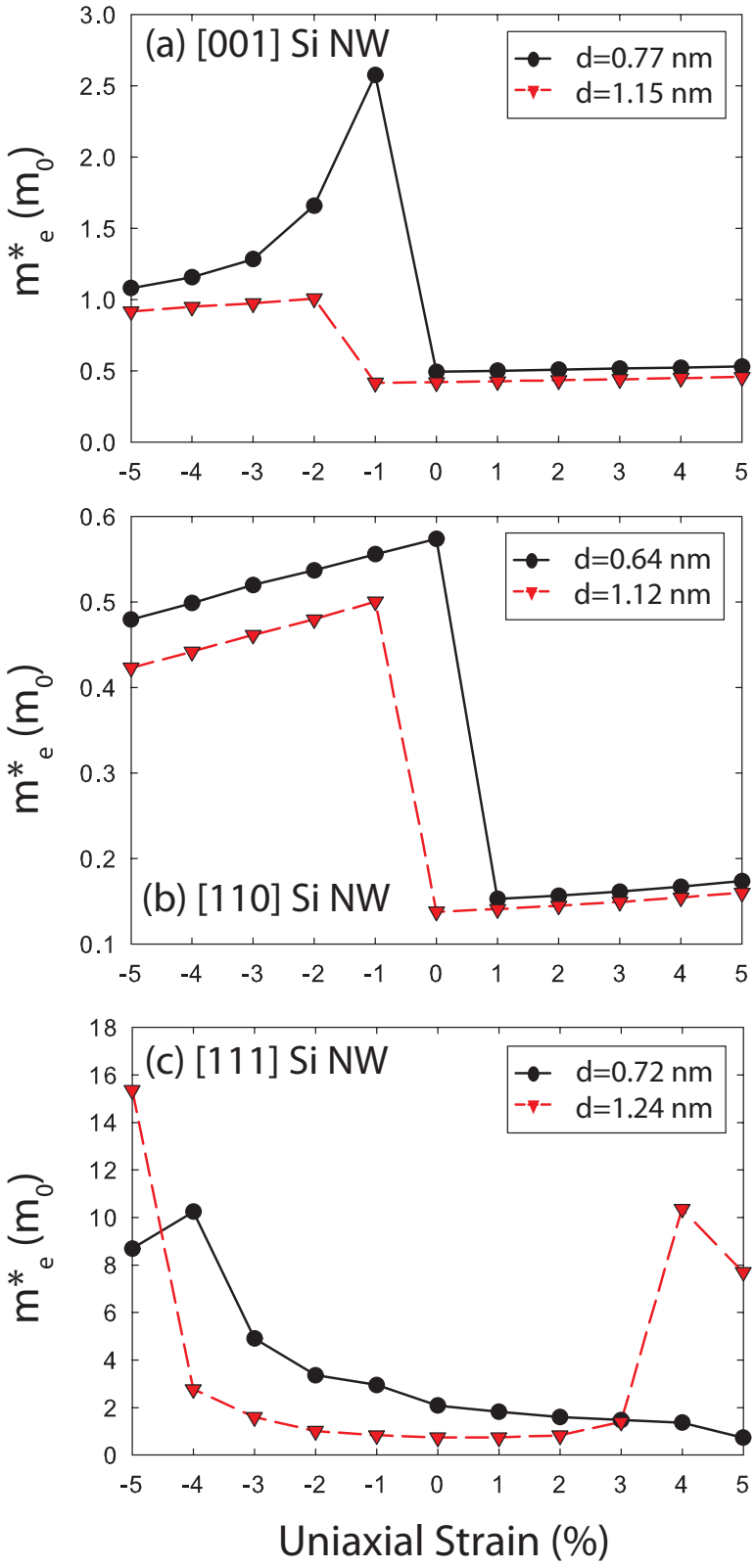

Figure 7.17. Electron effective masses in unit of m_0 at the conduction-band minimum for $\sim$ 0.7 nm and $\sim$ 1 nm diameters (a) [001], (b) [110] and (c) [111] Si NWs as a function of uniaxial strain. The level of strain varies from -5% (compressive) to +5% (tensile), respectively.

CHAPTER 8

CONCLUSIONS

Nonlocal empirical pseudopotentials with spin-orbit interaction have been employed to calculate the electronic band structure of bulk and confined semiconductors under biaxial and uniaxial strain along various crystallographic orientations. In this dissertation, we have thoroughly reviewed various theoretical backgrounds and showed calculated results comparable to the numerous experimental data.

First, we have calculated band structure of bulk semiconductors such as Si, Ge, various III-Vs and their alloys. We have shown that the calculation of the band structure of relaxed semiconductors results in gaps at various symmetry points which are in good agreement with experimental data, giving us confidence in our choice of the local form factors. We have then investigated band structure modulation induced by biaxial strain, study which depends on the interpolation $V(q)$ of the local pseudopotential form factors. A new interpolation scheme of the $V(q)$ has been introduced and the resulting interpolated $V(q)$ has given us better flexibility in reproducing empirically known values for the deformation potentials using linear deformation potential theory. The virtual crystal approximation (with additional empirical parameters regarding compositional disorder effects) has been employed to compute band gap bowing effects in bulk relaxed and strained $In_xGa_{1-x}As$ and $In_xGa_{1-x}Sb$ as a function of In mole fraction x. We also have investigated the effects of strain on electron and hole effective masses at various symmetry points. Without strain, the electron effective masses are proportional to the band gaps and the hole effective masses show a strong dependence of crystal orientation due to the anisotropy

of the valence bands. Bowing effects on hole effective masses have been shown to be more significant in strained than in relaxed alloys, but we have not observe any clear trend of the effective-mass bowing behavior.

Having calculated band structure of bulk semiconductors we have discussed the transferability of the local pseudopotential with correct workfunction which allows us to deal with confined systems with supercell method. Quantum confinement, biaxial and uniaxial strain and crystallographic orientations dependence of band structure for 1D and 2D confined systems have been investigated.

For 1D confined systems, we have studied free-standing, hydrogen passivated Si-thin layer and $Si/Si_{1-x}Ge_x/Si$ hetero layer structures. We have showed nonlinear decrease of the band gap with increased layer thickness in relaxed Si-thin layer due to the quantum confinement effect. Also, we have showed that the direct-to-indirect band transition with biaxial strain for (001) Si-thin layers. In order to mimic more realistic electronic device structure, we have designed $Si/Si_{1-x}Ge_x/Si$ hetero-layer structure in which $Si_{1-x}Ge_x$ layer is biaxially strained with Ge concentration x. We have discussed a band alignment problem between the Si and $Si_{1-x}Ge_x$ layer and showed that parameterization of the $V(q = 0)$ is the reasonable compromise of this problem. However, qualitative study of the effective mass have shown that the curvature hole effective mass is the smallest in Si-only layer implying that degraded hole mobility in $Si/Si_{1-x}Ge_x/Si$ layer relative to the Si-only layer which is inconsistent with experiment so that we need thorough evaluation of the scattering rate.

Finally, we have studied the electronic properties of 2D confined system. We have investigated the diameter and strain dependence of various electronic properties of hydrogen passivated, relaxed and uniaxially strained [001], [110] and [111] Si NWs, in many instances comparing our results to those of first-principle calculations to gain confidence in the correctness and 'portability' of our model potential. Direct and indirect nature of the band gap in relaxed Si NWs of different crystallographic

orientations has been discussed and we have shown how the band gap of relaxed Si NWs decreases nonlinearly and approaches the bulk Si band gap as the wire diameter increases, due to a reduction of quantum confined effects. Nonlocal pseudopotential corrections have provided a qualitatively improved agreement with *ab initio* calculation, especially regarding the energy of the conduction band valleys of strained [110] wires. The variation of the band gap with strain has shown that a direct-to-indirect energy-gap transition occurs in [001] and [110] wires under compressive strain, while the transition occurs at $\pm 5\%$ strain in [111] wires. Then, we have calculated the ballistic conductance and effective mass of electrons in relaxed and strained Si NWs in order to gain some insights on their charge transport properties. In relaxed wires, the electron conductance has found to be the highest in larger diameter of [001] wires while it is the smallest in the smaller diameter of [111] wires. In strained wires, we have found that the largest electron conductance occurs at values of strain causing direct-to-indirect energy-gap transitions, resulting in a V-shape conductance contours, thus leading us to expect the highest conductance in large-diameter [001] wires under compressive uniaxial strain. On the contrary, as far as the electron mobility is concerned, the electron effective mass is the smallest in large-diameter [110] wires under tensile strain, implying an enhanced mobility in these strained [110] wires.

BIBLIOGRAPHY

[1] Adachi, S. Band gaps and refractive indices of AlGaAsSb, GaInAsSb, and InPAsSb: Key properties for a variety of the 2–4-μm optoelectronic device applications. *Journal of Applied Physics 61*, 10 (1987), 4869–4876.

[2] Adachi, S. *Properties of Semiconductor Alloys:Group-IV, III-V and II-VI Semiconductors*. Wiley, May 2009.

[3] Allen, P.B., and Cardona, M. Theory of the temperature dependence of the direct gap of germanium. *Physical Review B 23*, 4 (1981), 1495–1505.

[4] Allen, P.B., and Cardona, M. Temperature dependence of the direct gap of Si and Ge. *Physical Review B 27*, 8 (1983), 4760–4769.

[5] Balslev, I. Influence of uniaxial stress on the indirect absorption edge in silicon and germanium. *Physical Review 143*, 2 (1966), 636–647.

[6] Bechiri, A., Benmakhlouf, F., and Bouarissa, N. Band structure of III–V ternary semiconductor alloys beyond the VCA. *Materials Chemistry and Physics 77*, 2 (2003), 507–510.

[7] Bednarek, S., and Rössler, U. Calculation of the Γ-Δ Electron-Phonon and Hole-Phonon Matrix Elements in Silicon. *Physical Review Letters 48*, 18 (1982), 1296–1296.

[8] Bellaiche, L., Wei, S.H., and Zunger, A. Localization and percolation in semiconductor alloys: GaAsN vs GaAsP. *Physical Review B 54*, 24 (1996), 17568–17576.

[9] Berolo, O., Woolley, J.C., and Van Vechten, J.A. Effect of Disorder on the Conduction-Band Effective Mass, Valence-Band Spin-Orbit Splitting, and the Direct Band Gap in III-V Alloys. *Physical Review B 8*, 8 (1973), 3794–3798.

[10] Bester, G. Electronic excitations in nanostructures: an empirical pseudopotential based approach. *Journal of Physics: Condensed Matter 21*, 2 (2009), 023202.

[11] Bloom, S., and Bergstresser, T.K. Band structure of α-Sn, InSb and CdTe including spin-orbit effects. *Solid State Communications 6*, 7 (1968), 465–467.

[12] Bouarissa, N. Effects of compositional disorder upon electronic and lattice properties of $Ga_xIn_{1-x}As$. *Physics Letters A 245*, 3-4 (1998), 285–291.

[13] Brey, L., Christensen, N.E., and Cardona, M. Deformation potentials at the valence-band maximum in semiconductors. *Physical Review B 36*, 5 (1987), 2638–2644.

[14] Canning, A., Wang, L.W., Williamson, A., and Zunger, A. Parallel empirical pseudopotential electronic structure calculations for million atom systems. *Journal of Computational Physics 160*, 1 (2000), 29–41.

[15] Chandrasekhar, M., and Pollak, F.H. Effects of uniaxial stress on the electroreflectance spectrum of Ge and GaAs. *Physical Review B 15*, 4 (1977), 2127–2144.

[16] Chau, R., Datta, S., Doczy, M., Doyle, B., Jin, B., Kavalieros, J., Majumdar, A., Metz, M., and Radosavljevic, M. Benchmarking nanotechnology for high-performance and low-power logic transistor applications. *IEEE Transactions on Nanotechnology 4*, 2 (2005), 153–158.

[17] Chelikowsky, J.R., and Cohen, M.L. Electronic structure of silicon. *Physical Review B 10*, 12 (1974), 5095–5107.

[18] Chelikowsky, J.R., and Cohen, M.L. Nonlocal pseudopotential calculations for the electronic structure of eleven diamond and zinc-blende semiconductors. *Physical Review B 14*, 2 (1976), 556–582.

[19] Cho, K.H., Yeo, K.H., Yeoh, Y.Y., Suk, S.D., Li, M., Lee, J.M., Kim, M.S., Kim, D.W., Park, D., Hong, B.H., Jung, Y.C., and Hwang, S.W. Experimental evidence of ballistic transport in cylindrical gate-all-around twin silicon nanowire metal-oxide-semiconductor field-effect transistors. *Applied Physics Letters 92* (2008), 052102.

[20] Chu, S.N.G., Macrander, A.T., Strege, K.E., and Johnston Jr, W.D. Misfit stress in InGaAs/InP heteroepitaxial structures grown by vapor-phase epitaxy. *Journal of Applied Physics 57* (1985), 249–257.

[21] Cohen, M.L. Nanotubes, nanoscience, and nanotechnology. *Materials Science and Engineering: C 15*, 1-2 (2001), 1–11.

[22] Cohen, M.L., and Chelikowsky, J.R. *Electronic Structure and Optical Properties of Semiconductors*. Springer-Verlag Berlin, 1988.

[23] Cui, Y., and Lieber, C.M. Functional nanoscale electronic devices assembled using silicon nanowire building blocks. *Science 291*, 5505 (2001), 851.

[24] Cui, Y., Zhong, Z., Wang, D., Wang, W.U., and Lieber, C.M. High performance silicon nanowire field effect transistors. *Nano Letters 3*, 2 (2003), 149–152.

[25] Delley, B., and Steigmeier, E.F. Size dependence of band gaps in silicon nanostructures. *Applied Physics Letters 67* (1995), 2370.

[26] Driad, R., Lu, Z.H., Charbonneau, S., McKinnon, W.R., Laframboise, S., Poole, P.J., and McAlister, S.P. Passivation of InGaAs surfaces and InGaAs/InP heterojunction bipolar transistors by sulfur treatment. *Applied Physics Letters 73* (1998), 665.

[27] Elibol, O.H., Morisette, D., Akin, D., Denton, J.P., and Bashir, R. Integrated nanoscale silicon sensors using top-down fabrication. *Applied Physics Letters 83* (2003), 4613.

[28] Fischetti, M.V., Gámiz, F., and Hänsch, W. On the enhanced electron mobility in strained-silicon inversion layers. *Journal of applied physics 92* (2002), 7320.

[29] Fischetti, M.V., and Higman, J.M. Theory and calculation of the deformation potential electron-phonon scattering rates in semiconductors. In *Monte Carlo Device Simulation: Full Band and Beyond*, K. Hess, Ed. Kluwer Academic Publishers, 1991, ch. 5, pp. 123–160.

[30] Fischetti, M.V., and Laux, S.E. Band structure, deformation potentials, and carrier mobility in strained Si, Ge, and SiGe alloys. *Journal of Applied Physics 80* (1996), 2234.

[31] Friedel, P., Hybertsen, M.S., and Schlüter, M. Local empirical pseudopotential approach to the optical properties of Si/Ge superlattices. *Physical Review B 39*, 11 (1989), 7974–7977.

[32] Geller, C.B., Wolf, W., Picozzi, S., Continenza, A., Asahi, R., Mannstadt, W., Freeman, A.J., and Wimmer, E. Computational band-structure engineering of III–V semiconductor alloys. *Applied Physics Letters 79* (2001), 368.

[33] Gershoni, D., Temkin, H., Vandenberg, J.M., Chu, S.N.G., Hamm, R.A., and Panish, M.B. Type-I to type-II Superlattice Transition in Strained Layers of $In_xGa_{1-x}As$ Grown on InP. *Physical Review Letters 60*, 5 (1988), 448–451.

[34] Gershoni, D., Vandenberg, J.M., Hamm, R.A., Temkin, H., and Panish, M.B. Electronic energy levels in $In_xGa_{1-x}As$/InP strained-layer superlattices. *Physical Review B 36*, 2 (1987), 1320–1323.

[35] Glembocki, O.J., and Pollak, F.H. Calculation of the Γ-L electron-phonon and hole-phonon scattering matrix elements in germanium. *Physical Review B 25*, 12 (1982), 7863–7866.

[36] Goano, M., Bellotti, E., Ghillino, E., Garetto, C., Ghione, G., and Brennan, K.F. Band structure nonlocal pseudopotential calculation of the III-nitride wurtzite phase materials system. Part II. Ternary alloys $Al_xGa_{1-x}N$, $In_xGa_{1-x}N$, and $In_xAl_{1-x}N$. *Journal of Applied Physics 88*, 11 (2000), 6476–6482.

[37] Gomez, L., Chle irigh, N., Hashemi, P., and Hoyt, J.L. Enhanced Hole Mobility in High Ge Content Asymmetrically Strained-SiGe p-MOSFETs. *Electron Device Letters, IEEE 31*, 8 (2010), 782–784.

[38] Harris, C., and O'Reilly, E.P. Nature of the band gap of silicon and germanium nanowires. *Physica E: Low-dimensional Systems and Nanostructures 32*, 1-2 (2006), 341–345.

[39] Harrison, W.A. *Pseudopotentials in the Theory of Metals*. W.A. Benjamin, New York, 1966.

[40] Herman, F., Skillman, S., and Arents, J. Atomic Structure Calculations. *Journal of The Electrochemical Society 111* (1964), 87C.

[41] Herring, C., and Vogt, E. Transport and deformation-potential theory for many-valley semiconductors with anisotropic scattering. *Physical Review 101*, 3 (1956), 944–961.

[42] Hong, K.H., Kim, J., Lee, S.H., and Shin, J.K. Strain-driven electronic band structure modulation of si nanowires. *Nano letters 8*, 5 (2008), 1335.

[43] Kassali, K., and Bouarissa, N. Pseudopotential calculations of electronic properties of $Ga_{1-x}In_xN$ alloys with zinc-blende structure. *Solid State Electronics 44*, 3 (2000), 501–507.

[44] Kim, J., and Fischetti, M.V. Electronic band structure calculations for biaxially strained Si, Ge, and III-V semiconductors. *Journal of Applied Physics 108* (2010), 013710.

[45] Kim, K., Hart, G.L.W., and Zunger, A. Negative band gap bowing in epitaxial InAs/GaAs alloys and predicted band offsets of the strained binaries and alloys on various substrates. *Applied Physics Letters 80* (2002), 3105.

[46] Kittel, C. *Introduction to Solid State Physics*, 7 ed. John Wiley & Sons, 1966.

[47] Krijn, M. Heterojunction band offsets and effective masses in III-V quaternary alloys. *Semiconductor Science and Technology 6* (1991), 27–31.

[48] Kuphal, E., Pöcker, A., and Eisenbach, A. Relation between photoluminescence wavelength and lattice mismatch in metalorganic vapor-phase epitaxy InGaAs/InP. *Journal of Applied Physics 73* (1993), 4599.

[49] Lee, M.L., Leitz, C.W., Cheng, Z., Pitera, A.J., Langdo, T., Currie, M.T., Taraschi, G., Fitzgerald, E.A., and Antoniadis, D.A. Strained Ge channel p-type metal–oxide–semiconductor field-effect transistors grown on SiGe/Si virtual substrates. *Applied Physics Letters 79* (2001), 3344.

[50] Lee, S.J., Kwon, T.S., Nahm, K., and Kim, C.K. Band structure of ternary compound semiconductors beyond the virtual crystal approximation. *Journal of Physics : Condensed Matter 2*, 14 (1990), 3253–3257.

[51] Leu, P.W., Svizhenko, A., and Cho, K. Ab *initio* calculations of the mechanical and electronic properties of strained Si nanowires. *Physical Review B 77*, 23 (2008), 235305.

[52] Li, Y.H., Gong, X.G., and Wei, S.H. Ab *initio* calculation of hydrostatic absolute deformation potential of semiconductors. *Applied Physics Letters 88* (2006), 042104.

[53] Liboff, R.L. *Introductory quantum mechanics*. Addison-Wesley Reading, MA, 2003.

[54] Long, F., Harrison, P., and Hagston, W.E. Empirical pseudopotential calculations of $Cd_{1-x}Mn_xTe$. *Journal of Applied Physics 79* (1996), 6939.

[55] Lu, W., Xiang, J., Timko, B.P., Wu, Y., and Lieber, C.M. One-dimensional hole gas in germanium/silicon nanowire heterostructures. *Proceedings of the National Academy of Sciences of the United States of America 102*, 29 (2005), 10046.

[56] Ma, Q.M., Wang, K.L., and Schulman, J.N. Band structure and symmetry analysis of coherently grown $Si_{1-x}Ge_x$ alloys on oriented substrates. *Physical Review B 47*, 4 (1993), 1936–1953.

[57] Madelung, O. *Landolt–Bornstein: Numerical Data and Functional Relationships in Science and Technology*. Springer Berlin, 1982.

[58] Madelung, O, Ed. *Data in Science and Technology; Semiconductors Group IV Elements and III-V Compounds*. Springer-Verlag, 1991.

[59] Mäder, K.A., and Zunger, A. Empirical atomic pseudopotentials for AlAs/GaAs superlattices, alloys, and nanostructures. *Physical Review B 50*, 23 (1994), 17393–17405.

[60] Nehari, K., Cavassilas, N., Autran, J.L., Bescond, M., Munteanu, D., and Lannoo, M. Influence of band structure on electron ballistic transport in silicon nanowire MOSFET's: An atomistic study. *Solid-State Electronics 50*, 4 (2006), 716–721.

[61] Nielsen, O.H., and Martin, R.M. Stresses in semiconductors: Ab *initio* calculations on Si, Ge, and GaAs. *Physical Review B 32*, 6 (1985), 3792–3805.

[62] Noack, R.A., Rühle, W., and Morgan, T.N. Bound excitons at doubly ionizable acceptors in GaSb. *Physical Review B 18*, 12 (1978), 6944–6956.

[63] Nolan, M., O'Callaghan, S., Fagas, G., Greer, J.C., and Frauenheim, T. Silicon nanowire band gap modification. *Nano Lett 7*, 1 (2007), 34–38.

[64] Nye, J.F. *Physical Properties of Crystals: Their Representation by Tensors and Matrices*. Oxford University Press, 1985, p. 134.

[65] Peng, G.W., and Feng, Y.P. Anomalous strain dependent effective masses in (111) Si nanowires. *Applied Physics Letters 91* (2007), 083116.

[66] Persson, M.P., Lherbier, A., Niquet, Y.M., Triozon, F., and Roche, S. Orientational dependence of charge transport in disordered silicon nanowires. *Nano Letters 8*, 12 (2008), 4146–4150.

[67] Phillips, J.C., and Kleinman, L. New method for calculating wave functions in crystals and molecules. *Physical Review 116*, 2 (1959), 287–294.

[68] Phillips, J.C., and Pandey, K.C. Nonlocal Pseudopotential for Ge. *Physical Review Letters 30*, 17 (1973), 787–790.

[69] Polizzi, E. Density-matrix-based algorithm for solving eigenvalue problems. *Physical Review B 79*, 11 (2009), 115112.

[70] Pollak, F.H., and Cardona, M. Piezo-Electroreflectance in Ge, GaAs, and Si. *Physical Review 172*, 3 (1968), 816–837.

[71] Priester, C., Allan, G., and Lannoo, M. Band-edge deformation potentials in a tight-binding framework. *Physical Review B 37*, 3 (1988), 8519–8522.

[72] Read, A.J., Needs, R.J., Nash, K.J., Canham, L.T., Calcott, P.D.J., and Qteish, A. First-principles calculations of the electronic properties of silicon quantum wires. *Physical Review Letters 69*, 8 (1992), 1232–1235.

[73] Rieger, M.M., and Vogl, P. Electronic-band parameters in strained $Si_{1-x}Ge_x$ alloys on $Si_{1-y}Ge_y$ substrates. *Physical Review B 48*, 19 (1993), 14276–14287.

[74] Rim, K., Anderson, R., Boyd, D., Cardone, F., Chan, K., Chen, H., Christansen, S., Chu, J., Jenkins, K., Kanarsky, T., Koester, S., Lee, B.H., Lee, K., Mazzeo, V., Mocuta, A., Mocuta, D., Mooney, P.M., Oldiges, P., Ott, J., Ronsheim, P., Roy, R., Steegen, A., Yang, M., Zhu, H., Leong, M., and Wong, H.-S.P. Strained Si CMOS (SS CMOS) technology: opportunities and challenges. *Solid State Electronics 47*, 7 (2003), 1133–1139.

[75] Sacconi, F., Persson, M.P., Povolotskyi, M., Latessa, L., Pecchia, A., Gagliardi, A., Balint, A., Fraunheim, T., and Di Carlo, A. Electronic and transport properties of silicon nanowires. *Journal of Computational Electronics 6*, 1 (2007), 329–333.

[76] Saravia, L.R., and Brust, D. Spin Splitting and the Ultraviolet Absorption of Ge. *Physical Review 176*, 3 (1968), 915–923.

[77] Scheel, H., Reich, S., and Thomsen, C. Electronic band structure of high-index silicon nanowires. *Physica Status Solidi B : Basic Research 242*, 12 (2005), 2474.

[78] Shiri, D., Kong, Y., Buin, A., and Anantram, MP. Strain induced change of bandgap and effective mass in silicon nanowires. *Applied Physics Letters 93* (2008), 073114.

[79] Silver, M., Batty, W., Ghiti, A., and O'Reilly, E.P. Strain-induced valence-subband splitting in III-V semiconductors. *Physical Review B 46*, 11 (1992), 6781–6788.

[80] Sun, Y., Thompson, SE, and Nishida, T. Physics of strain effects in semiconductors and metal-oxide-semiconductor field-effect transistors. *Journal of Applied Physics 101* (2007), 104503.

[81] Takagi, S., Hoyt, J.L., Welser, J.J., and Gibbons, J.F. Comparative study of phonon-limited mobility of two-dimensional electrons in strained and unstrained Si metal–oxide–semiconductor field-effect transistors. *Journal of Applied Physics 80* (1996), 1567.

[82] Takagi, S., Toriumi, A., Iwase, M., and Tango, H. On the universality of inversion layer mobility in Si MOSFET's: Part I-Effects of substrate impurity concentration. *IEEE Transactions on Electron Devices 41*, 12 (1994), 2357–2362.

[83] Tiwari, S., and Frank, D.J. Empirical fit to band discontinuities and barrier heights in III–V alloy systems. *Applied Physics Letters 60* (1992), 630.

[84] Van de Walle, C.G. Band lineups and deformation potentials in the model-solid theory. *Physical Review B 39*, 3 (1989), 1871–1883.

[85] Van de Walle, C.G., and Martin, R.M. Theoretical calculations of heterojunction discontinuities in the Si/Ge system. *Physical Review B 34*, 8 (1986), 5621–5634.

[86] Vo, T., Williamson, AJ, and Galli, G. First principles simulations of the structural and electronic properties of silicon nanowires. *Physical Review B 74*, 4 (2006), 45116.

[87] Vurgaftman, I., Meyer, J.R., and Ram-Mohan, L.R. Band parameters for III–V compound semiconductors and their alloys. *Journal of Applied Physics 89* (2001), 5815.

[88] Walter, J.P., Cohen, M.L., Petroff, Y., and Balkanski, M. Calculated and Measured Reflectivity of ZnTe and ZnSe. *Physical Review B 1*, 6 (1970), 2661–2667.

[89] Wang, L.W., and Zunger, A. Electronic Structure Pseudopotential Calculations of Large (. apprx. 1000 Atoms) Si Quantum Dots. *The Journal of Physical Chemistry 98*, 8 (1994), 2158–2165.

[90] Wang, L.W., and Zunger, A. Solving Schrodinger's equation around a desired energy: application to silicon quantum dots. *The Journal of Chemical Physics 100*, 3 (1994), 2394–2397.

[91] Wang, T.Y., and Stringfellow, G.B. Strain effects on GaInAs/InP single quantum wells grown by organometallic vapor-phase epitaxy with $0 \leqslant x \leqslant 1$. *Journal of Applied Physics 67* (1990), 344.

[92] Weisz, G. Band structure and Fermi surface of white tin. *Physical Review 149*, 2 (1966), 504–518.

[93] Welser, J., Hoyt, JL, and Gibbons, JF. Electron mobility enhancement in strained-Si n-typemetal-oxide-semiconductor field-effect transistors. *IEEE Electron Device Letters 15*, 3 (1994), 100–102.

[94] Williamson, A.J., and Zunger, A. InAs quantum dots: Predicted electronic structure of free-standing versus GaAs-embedded structures. *Physical Review B 59*, 24 (1999), 15819–15824.

[95] Wu, Y., Cui, Y., Huynh, L., Barrelet, C.J., Bell, D.C., and Lieber, C.M. Controlled growth and structures of molecular-scale silicon nanowires. *Nano letters 4*, 3 (2004), 433–436.

[96] Wu, Z., Neaton, J.B., and Grossman, J.C. Charge separation via strain in silicon nanowires. *Nano Letters 9*, 6 (2009), 2418–2422.

[97] Yeh, C.Y., Zhang, S.B., and Zunger, A. Confinement, surface, and chemisorption effects on the optical properties of Si quantum wires. *Physical Review B 50*, 19 (1994), 14405–14415.

[98] Yu, P.Y., and Cardona, M. *Fundamentals of Semiconductors: Physics and Materials Properties*, 3 ed. Springer, 2001.

[99] Zhang, S.B., Yeh, C.Y., and Zunger, A. Electronic structure of semiconductor quantum films. *Physical Review B 48*, 15 (1993), 11204–11219.

[100] Zhang, Y., Kim, J., and Fischetti, M.V. Self-consistent calculation for valence subband structure and hole mobility in p-channel inversion layers. *Journal of Computational Electronics 7*, 3 (2008), 176–180.

[101] Zhao, X., Wei, CM, Yang, L., and Chou, MY. Quantum confinement and electronic properties of silicon nanowires. *Physical review letters 92*, 23 (2004), 236805.